Interfacial profiles of wavy film flow in vertical pipe at low Reynolds numbers – an experimental study

Keerthivasan Rajamani

Technische Universiteit Delft

Interfacial profiles of wavy film flow in vertical pipe at low Reynolds numbers – an experimental study

by

Keerthivasan Rajamani

in partial fulfillment of the requirements for the degree of

Master of Science
in Mechanical Engineering

at the Delft University of Technology,
to be defended on February 12, 2018 at 1400.

P & E Report Number : 2875

Supervisor:	Dr. René Delfos	TU Delft
Thesis committee:	Dr. ir. Mark J. Tummers	TU Delft
	Prof. dr. ir. Bendiks Jan Boersma	TU Delft
	ir. Andries van Eckeveld	TU Delft

CONTENTS

List of Symbols

Abbreviations

CCD	Charged Coupled Device
LIF	Laser Induced Fluorescence
PLIF	Planar Laser Induced Fluorescence
PIV	Particle Image Velocimetry
PDD	Probability Density Distribution

Symbols

Ka	Kapitza number	
Re	Reynolds number	
C	Value of cross-correlation coefficient	
f	Frequency of measurements	Hz
g	Gravitational Acceleration	m/s^2
h	Film Height	m
H	Time and space averaged value of the film thickness across all recorded frames	m
i	Pixel location in the horizontal direction	
j	Pixel location in the vertical direction	
k	Thermal conductivity of the liquid	$W/(m \cdot K)$
N	Total number of film thickness measurements	
P	Phase velocity of the wave	m/s
r	Radial clearance between the slit adjuster and converging section in the liquid distributor.	m
s	Ratio of increase in recorded fluorescence intensity for per unit increase in dye concentration.	
t	Time	s
v	velocity of the liquid in the direction of gravity	m/s
X	Cross-stream direction	
x	Distance from the plate in the cross-stream direction	m
Y	Stream-wise direction	
y	Vertical distance along the wall	m
Z	Span-wise direction	
$\mathcal{O}$	Indicates order of magnitude	
$\dot{m}$	mass flow rate of the fluid per unit width	$kg/(m \cdot s)$
μ	Dynamic Viscosity	$kg/(m \cdot s)$
ν	Kinematic Viscosity	m^2/s
σ	Surface Tension	N/m
ρ	Density	kg/m^3
δ	Film Thickness	m

List of Figures

List of Tables

ACKNOWLEDGEMENTS

First of all, I would like to thank my parents for their unconditional love and support throughout my endeavours.

I am grateful to the following persons at my under-graduate institution, who inspired me to pursue higher education and research. Dr. Madhu Ganesh, who's undergraduate fluid mechanics and heat transfer classes helped me to develop interest in thermal sciences; Prof. V. Ramachandran, who's humbleness and curiosity even at his eighties is something that I have deeply admired; and Dr. P. V. Mohanram for his lectures which has always kindled my curiosity.

I would like to thank my thesis supervisor, Dr. René Delfos for his mentorship during the thesis period, patiently clarifying all my concerns, and providing support whenever I ran into trouble. It was an enriching experience to carryout systematic investigations and careful interpretation of the results obtained. I believe this training would serve a sound basis for all the scientific work that I venture into in the future.

I am thankful to Mr. Jasper Ruijgrok for helping with mechanical aspects of the experimental setup and especially for manufacturing the calibration cylinders; and to Ing. Edwin F.J. Overmars for assisting in setting up the laser and optical system of the experimental setup.

My stay at Delft has been pleasantly memorable, and this would have not been possible without my friends - Aditya, Digvijay, Naren, Sai, Vaibhav, and Veera. Thank you all for providing the assistance needed during the experiments, and patiently proof-reading my report several times.

Finally, I would like to thank Dr. ir. Mark J. Tummers, Prof. dr. ir. Bendiks Jan Boersma, and ir. Andries van Eckeveld for taking time to be on my thesis committee.

ABSTRACT

A liquid film falling vertically along a wall results in the formation of waves at the liquid-gas interface. The principal forces in these flows are gravity, viscosity, and surface tension, which are characterized by the Reynolds number, *Re* and the Kapitza number, *Ka*. Experimental characterization of the film flows for high viscosity liquids ($Ka \sim \mathcal{O}(1)$) at low $Re \sim \mathcal{O}(10)$ was performed for flow along the inner circumference of a vertical pipe. The three-dimensional liquid-gas interfacial profile is quantitatively reconstructed using the laser induced fluorescence technique. The waves observed had higher surface steepness at the front when compared with the back of the wave crest. The film thickness at the back of the wave crest is higher than at the front, resembling the streak-like waves observed in the literature for low-viscosity liquids ($Ka \sim \mathcal{O}(10^3)$) at comparable *Re*. When the lateral surfaces of the waves are in contact, merging in the transverse direction is observed. The experimentally determined mean film thickness was ≈ 15 % lower than the Nusselt's flat film thickness, while the experimental values of average wave velocity was ≈ 4 times higher than the Nusselt's velocity for the corresponding film thickness. On the time-averaged film thickness field, a transverse variation in the film thickness, called as ridges and valleys, were observed. These transverse variations are found to be unsteady in their behaviour. Probability density distributions of the film thickness measurements showed two distinctive time-dependant patterns for the distribution of film thickness values in the ridges.

1

INTRODUCTION

1

1.1. FALLING FILMS

A film of liquid falling over a vertical surface has fascinated the fluid dynamics community for nearly 7 decades with its unique and interesting wave flow patterns. Nusselt (1916) considered a film flow without waves i.e. a laminar flow, over a vertical wall such as the region identified as "flat film flow" in Fig. 1.1, and provided the analytical solution for the film thickness. In an actual film flow, the infinitesimal disturbances present at the liquid inlet gets amplified and results in wave formation at the interface (Chang (1994)). The first scientific study on the appearance of waves in vertical film flows was reported by the Russian Physicists Kapitza and Kapitza (1949). They also proposed that a film falling vertically down has a critical Reynolds number for transition from a flat film, i.e. laminar, to a film with waves or irregularities on its free surface, i.e. a wavy laminar regime. This hypothesis was based on their experimental observations of film thickness. However, Benjamin (1957) showed (as reported in Kalliadasis et al. (2011)) through theoretical analysis that for a film falling vertically, waves would appear at all Reynolds number, i.e. it is unconditionally unstable.

The industrial interest in falling film phenomenon is due to its enhanced heat (Gross et al. (2009)) and mass transfer (Yoshimura et al. (1996)). A simple falling film evaporator consists of a vertical tube through which the the liquid to be concentrated falls as a film, while heat, typically steam, is passed on the outside of the tube. The typical dimensions of the tube, for example in the milk industry is 4 to 15 m in length and 25 to 80 mm in diameter (Varnam and Sutherland (1994)). The exposure time of liquids to the heating medium is short, typically a few seconds (Woods (2007)) to minutes (Asadi (2006)). Further, the temperature difference between the process liquid and the heating medium can be as low as 10 ^{o}C (Cheremisinoff (2000)). Owing to these advantages, falling film evaporators are extensively used to obtain concentrates of temperature sensitive liquids such as fruit juices, milk, sucrose, chemical solvents, and slurries.

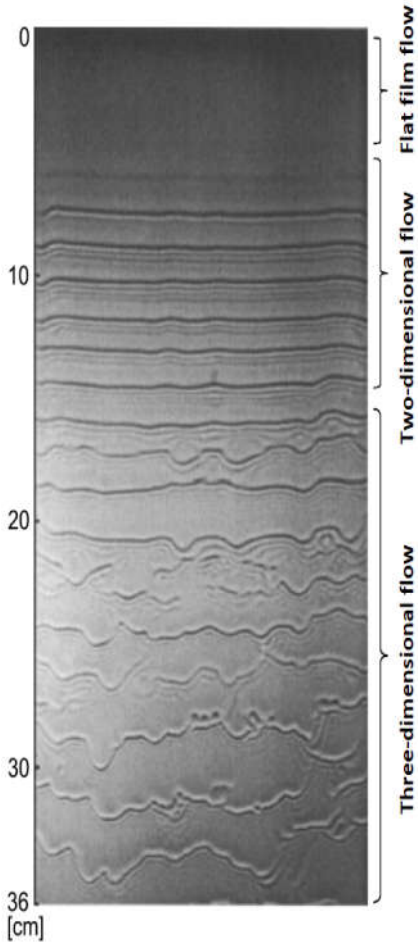

Figure 1.1: Shadow image of vertical film flow of water at Re = 131, Park and Nosoko (2003).

Another advantage of the falling film evaporator that is of industrial interest is in its ability to be retrofitted with existing heat exchangers. By doing so, Grant et al. (2000) obtained a reduction in the steam demand on sugar-cane from 45 % to 30 %. Also retrofitting is relatively less expensive than replacing the existing setup with a new installation. This results in increased payback and is thus investment friendly. Apart from evaporators, the film flow phenomenon is important in applications such as: (i) cooling of microelectronic equipment; (ii) film coating process; and (iii) to perform as lubrication layers for transporting oil through long distance pipelines (Kalliadasis et al. (2011)).

The initial step in efficiently applying a film flow phenomenon to an application is to understand the hydrodynamic behaviour of the liquid. Though extensive literature is available for hydrodynamic behaviour of low viscosity liquids (quantified in the next section), studies for high viscosity liquids are scarce (Mendez et al. (2017)). Thus the present work focuses to experimentally characterize the behaviour of such liquids by utilizing techniques to measure film thickness over a curved surface.

In the remaining portion of this chapter, the dimensionless groups characterizing the vertical film flows is described in section 1.2, followed by the Nusselt's solution to laminar film thickness in section 1.3. A brief review of the literature with historical background on falling films is presented in section 1.4. Since the present work is experimental in nature, emphasis is given to the same in the review. The presence of the temperature gradient in the film free surface initiates the so-called Marangoni driven flows and it is explained next. It is followed by a typical classification of the film flow regimes as waves exhibit many complex dynamics. The experimental works performed using contact measurements (conductance probes) and non-contact measurements (section 1.5) are then discussed. The chapter ends with the research objectives.

1.2. CHARACTERIZATION OF FILM FLOWS

The principal forces acting in a vertically falling film are viscosity, inertia, and surface tension. These are characterized by the two dimensionless numbers - the Reynolds number (*Re*), and the Kapitza number (*Ka*).

REYNOLDS NUMBER

Reynolds number (*Re*) represents the ratio of inertial forces to viscous forces. The *Re* used in the present work is defined as,

$$Re = \frac{4 \cdot \rho \cdot \delta \cdot v}{\mu} \tag{1.1}$$

where, ρ represents the density of the liquid [kg/m^3], δ is the film thickness measured in the direction perpendicular to the vertical wall [m] (Fig. 1.2), v is the velocity of the liquid along the direction of gravity [m/s], and μ represents the dynamic viscosity of the liquid [kg/(m · s)].

Alternate definitions of *Re* exist in the literature, where the factor "4" is not used in the numerator. To be consistent while quoting the Reynolds number of other studies, they are transformed to definition given by Eq. 1.1.

KAPITZA NUMBER

Kapitza number (*Ka*) is the ratio of surface tension force to inertial force. *Ka* is defined by,

$$Ka = \frac{\sigma}{\rho \cdot g^{1/3} \cdot \nu^{4/3}} \tag{1.2}$$

where, σ represents the surface tension of the liquid (unless otherwise mentioned, the contact medium is air) [N/m], g is the gravitational acceleration [m/s^2], and ν is the kinematic viscosity of the liquid [m^2/s]. Unlike *Re*, *Ka* depends only on the liquid property. *Ka* is related to the Morton number (*Mo*) by the relation, $Ka = Mo^{-1/3}$ (Kay and Nedderman (1974)). The value of *Ka* for water at 20 ^{o}C is $\approx$ 3370. The liquid used in the present study for film formation is 84 wt. % glycerine-water mixture, which has a *Ka* value of $\approx$ 8 at 20 ^{o}C. Typically, liquids having low-viscosity are characterized by $Ka \sim \mathcal{O}\left(10^2 - 10^3\right)$, while high-viscosity liquids are characterized by $Ka \sim \mathcal{O}(1)$.

1.3. NUSSELT'S SOLUTION TO LAMINAR FILM THICKNESS

WITHOUT HEAT TRANSFER

Consider a vertical wall on which a liquid film flow happens, as shown in Fig. 1.2. For a hydro-dynamically fully developed flow, since there is no acceleration, the net force acting on the control volume, which is shaded in blue color, should be zero. Nusselt's solution to laminar film thickness without heat transfer is obtained by performing a force balance between gravity and viscosity on this control volume. The main results are presented in this section, while a detailed derivation is shown in Appendix A.

The laminar velocity profile within the film is given by (also known as Nusselt flat film velocity solution in the literature) Eq. 1.3.

$$v = \frac{(\delta x - \frac{x^2}{2}) \cdot g}{\nu} \qquad [m/s] \tag{1.3}$$

where, v is the velocity of the liquid [m/s] in the stream-wise direction (along Y in Fig. 1.2), δ is the film thickness [m], and x is the location of interest between the wall and the liquid-vapour interface.

The mass flow rate of the liquid per unit width ($\dot{m}$) could be obtained by integrating the velocity over the thickness resulting in Eq. 1.4

$$\dot{m} = \rho \cdot \frac{g}{\nu} \cdot \frac{\delta^3}{3} \qquad [kg/(m \cdot s)] \tag{1.4}$$

The laminar film thickness is given by Eq. 1.5.

$$\delta_{\text{without heat transfer}} = \left(\frac{3 \cdot \nu \cdot \dot{m}}{\rho \cdot g}\right)^{1/3} \qquad [m] \tag{1.5}$$

Laminar film thickness from Eq. 1.5 is plotted in Fig. 1.3 for three liquids - Water, 100 wt. % Glycerol, and 87 wt. % Glycerol (13 wt. % water).

1

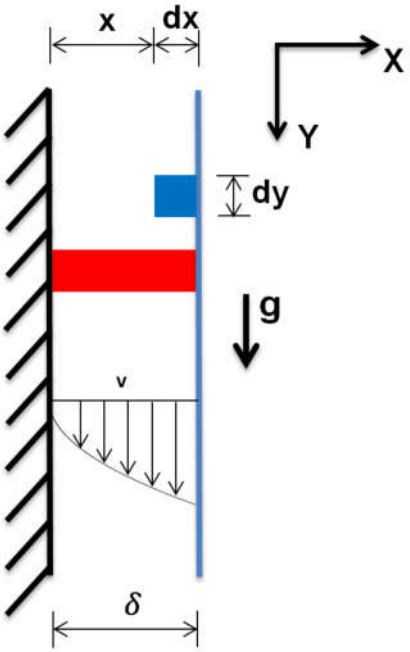

Figure 1.2: Laminar vertical falling film. The blue colored shaded region is the control volume for obtaining the Eq. 1.5, while the red colored region is the control volume for obtaining Eq. 1.6. Film thickness is denoted by δ, while v represents the velocity in the stream-wise direction. Y axis is taken positive downwards. Z axis is normal to the figure.

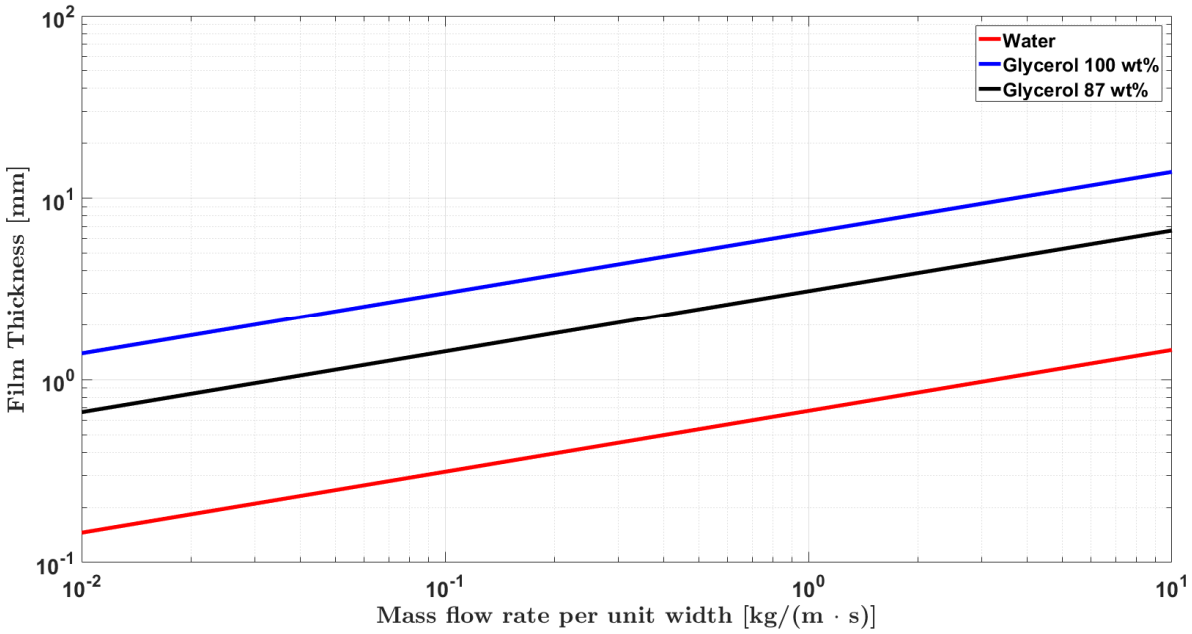

Figure 1.3: Log-Log plot of laminar film thickness at different mass flow rates along a vertical wall per unit depth (i.e. in Z direction) for three liquids: water, 100 wt % glycerine, and 87 wt % glycerine (13 wt % water). The densities used for water, 100 wt % glycerine, and 87 wt % glycerine are 998.23, 1261.08, and 1227.1 kg/m^3, while the dynamic viscosities are 0.001, 1.410, and 0.1445 kg/(m · s) respectively (Cheng (2008)).

WITH HEAT AND MASS TRANSFER

The principle of energy conservation is used to model the film thickness with condensation or evaporation. In this case, the heat transfer happens at both the interfaces - (i) convection at liquid-vapour interface, and (ii) conduction at liquid-solid interface. The Nusselt's solution to laminar film thickness with heat transfer is

obtained by applying energy conservation principle to the control volume indicated by the red colored box in Fig. 1.2. The final form is presented in Eq. 1.6, while the derivation is provided in the Appendix B.

$$\delta_{\text{with heat transfer}} = \left(\delta^4_{y=0} + \frac{4 \cdot \nu \cdot k \cdot (T_{film} - T_{wall})}{h_{fg} \cdot \rho \cdot g} \cdot y\right)^{1/4} \qquad [m] \tag{1.6}$$

where h_{fg} is the enthalpy of vaporization of the liquid [kJ/kg], k is the thermal conductivity of the liquid [W/(m · K)], T is the temperature of the film/wall [K], and y is the vertical location along the wall [m].

Qualitatively, Eq. 1.6 informs that for the case of evaporation, ($T_{\text{wall}} > T_{\text{film}}$), the film thickness would decrease along the stream-wise direction. For condensation, ($T_{\text{wall}} < T_{\text{film}}$), the film thickness would increases along the stream-wise direction.

1.4. PHENOMENON OF WAVES IN FALLING FILMS

When an actual film flow happens over a vertical surface, such as the one shown in Fig. 1.1, in the regions near the liquid inlet the interfacial profile is flat, as considered in the Nusselt theory. The evolution of the so formed waves was the objective of many studies, an overview of which is discussed in section 1.4.4. In Fig. 1.1, three broad categories of interfacial profiles can be seen - (i) flat film; (ii) two-dimensional waves; and (iii) three-dimensional waves. In this report, the term "two-dimensional waves" is used for waves whose height varies only along the streamwise direction. The waves whose height varies along both streamwise and transverse direction are referred to as "three-dimensional waves". This terminology is consistent with the bulk of the literature on falling films.

1.4.1. HISTORICAL BACKGROUND

The first published scientific analysis on waves in a falling film was initiated in a modest circumstance. Russian physicist Piotr Leonidovitch Kapitza (1894 - 1984) refused to work on his country's nuclear weapon project and as a consequence, he was confined to his country house (1946 - 1953) (Kalliadasis et al. (2011)). Unable to continue his prior work on low temperature physics, he ventured into physical problems that he could study with the facilities he had. It was during this time he analyzed the waves on thin films. In his own words - "Ever since the time of Poiseuille this [thin flow of viscous liquid] was considered as a classical case of laminar flow, but I realized that there are a number of indications that this is not so. [. . .] It is rare to discover a new form of wave motion and I decided to look into it." (Boag et al. (2012), p. 388).

The first simplified Navier-Stokes equation to quantify the temporal wave amplitude variation on liquid films was proposed by Benney (1966) and hence known as Benney equation in the literature. This is also referred to as Long-Wave equation. A further simplification of the Long-Wave equation results in the so called Kuramoto – Sivashinsky equation, which is also widely studied (Nguyen and Balakotaiah (2000)). The main phenomenon for enhanced heat and mass transfer was attributed to backflow i.e. re-circulation within the waves. Dietze et al. (2009) used Particle Image Velocimetry (PIV) to visualize the backflow in the capillary wave region of a falling film. One snapshot is shown in Fig. 1.4 for $Re = 10.7$, $Ka = 509$, and the liquid is excited at the inlet with a frequency of 18 Hz.

1.4.2. INSTABILITIES

As a test for instability in a liquid system, a disturbance is given at a particular place at a particular time. If the disturbance grows in time, then the instability is confirmed, and its type is classified as absolute or convective type. In the former, the disturbance grows such that the region of initial instability remains so forever (Fig. 1.5a). In the latter, the disturbance apart from growing in time, also gets transported in space (Fig. 1.5b). The instabilities in the inception region of waves in the falling films is of convective type (Chang (1994)).

1.4.3. MARANGONI EFFECT

Consider a film flow that is initially uniform in thickness along the vertical direction. Let the vertical wall be maintained at a constant temperature of T_{wall} which is considerably higher than the film temperature, but well below saturation temperature of the film T_{sat}. A sinusoidal disturbance is introduced by external means, resulting in the film thickness to vary as shown in Fig. 1.6a. The heat from the wall transfers to the film. At the troughs, since the film thickness δ is relatively less, it offers less thermal resistance to heat flow when compared to the crests. So the film temperature at the liquid-vapour interface is higher at troughs than in crests, which

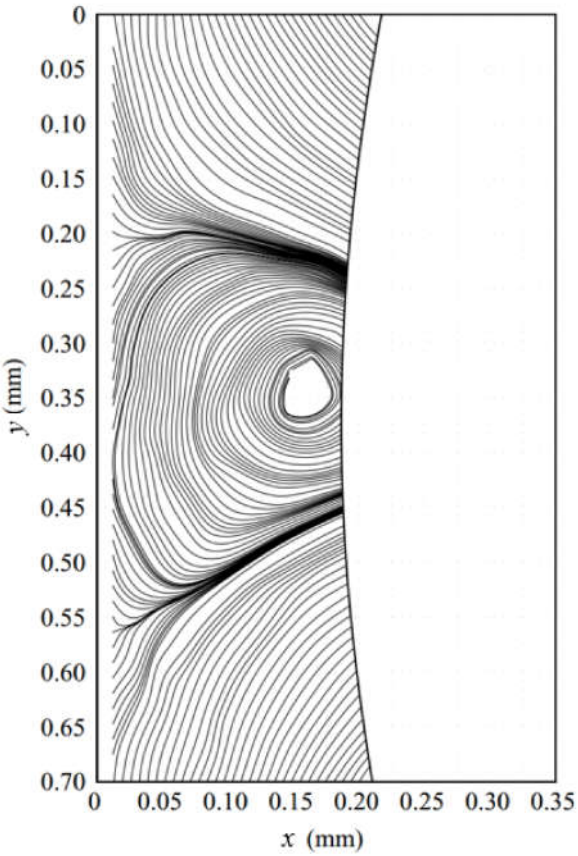

Figure 1.4: Experimental visualization (PIV) of streamlines at Re = 10.7 showing the region of re-circulation in the capillary wave region of a falling film obtained by Dietze et al. (2009). The liquid used is aqueous solution of dimethylsulfoxide, Ka = 509. The liquid at inlet is excited with a frequency of 18 Hz.

(a) Absolute Instability

(b) Convective Instability

Figure 1.5: Instabilities in a liquid system.

is shown in Fig. 1.6b. For most of the liquids, surface tension σ decreases with increasing temperature. So there exists a variation in surface tension as shown in 1.6c. Due to this, the liquid from troughs (where σ is relatively less) is pulled towards the crests (where σ is relatively more) due to the force imbalance. The action of the net force on the film interface (without considering the effect of gravity) is marked by the black colored arrows in 1.6d. From 1.6d it is also seen that, the liquid from troughs moves towards crests in both direction, i.e. upwards and downwards. However, the downward movement has the support from gravity, while the upward

movement have to overcome the gravity force. So depending on the scale of surface tension force present in a particular flow condition, the direction of liquid movement is affected. In any case, the movement of liquid from troughs to crests would happen. Thus the variation in surface tension enhances the wavy pattern of the liquid-vapour interface. This effect is known as Marangoni effect, named after Sir Carlo Giuseppe Matteo Marangoni (1840 – 1925), an Italian Physicist who studied extensively about interfacial phenomenon in liquids (Kalliadasis et al. (2011)).

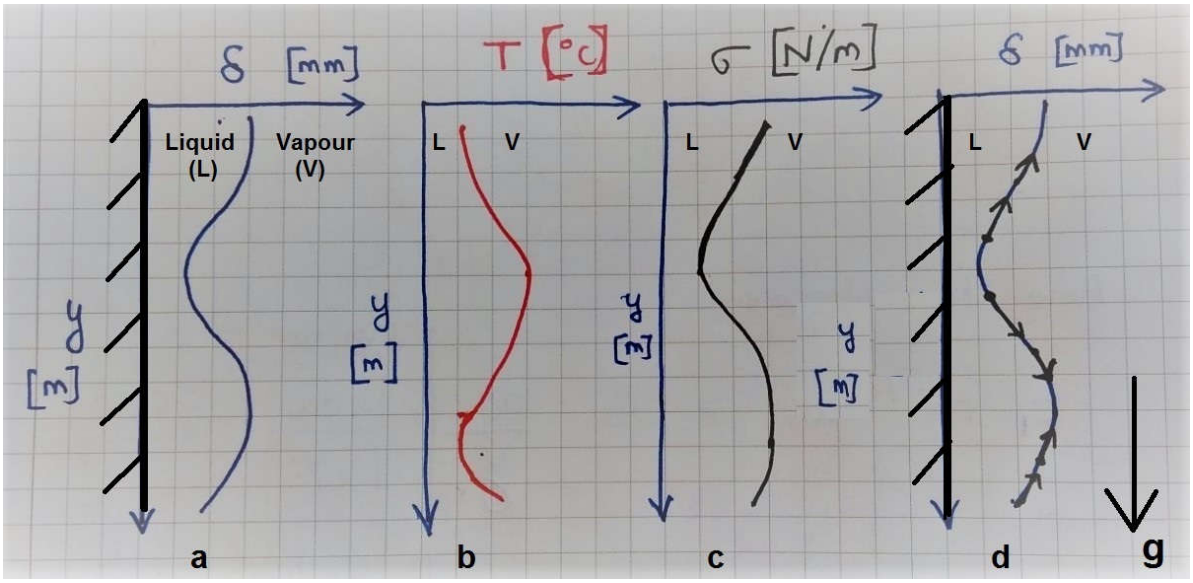

Figure 1.6: Marangoni Effect: (a) The variation of film thickness along the vertical direction (b) causes a corresponding variation in the Temperature at the liquid-vapour interface. (c) The variation in temperature causes surface tension gradient at the liquid-vapour interface. (d) This causes a force imbalance in the interface, which is denoted by black colored arrow marks superimposed on the interface. This leads to further thickening of crests and thinning of troughs.

1.4.4. WAVE EVOLUTION IN VERTICAL FALLING FILMS

An extensive review and characterization of vertical falling films is provided by Chang (1994) and a brief overview of it is presented in this section. The flow *Re* can in general be divided into 4 ranges. At *Re*«1, the film often ruptures, as the inter-molecular forces dominates. At 1200<*Re*<4000, the wave evolution is non-stationary making it difficult to characterize. At *Re* > 4000, turbulence dominates the interfacial dynamics. So the wave characteristics are not observed. The behaviour of waves is different at different flow rates (*Re*). An overview of the main differences in wave types, instabilities and general behaviour are described in Table 1.1.

At 1<*Re*<1200, which is the interest of the present work, the wave evolution is typically categorized into 4 regions (R1 - R4) along the stream-wise direction. The length of these regions vary depending on the flow conditions. For water films, each of the regions R1 to R3 has a span of ≈ 10 times the wavelength of the wave formed in the inception region, while R4 extends indefinitely. The instabilities that leads to wave formation in films could be due to natural disturbances in the system or by externally forced disturbances.

Irrespective of the amplitude and frequency of the applied disturbance, a uniform wave field emerges at the end of R1 and R2. However, there is a difference between the broad-banded small amplitude disturbance, and periodic high amplitude disturbance. In the former, the uniform wave field that emerges is independent of the forcing disturbances, and the linear and non-linear selection mechanisms of R1 and R2 uniquely determines it. In the latter, the frequency of the waves present in the uniform wave field matches with the forcing frequency. The wave amplitude grows exponentially in R1 with the instability mechanism being convective. However the growth is restricted due to non-linear effects in R2 and the amplitude saturates to a finite value characterized by wave number, *Re*, and *Ka*. At the end of R2, the waves are subjected to two kinds of instabilities - (i) sub-harmonic instability: neighbouring waves coalesce at intermittent locations and (ii) sideband instability: long-wave modulation appears. In an otherwise uniform wave field, these two instabilities cause a kind of defective patches. Within these, the distorted waves grow in amplitude, speed, and evolves into

characteristic humps which is spatially localized. These humps have a steep upfront, and they expand in the downstream direction. These are also known as solitary humps due to presence of relatively long (when compared to the characteristic length of the humps) flat film between the humps. Finally in R4, merging of the humps in transverse direction occurs, while retaining their solitary character.

Table 1.1: Evolution of waves at different *Re* (Chang (1994))

	***Re*«1**	**1<*Re*<1200**	**1200<*Re*<4000**	***Re*>4000**
Type of waves observed	Film is very thin.	Long interfacial waves	Long interfacial waves	Short wavelength waves
Wavelength		Order of magnitude higher than the film thickness.		Comparable to or shorter than the film thickness.
Instabilities are caused by		Gravity capillarity effects	Gravity capillarity effects	Tollmien–Schlichting
Remarks	The film is so thin that the intermolecular forces and contact line dynamics dominates and the film ruptures.	Refer section 1.4.4	Wave dynamics are extremely non-stationary, especially by short waves that are produced by vortex shedding of long waves.	The interfacial dynamics are enslaved by internal disturbances.

1.4.5. SLOPE OF THE WAVE SURFACE

Karapantsios and Karabelas (1990) studied the interfacial characteristics of large inertia-gravity waves (also known as roll waves) in vertical film flows of water for *Re* in the range 500 to 13000. Their experimental setup consisted of a vertical tube with inner diameter of 50 mm and the thickness measurements were recorded at ≈ 2.5 m from the liquid inlet using two conductance probes which were placed 6 cm apart along the flow direction. The plot of thickness time series for the case of $Re = 6680$ is shown in Fig. 1.7, where one of the roll wave is indicated by an arrow. They claimed that with the available experimental data, the roll waves travels at constant celerity. One part of their study focused on the interfacial slopes at the wave front and back. They related their thickness time series to the interfacial slope using the Eq. 1.7.

$$\frac{\partial h}{\partial t} = P \cdot \frac{\partial h}{\partial y} \tag{1.7}$$

where, h is the film thickness, P is the phase velocity of the waves, and y represents the stream-wise direction.

For the roll wave identified by an arrow in Fig. 1.7, the temporal film thickness variation ($\frac{\partial h}{\partial t}$) with film thickness ($h$) is presented in Fig. 1.8. Karapantsios and Karabelas (1990) referred to them as "spatial evolution portrait" of the film. From Fig. 1.8, it is inferred that the temporal thickness variation ($\frac{\partial h}{\partial t}$) is initially high, then reaches a maximum, after which it starts to decrease. This is observed at both upstream and downstream locations. The part of the plot that has increasing values of $\frac{\partial h}{\partial t}$ indicates the arrival of the roll wave wherein the film thickness increases with time at a stationary location (as recorded by the conductance probe), i.e. front of the roll wave. The part corresponding to decreasing values of $\frac{\partial h}{\partial t}$ indicate the back portion of the roll wave, where the thickness decreases with time. The values of $\frac{\partial h}{\partial t}$ at the front (≈ 410 mm/s) of the roll wave are steeper than at the back (≈ 250 mm/s). The authors use this inference, along with Eq. 1.7 to state that the slope of the wave surface ($\frac{\partial h}{\partial y}$) at the front is steeper than the wave surface at the back of the roll wave.

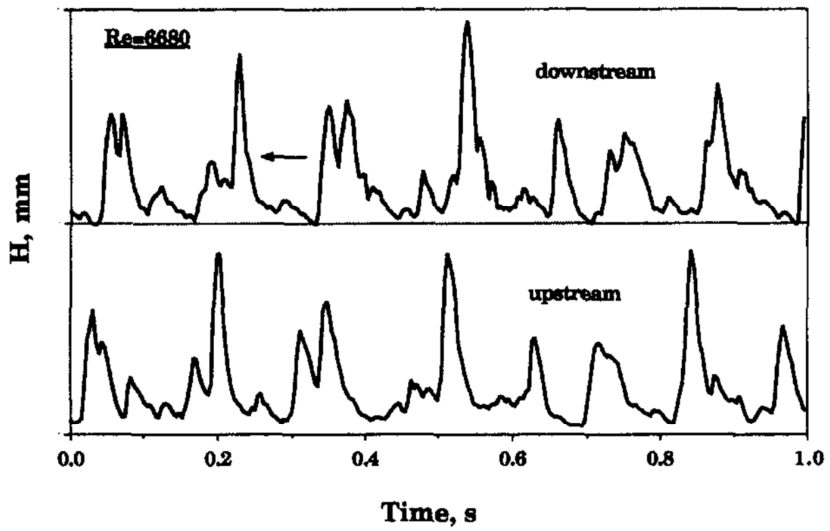

Figure 1.7: Time series of thickness measurements recorded by Karapantsios and Karabelas (1990) using two conductance probes placed at 6 cm apart in the stream-wise direction at a distance of ≈ 2.5 m from the liquid inlet. Recording frequency is 500 Hz. (Note: Only digitized version of the research article was accessible, and the values of the vertical axis was not present in it. However, from Fig. 1.8, the range for vertical axis is expected to be 0 to 4 mm.)

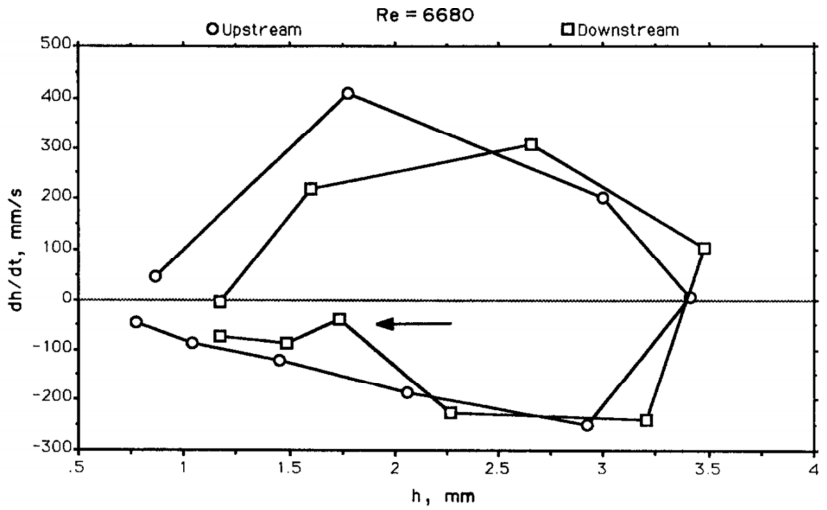

Figure 1.8: Plot of temporal variation of film thickness ($\frac{\partial h}{\partial t}$) with film thickness ($h$) for the roll wave identified by an arrow in Fig. 1.7, obtained by Karapantsios and Karabelas (1990).

1.5. NON-CONTACT MEASUREMENTS

With advancement in optical techniques, contactless measurement techniques such as Laser Induced Fluorescence (LIF) and Particle Image Velocimetry (PIV) were used. LIF is used to quantify the scalar variables such as film thickness, temperature, while PIV is used to measure vector variables such as velocity distribution along a plane. These techniques offer the advantage of not disturbing the film flows which is otherwise present with the usage of conductance or needle contact probes.

Using LIF, measurements can be taken at a single point, along a line or along a surface. Kockx et al. (2005) used LIF for one-point thickness measurement of the falling film around a stationary Taylor bubble. Schubring et al. (2010) measured film thickness along a line to study the effect of gas flow on the liquid-vapour interface of thin film flows. Alekseenko et al. (2012) utilized LIF to visualize the three-dimensional shapes of the waves formed in annular gas-liquid films flows.

1

1.5.1. THREE-DIMENSIONAL WAVE SHAPE

Regarding the shape of the three-dimensional waves on falling films, Kharlamov et al. (2015) notes that for *Re* ~ $\mathcal{O}(10-10^2)$ there exists two possible candidates in the literature - (i) horseshoe shaped wave (also known as Λ solitons); and (ii) streak-like wave. These are shown in Fig. 1.9. A notable difference between them is, in the case of (i), the film thickness in the upstream region of the crest is lower than the film thickness in the undisturbed region, while in the case (ii) it is opposite.

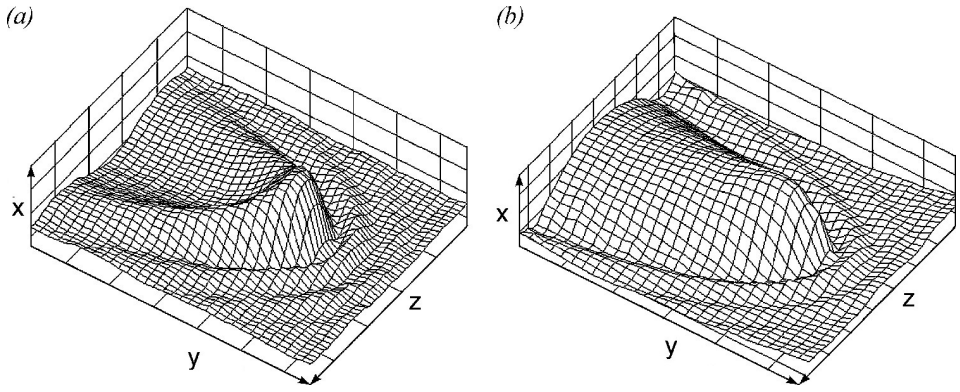

Figure 1.9: (a) Horseshoe shaped wave in which the film thickness in the upstream region of the wave crest is lower than the undisturbed film thickness. (b) Streak-like wave in which the upstream region of the wave crest is higher than the undisturbed film thickness (Kharlamov et al. (2015))

Demekhin et al. (2010) performed experiments on falling film of water on a vertical plane surface with a height of 25 cm and width of 15 cm for the *Re* in the range 20 - 400. In order to obtain the three-dimensional wave, they adopt the so called "rain drop" method. In this method, a drop of test liquid is introduced to the undisturbed film surface as shown in Fig. 1.10. The mass of the deposited drop equals the mass of the theoretical three-dimensional wave which is calculated from Demekhin et al. (2007). The reason for using rain-drop method is to bypass intermediate stages of film evolution, and the idea of using such a technique, the authors state, was prompted by the rain drops on the windscreen of a car during a traffic jam. The shape of the wave obtained from their experiments and theoretical calculations are shown in the Fig. 1.11. It resembles the horseshoe structure shown in Fig. 1.9.

Kharlamov et al. (2015) studied the transition characteristics from two dimensional to three dimensional waves in a film falling on a vertical plate with a height of 140 cm and 45 cm in width. The range of *Re* investigated was 16 - 560. The test liquid used was water (*Ka* = 3660). They studied the transition effects due to natural noise (i.e. no externally induced noise) driven flow as well as due to a modulated inlet mass flow rate. In both the cases, the shape of the three-dimensional wave obtained (at a distance of 120 cm from liquid inlet), which is shown in Fig. 1.12, resembled streak-like waves. Such waves were also obtained using numerical simulations, as shown in Fig. 1.13, by Dietze and Kneer (2011) for *Re* = 237 and *Ka* = 3940.

To the best extent of the knowledge of the present author, there were no studies that focused on investigating the three-dimensional wave shapes for low *Ka* liquids.

1.5.2. OTHER CHARACTERISTICS

Alekseenko et al. (2012) utilized three-dimensional LIF technique to study the wave characteristics with and without liquid entrainment in the core region of the tube. The wave characteristics studied were primary and secondary waves, also known as ring waves and ripples. They observed that for regime without liquid entrainment, the degree of circumferential uniformity was higher than for regime with entrainment. So they suggest that, two-dimensional measurement technique would be preferable for the former, while a three-dimensional technique should be considered for the latter regime.

Koizumi et al. (2009) studied using PLIF the wave characteristics for counter-current flow of water and silicone oils as the liquid, while air was used for the gas phase.The flow happened along a vertical tube with inner diameter of 30 mm and 5.4 m in length. The range of film Reynolds number tested were .06 to 9000. They obtained correlations which predicted the wave velocity and maximum film thickness to an accuracy of 15 % for their experimental values and three other studies, while one other experimental study fell well outside this

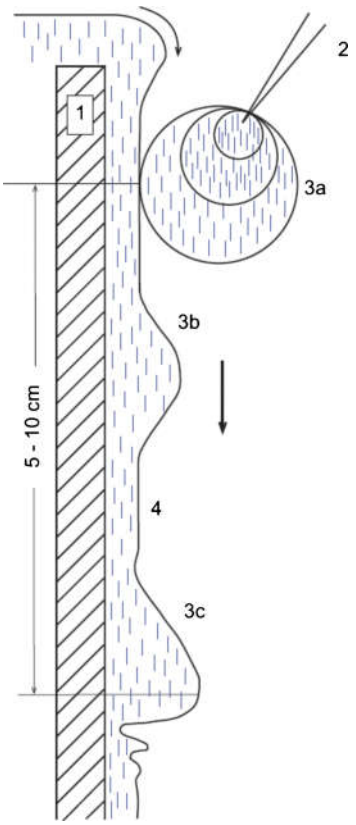

Figure 1.10: Illustration of the rain-drop method utilized by Demekhin et al. (2010). (1) Test section; (2) pipette with adjustable drop-volume though which the liquid is introduced to the film; (3a) Drop increases in size and touches the liquid surface and becomes a part of the film; (3b) Introduced drop spreads over and turns into an evolving localized signal downstream; (3c) The drop finally becomes a stationary running Λ wave; (4) liquid layer flowing downstream.

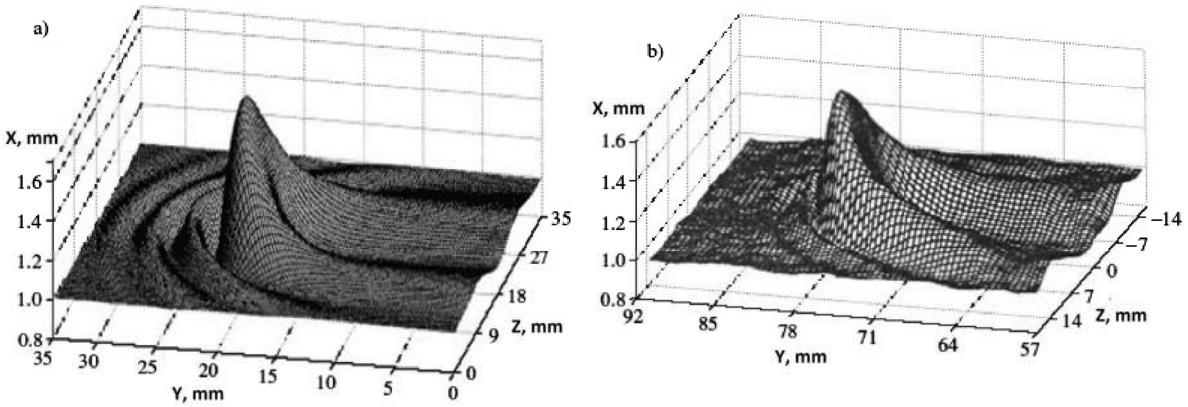

Figure 1.11: Three-dimensional wave shape obtained by Demekhin et al. (2010) from their (a) theory, and (b) experiments. $Re = 16$ and $Ka = 404$. The flow is excited using rain-drop method which is illustrated in Fig. 1.10. The wave shape resembles horseshoes like wave shown in Fig. 1.9.

accuracy range. The reason was hypothesized to the difference in the measurement techniques used.

Kharlamov et al. (2015), whose experimental details were explained in section 1.5.1, observed the formulation of rivulets in the transverse direction during the transition from two dimensional to three dimensional flows in falling films. In the time averaged film thickness field, at location nearer to the inlet (35 cm from inlet), no visible rivulets were formed in case of natural noise driven flow. However, with external forcing rivulets with height variation in the transverse direction of 0.02 mm from mean thickness (≈ 12 %) were observed.

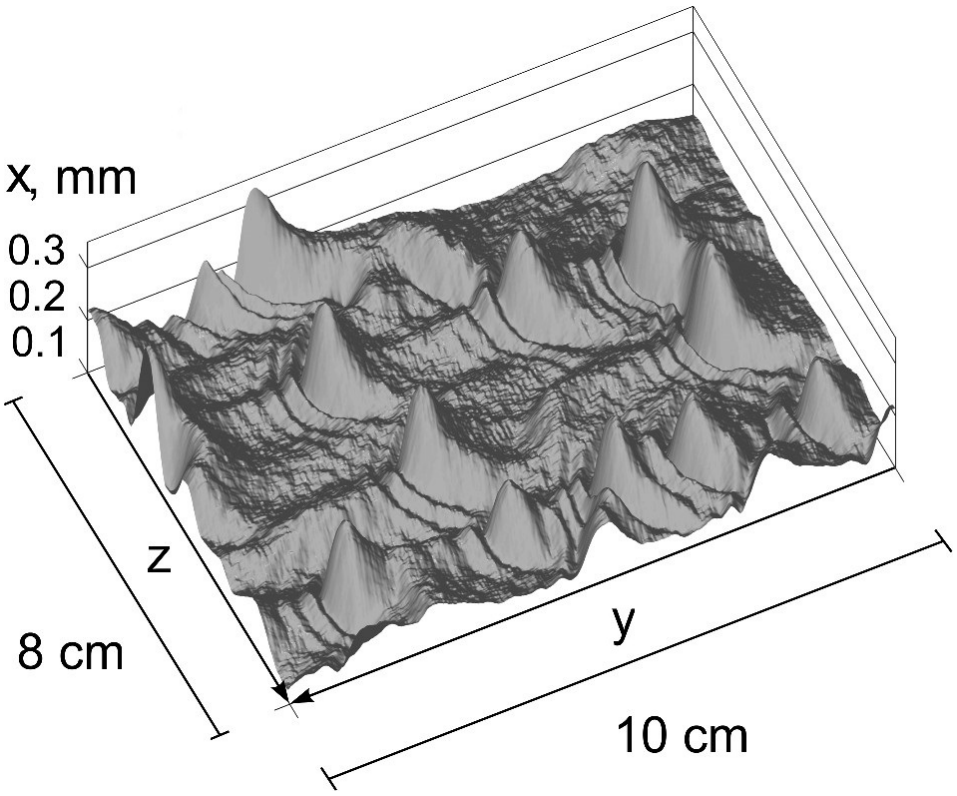

Figure 1.12: Three-dimensional wave for the case with no externally induced disturbances experimentally obtained by Kharlamov et al. (2015) for $Re = 56$ and $Ka = 3660$. The stream wise direction is located at 120 cm from the inlet. The film thickness at the back of the wave crest is higher than the unperturbed film thickness. So it resembles streak-like structure shown in Fig. 1.9.

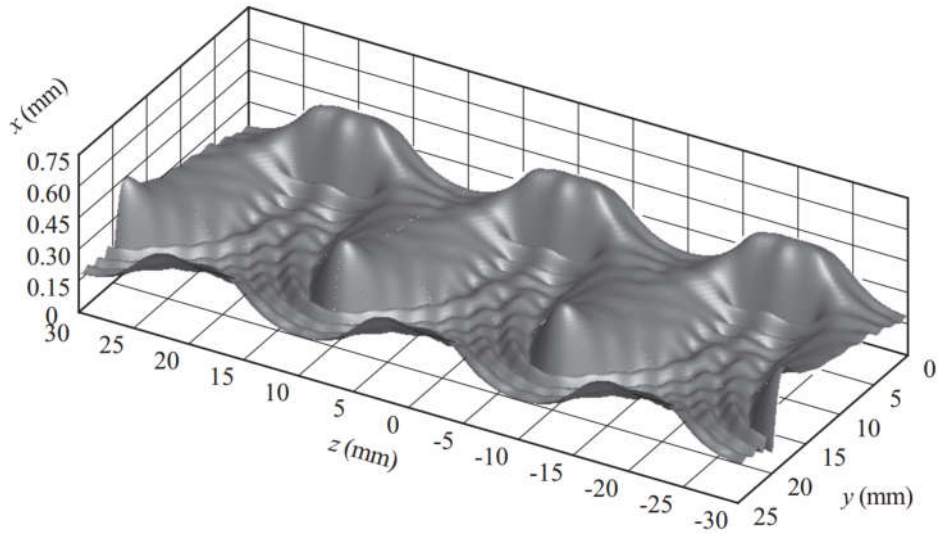

Figure 1.13: Streak-like three-dimensional waves numerically obtained by Dietze and Kneer (2011) for Re= 237 and Ka = 3940.

At distances further downstream (120 cm from inlet), rivulets were observed for both the cases as shown in Fig. 1.14.

Recently, Mendez et al. (2017) notes the absence in literature regarding detailed two-dimensional wave characterization for low Kaptiza number (in the order of 1) liquids falling vertically. Also, due to lack of extensive experimental data for low Kaptiza number liquids, the validity of lower-dimensional theoretical models for film flows are yet to be verified. They studied (Fig.1.15) the spatio-temporal variation of film thickness for

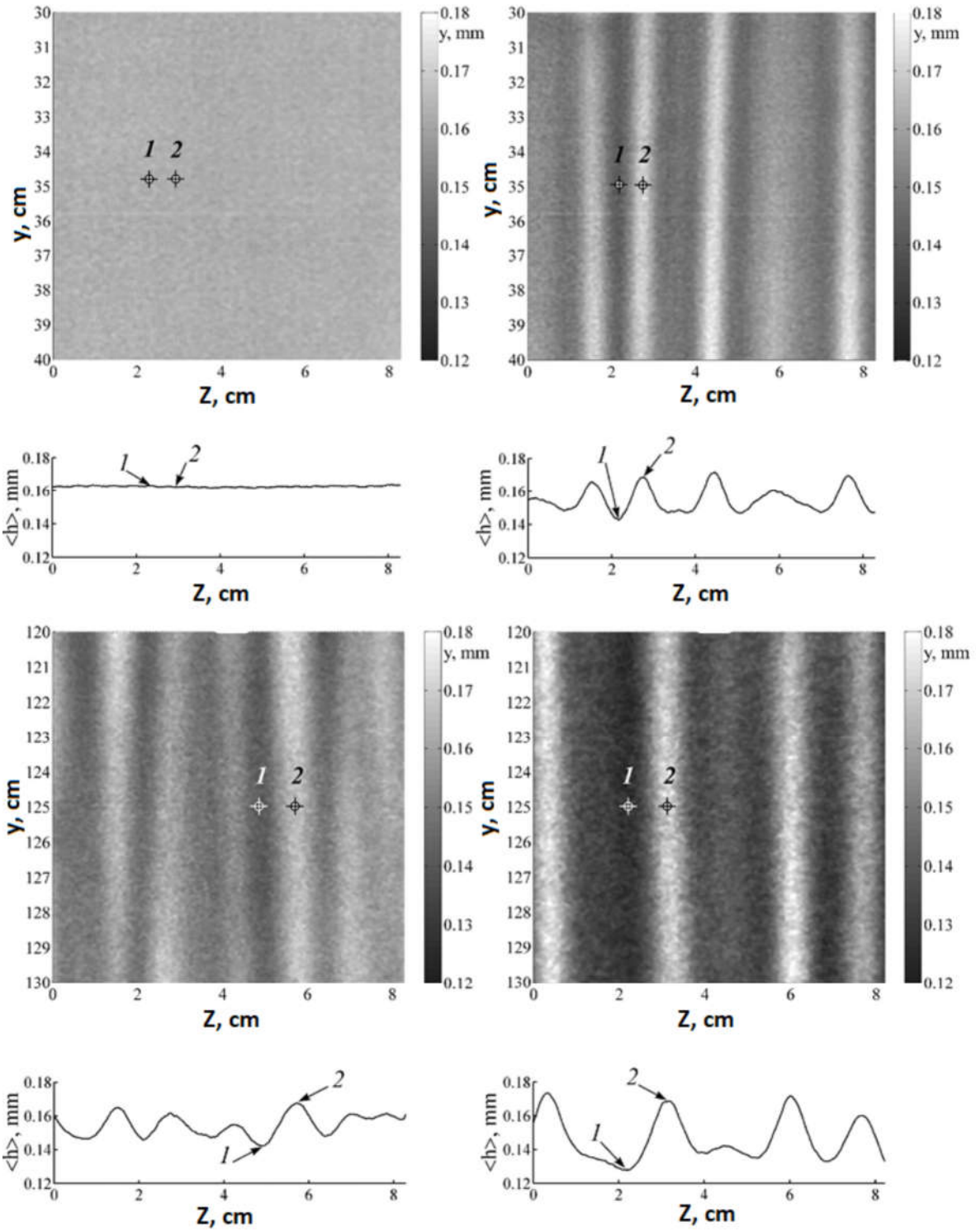

Figure 1.14: Rivulet formation in falling films. The *Re* of the flow is 56, while *Ka* = 3660 (water). The top two images corresponds to measurements taken at 30 to 40 cm downstream, while the bottom two is taken at 120 and 130 cm downstream from the inlet. The graph shows the thickness variation along the transverse direction. The images on left correspond to natural wave evolution, while the images on the right corresponds to forcing frequency of 6 Hz (Kharlamov et al. (2015)).

Dipropilene Glycol ($Ka = 3.7 \pm 2\%$), with the flow along a vertical plate. Light adsorption technique was used for thickness measurement. The Reynolds number studied were in the range of 4 to 24, while the liquid flow rate

was pulsated in the frequency range of 12 to 24 Hz. They provide correlations for wavelength, wave velocity and wave peak. Additionally, they provide a correlation for wave profiles, in which a piece-wise exponential function is used to describe the wave shape, with the parameter values for the equation given as a function of operating conditions. Their study was confined to two-dimensional waves on vertical falling films.

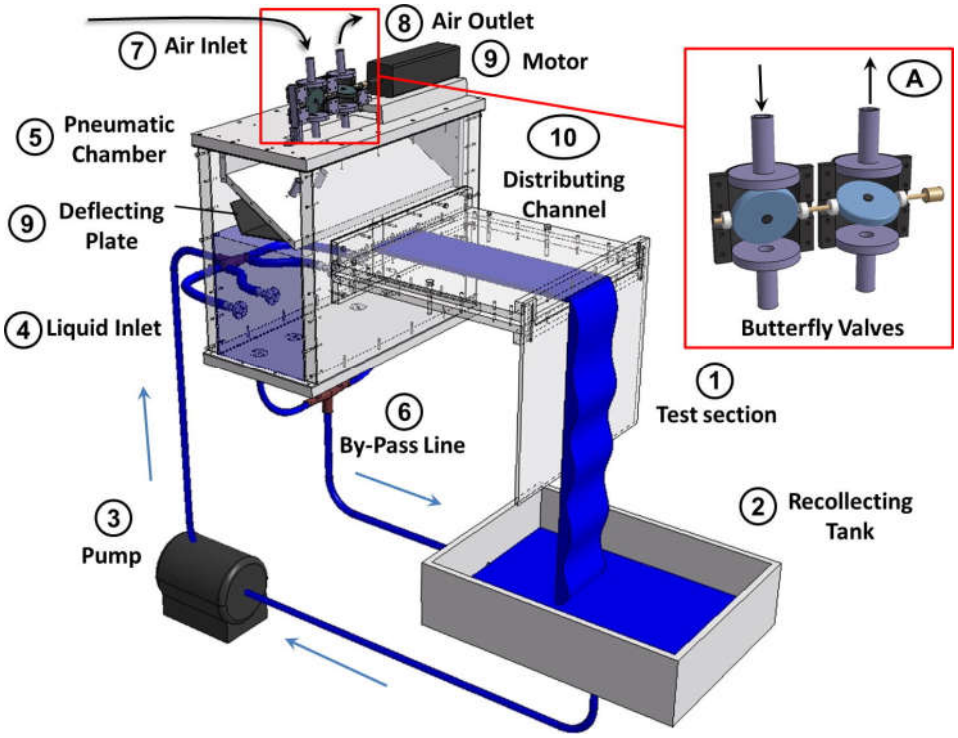

Figure 1.15: Experimental setup used by Mendez et al. (2017) for measuring the spatio-temporal variation of wave thickness for low-Kapitza number liquid - Dipropilene Glycol, $Ka = 3.7$.

1.6. RESEARCH OBJECTIVE

The temporal and spatial evolution of the waves on falling films are extensively measured and characterized through experiments for a wide range of $Re \sim \mathcal{O}\left(10-10^4\right)$. A majority of these studies utilizes film thickness measurements at a point or along a line. Film flows that is of industrial interest are three-dimensional, and this necessitates film thickness measurements along a surface. Such studies are needed to validate existing mathematical models, and if need be, to provide data for improving the models. In the past five years, experimental studies using various optical techniques were used to provide such three dimensional reconstruction of the instantaneous film thickness. These and prior experiments using contact measurement techniques, were comprehensive in providing the required experimental data for the low viscosity liquids ($Ka \sim \mathcal{O}\left(10^2-10^3\right)$). The available literature data on wave thickness, shape, and their statistical character for high viscosity liquids ($Ka \sim \mathcal{O}(1)$) are scarce (Mendez et al. (2017)). Adding to this, a recent discovery by Kharlamov et al. (2015) reveals the presence of rivulet structure in the transverse direction on time averaged film thickness field, for a vertically falling liquid film, which is not determined in existing mathematical models. It is with this background, the present work focuses on provision of the wave dynamics data using laser induced fluorescence technique for viscous liquids ($Ka \sim \mathcal{O}(1)$) at low Re ($\sim \mathcal{O}(10)$). More specifically, the objectives are:

1. Design and fabrication of a laboratory scale vertical falling film setup.
2. Implementation of a technique to quantitatively visualize the liquid-vapour interface of a film flowing along the inner circumference of a pipe.
3. Characterize the shape of the waves obtained, and perform statistical analysis on the film thickness field to understand their behaviour.

2

Experimental Setup Design

This chapter begins with an overview of the liquid film flow setup. Laser Induced Fluorescence (LIF) is utilized to visualize the film thickness over a curved surface of the pipe and the details of the optical system are described in section 2.2. It is followed by the discussion on the selection of dye concentration in section 2.3. The calibration process and the methodology used to obtain the film height from fluorescence intensities are described in section 2.4 and 2.5 respectively. The chapter ends with the discussion on the uncertainty in the film thickness measurements.

2.1. OVERVIEW OF THE EXPERIMENTAL SETUP

A schematic and an actual image of the experimental setup is given in Fig. 2.1. The liquid to be formed as a film is pumped from the reservoir to the liquid distributor. Here the liquid enters a converging section, at the end of which it enters the pipe's inner circumference as a film. Detailed description of the liquid distributor is given in section 2.1.1. The film then flows through a vertical plexigas pipe with an inner diameter of 62 mm (± 0.5 mm) and length of 2 m. Finally the liquid exits the pipe and reaches the reservoir, thus completing the loop. The outlet of the pipe is placed above the liquid's top surface in the reservoir so that when the liquid is sucked from the reservoir, the suction is not transmitted to the pipe. The pipe's inner diameter is selected to match with an adjacent facility with which it is to be merged for studying the effects of heat transfer at large distances from the liquid inlet (≈ 8 m), which is of industrial interest. The liquid distributor has provision for passing hot air through the pipe center, and this enables to include the effect of evaporation in the future experiments.

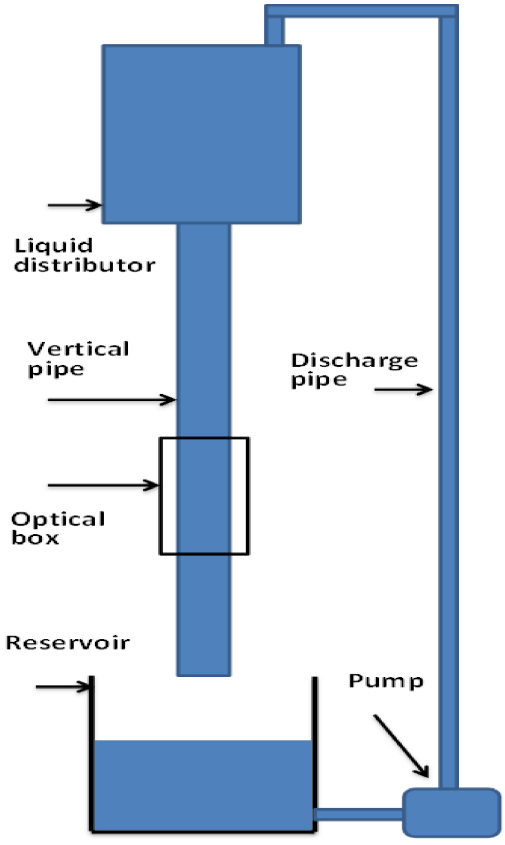

(a) Schematic representation of the experimental setup.

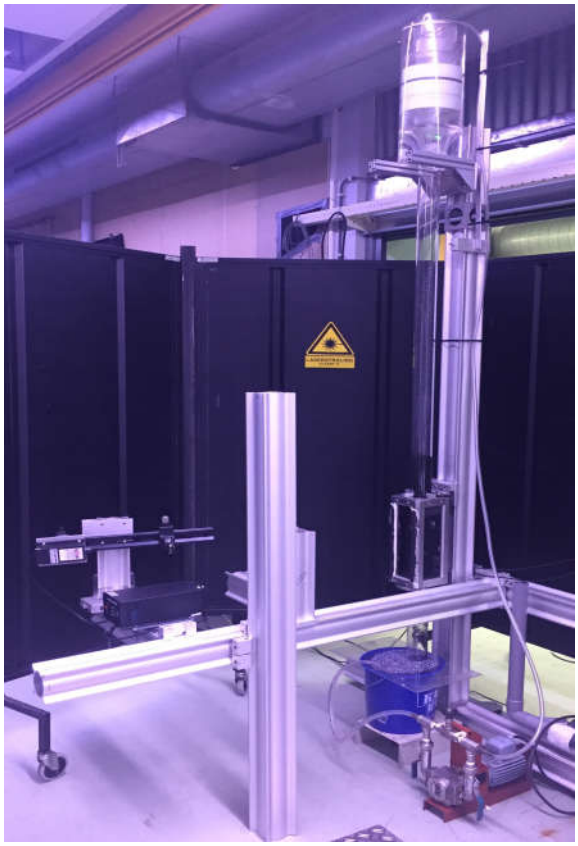

(b) Picture of the experimental setup.

Figure 2.1: Schematic and an actual view of the experimental setup.

2.1.1. LIQUID DISTRIBUTOR

The liquid distributor is shown in Fig. 2.2. It consists of 5 parts - the outer casing, the buffer zone, the slit adjuster, the porous structure, and the converging section. The buffer zone has a circumferential volume of 1 litre, and is mounted in a concentric manner to the outer casing. The liquid from the reservoir falls initially to the buffer zone. Upon filling the volume, it flows through the radial clearance between the buffer zone and the slit adjuster, to the porous structure to reduce the irregularities in the flow. The buffer zone is used due to two reasons - (i) to avoid the impinging action of the liquid, as it would result in unequal flow through the slit at the bottom; (ii) to uniformly distribute the liquid entering the porous structure. The liquid then enters the converging section, where the slit adjuster is placed such that a radial clearance - "r" is formed between them. The liquid flows through the radial clearance "r", and enters the pipe as a circumferential film. The slit adjuster is radially positioned by the porous structure and axially positioned by means of 3 screws at the top. The latter allows in obtaining variation in "r" by adjusting the axial position of the slit adjuster.

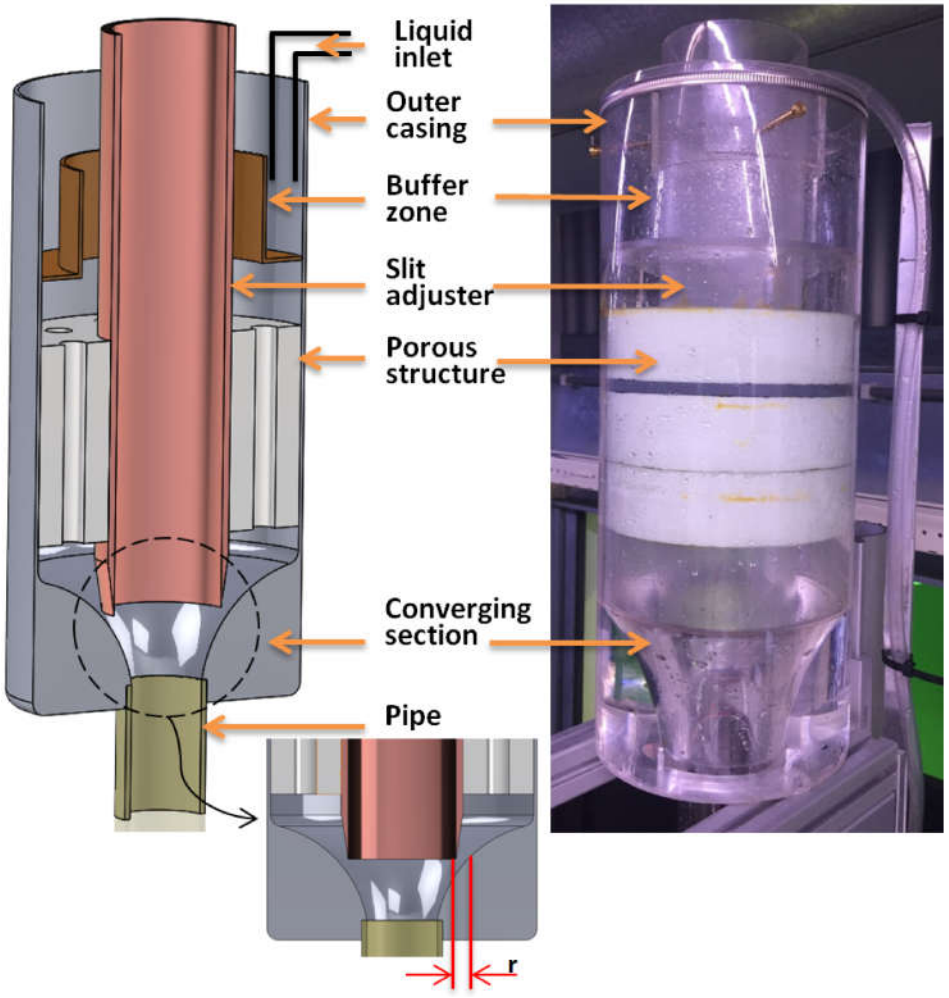

Figure 2.2: Schematic sectional and an actual view of the liquid distributor.

2.2. OPTICAL SYSTEM

2.2.1. LASER INDUCED FLUORESCENCE - INTRODUCTION

Fluorescence is one of the three ways in which the electron from an excited state comes back to the original state. The other two methods are radiationless collisional quenching and phosphorescence (Laufer (1996)). The excitation is caused by a laser light, and hence the term laser induced fluorescence. The resulting fluorescence intensity depends on the concentration of the dye, the intensity of the exciting light, and the thickness

of the film. A quantitative description of the process involved is presented in the Appendix C.

The pH and the temperature of the liquid-dye mixture also affects the fluorescence. However, for rhodamine WT (section 2.2.2), the dye utilized in the present experiment, the fluorescence is stable in the pH span of 5 to 10 (Wilson et al. (1986)), which is the range used in the present study. The liquid is not subjected to any external heating source. However, the temperature of the liquid may rise ($\sim \mathcal{O}\left(1^{o}C\right)$) due to friction in the pump. To account for this, experimental recordings are performed after a period of 30 minutes from the time the pump is turned on. Any temperature rise of the liquid would stabilize during this period.

The fluorescence is recorded by a camera with a band-pass filter which blocks the (reflected) laser light. Hence the recorded intensity, in addition to the above factors, also depends on (i) the focal length of the lens, (ii) aperture, (iii) shutter speed, (iv) sensor sensitivity, and (v) filtering efficiency of the band-pass filter. A majority of these are fixed, and only the aperture and the shutter speed can be varied.

2.2.2. SELECTION OF DYE

The liquid used to create a film in the present work is the water-glycerine mixture, to which a fluorescent dye is mixed homogeneously. The following are the desirable characteristics of the fluorescent dye:

1. Since the primary objective of the present work is amplitude measurement, it is important that the fluorescence emitted by the dye is a strong function of the film thickness, for a constant dye concentration.

2. The peak of the absorption and the emission spectra must be separated by sufficient distance to avoid emitted fluorescence from being absorbed by the dye.

3. The toxicity should be low.

4. The future vision is to extend the present work to study the effect of viscosity gradients in cross-stream direction on wave dynamics. These viscosity gradients are present due to concentration gradients that are caused due to heat transfer. Hence it is preferable that the selected dye is suitable for simultaneous measurement of film thickness, temperature, and concentration gradient.

5. The dye should not have photo-bleaching effect for the selected laser intensity.

6. The selected dye's absorption maxima should coincide with the available laser light's wavelength.

Of the many possible choices, Smart and Laidlaw (1977) made an extensive analysis of eight commonly used fluorescent dyes that included fluorescein, rhodamine B, and rhodamine WT. Among them, rhodamine B and rhodamine WT had high sensitivity. Toxicity of rhodamine B is more when compared with rhodamine WT. One reason for this is due to the rhodamine B's cationic nature, which causes it to be readily absorbed by the living tissues, and also gets adsorbed to the container in which they are stored, as many solid surfaces have negative charges on them (Smart and Laidlaw (1977)). For example, Yotsukura et al. (1970) reported that the adsoprtion loss of rhodamine B stored in glass bottles was significant. They were not able to arrive at a quantification of the adsorption loss, but concluded that they are "probably important". Due to this, the concentration of the dye could be different at different periods of experiments, making it difficult to use rhodamine B for quantitative measurements. Rhodamine WT being anionic, does not suffer from such adsorption losses. Hence, owing to the aforementioned reasons, rhodamine WT is selected as the fluorescent dye.

2.2.3. SELECTION OF LASER

For the light source, either (i) pulsed, or (ii) continuous laser could be used. In addition, the laser rays should have sufficient intensity (which is proportional to the laser power) such that the resulting fluorescence intensity is sufficient to obtain clear recordings at the selected frequency. Based on the availability, a 500 mW, 532 nm continuous laser is used.

2.2.4. CAMERA

The temporal resolution of the measurements is determined by the camera's frame rate (number of images the camera can capture per second, also known as Frames Per Second (FPS)), and the exposure time. By default, the exposure time is inverse of FPS. Exposure time can also set to be lower than 1/FPS, to achieve blur-free

images. This is used when a higher time period of recording is required, since the camera normally has a fixed internal memory. There is a lower limit to the exposure time, since the the amount of fluorescence intensity entering the camera is proportional to the exposure time. The following parameters were considered when selecting the FPS and exposure time for the experiments:

- The recorded images of the film flow should not be blurred. This was achieved when the recording was performed such that the distance travelled by the waves between successive frames was less than ≈ 3.5 mm for $Re \approx 32$.
- The maximum concentration of the dye used is limited by two types of saturation. One is the saturation in the fluorescence intensity emitted by the liquid-dye mixture for the range of film thickness considered in calibration (discussed in section 2.4). Other is the saturation in the fluorescence intensities as recorded by the camera for the range of film thickness considered. For example, at a certain dye concentration, even though the fluorescence intensity emitted by the liquid-dye mixture would be different for two different film thickness, the fluorescence intensity as recorded by the camera could be the same, if a large exposure time is used. Similarly, if a very low exposure time is used, the recorded fluorescence intensity would not be a strong function of the actual fluorescence intensity emitted by the liquid-dye mixture. So the dye concentration used places a limit for the range of FPS and exposure time that can be selected.

Based on the above parameters, trials with different possibilities were performed, and the optimum value was found to be 250 Hz with an exposure time of 1/400 s. The camera used is Photron Fastcam APX RS. It has a resolution of 1 megapixel and can record for 24 seconds for the chosen FPS.

2.2.5. POSITION OF CAMERA IN THE SETUP

Regarding the position of the camera, it is preferable to have the distance between the measurement section and the camera as far as possible ($\sim \mathcal{O}(10cm)$). This is to ensure the fluorescence rays are as paraxial as possible. The camera-lens arrangement used in this setup is of fixed focal length type.

(a) Camera is focused to the tube front resulting in the rear to be blurred.

(b) Camera is focused to tube rear resulting in the front to be blurred.

Figure 2.3: Illustration of the effect of camera being focused at the tube front and rear, where the tube's outer surface is wrapped with a printed sheet.

So to use the camera at farther distance from the measurement section, a lens with higher focal length is desired. The lens with highest focal length available during the time of experiment was 55 mm, and the same is used. The camera is placed at a horizontal distance of 40 cm from the vertical pipe. The vertical position of the camera was 1.5 m from the liquid inlet, where long wavelength three-dimensional waves were observed,

which is the interest of the present study. The measurement area is 70 mm x 70 mm. Owing to the curvature, a section of the pipe would not be in focus, and this is illustrated in Fig. 2.3. For optical access, the measurement region of the tube was enclosed with water filled glass box.

2.3. SELECTION OF DYE CONCENTRATION

In order to determine the dye concentration, it is preferable to have a film of increasing thickness so that the effect of both - dye concentration and film thickness, on the fluorescence intensity can be obtained simultaneously. A cone shown in Fig. 2.4 is used to obtain a film of increasing thickness. It is inserted into the tube and is held in position by two O-rings at its bottom that makes an interference fit with the tube. This creates a radial clearance between the outer circumference of the cone and the inner circumference of the tube, that increases in the axial direction. Initially a low concentration of the dye is mixed with the liquid - 0.004 ml of dye/liter of liquid, and is filled in the radial clearance. The laser rays, after a warm-up period of 30 minutes, is allowed to fall on the measurement area and the resulting fluorescence is recorded by the camera. To account for temporal fluctuations in the laser rays, a series of 200 frames were recorded, and it is averaged to a single image. The resulting fluorescence intensity along the cone center is plotted in Fig. 2.5. The radial clearance increases from 0.7 mm to 4.3 mm, which is plotted along the horizontal axis, while the resulting fluorescence intensities are plotted along the vertical axis. The concentration of the dye is increased in 7 steps to 0.357 ml of dye/liter of liquid, and the resulting fluorescence intensity is also plotted in Fig. 2.5. The different dye concentrations are identified as A to H. Before each measurements with the different dye concentrations, the cone and the inner surface of the tube was thoroughly cleaned.

Figure 2.4: Cone used for dye concentration test.

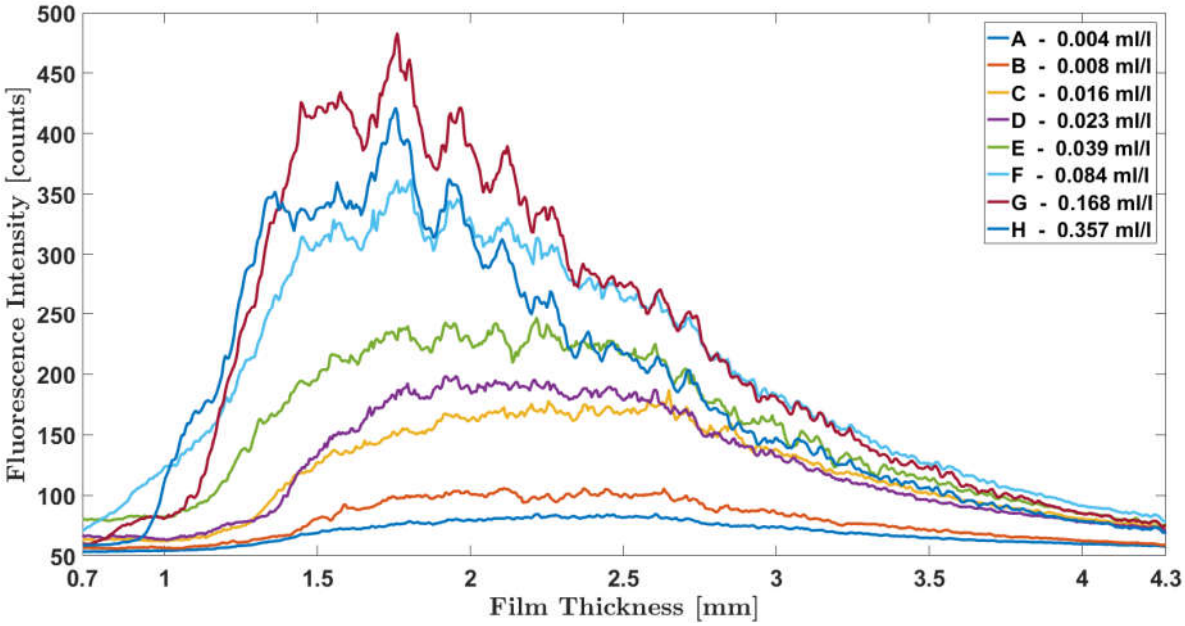

Figure 2.5: Variation of the recorded fluorescence intensity with film thickness and dye-concentration. The cone showed in Fig. 2.4 is placed inside the vertical pipe and the measurements are taken along a vertical line at the pipe center.

As the film thickness increases, Fig. 2.5 shows that the fluorescence intensity increases steeply initially, reaches a region of maximum, and then decreases, with relatively less-steepness. This is due to the spatial in-homogeneity in the laser beam, and is one of the reasons for the need of pixel-by-pixel calibration, i.e. a calibration curve of intensity versus film thickness for each pixel of the camera. The fluorescence intensity

for each film thickness increases with the dye concentration for A to G. However, upon further increasing the dye concentration to H, the measured fluorescence intensity distribution is lower than that of G. This suggests the existence of a maximum dye concentration beyond which there is an inverse relationship between fluorescence intensity and dye concentration. To visualize this better, the mean of the intensity values from 0.7 mm to 4.3 mm for each dye concentration shown in Fig. 2.5 is plotted in Fig. 2.6. The fluorescence intensity initially increases with increasing dye concentration up to 0.17 ml of dye/liter of liquid. Also in this range, the slope "$\dot{s}$" - increase in intensity for per unit increase in dye concentration, gradually decreases to zero at 0.17 ml of dye/liter of liquid. Upon further increasing the dye concentration, the fluorescence intensity decreases.

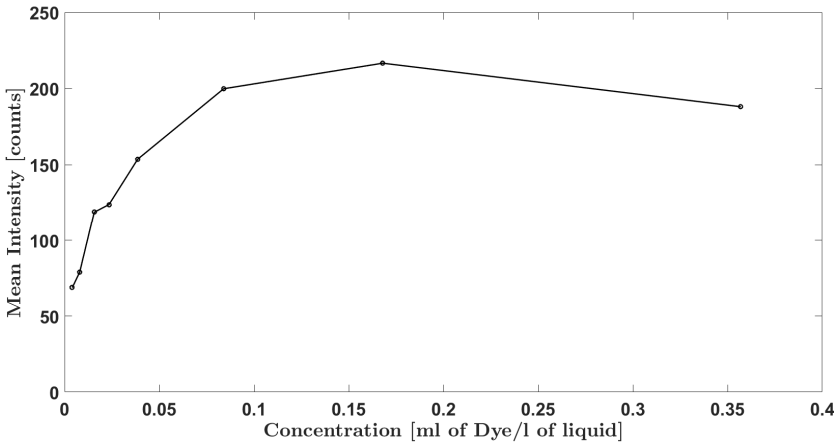

Figure 2.6: Variation of mean recorded fluorescence intensity (obtained by averaging fluorescence intensity distribution in Fig. 2.5) with dye concentration. The response is initially linear, followed by non-linear increase, then reaches saturation, and beyond which it decreases.

The selected dye concentration for the experiments should meet the following two criteria: (i) the variation of fluorescence intensity with increasing film thickness should be as high as possible; (ii) the film flow would be recorded at a temporal resolution of 250 Hz. So the fluorescence intensity should be high enough such that sufficient intensity can be captured in each frame. For criteria (i), it is desirable to choose the dye concentration such that *"s"* is as high as possible. This is because the behaviour of the fluorescence intensity with increasing film thickness is expected to be similar to the behaviour with increasing dye concentration (Fig. 2.5). A higher *"s"* will enable higher sensitivity to thickness variation. From Fig. 2.6 it is seen that for the *"s"* to be higher, the dye concentration has to be low. On the other hand, for criteria (ii), the dye concentration should be as high as possible, such that sufficient intensity is visible to camera during each frame. Trials were performed to satisfy these two criteria, and the dye concentration of 0.04 ml of dye / litre of liquid was found to be the optimum choice.

2.4. CALIBRATION

The laser beam is initially 3 mm in diameter. It is passed through a diverging lens to increase the diameter to 100 mm. The measurement area is 70 mm x 70 mm, and recorded with a spatial resolution of 0.1 mm/pixel. The basic idea of LIF is to make the fluorescence intensity emitted from a particular place in the measurement area (and thus to the corresponding pixel in the camera) to be proportional to the scalar variable of interest, which in this study is the film thickness. So a transfer function is to be obtained which maps the fluorescence intensity measured to the film thickness value. This is referred to as calibration. The following reasons explain why the transfer function is different for each pixel, necessitating a pixel-by-pixel calibration.

- The geometry of the tube is curved. So the laser rays would travel a longer distance than the film thickness everywhere except at the location where the incident laser ray is normal to the tangent of the tube surface. This is represented as seen from the top in Fig. 2.7a.

- The initial laser beam of 3 mm diameter has certain non-homogeneity in its spatial intensity distribution. This gets scaled up after passing through the diverging lens, resulting in an increased spatial

non-homogeneity of the laser beam. This can be seen from Fig. 2.7c, which shows the laser beam incident on a surface of size 200 mm by 200 mm.

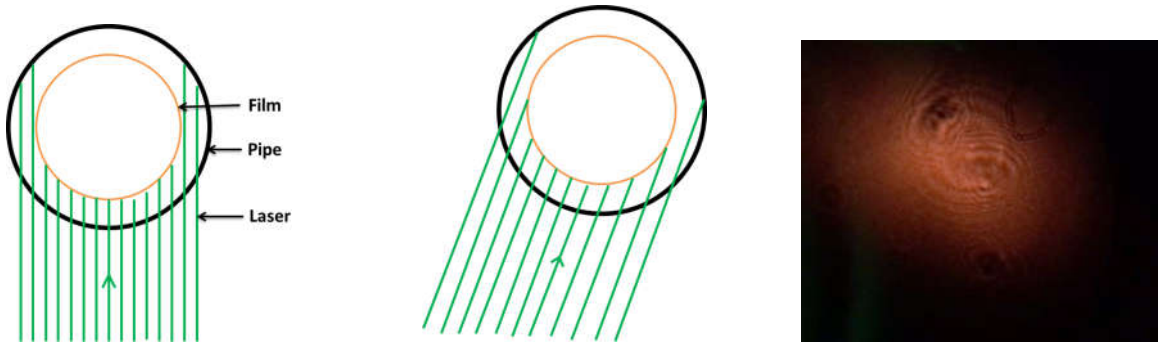

(a) (b) (c)

Figure 2.7: (a) Laser rays travel a longer distance compared to the film thickness (everywhere except at the pipe center) due to curvature of the geometry. (b) The inclination of the laser combined with its spatial non-homogeneity results in the non-uniform distribution of rays. (c) Spatial non-homogeneity of the laser beam, as seen by a camera with band filter on a projection area of 200 mm x 200 mm.

- One possible arrangement for the laser and the camera is to keep them at perpendicular direction as shown in Fig. 2.8a. In this arrangement, a dichroic mirror is used, whose function is to reflect the laser rays towards the pipe, while transmitting the emitted fluorescence rays towards the camera. The dichroic mirror is kept at an angle of 45^{o} to the vertical such that the laser rays is reflected towards the pipe. This implies that the size of the laser sheet that would be projected to the measurement area equals the projected size of the mirror to a plane that is normal to the incident laser ray. Thus the maximum size of the dichroic mirror available, which was 50 mm in diameter, limits the maximum size of laser sheet. So the projected laser sheet would approximately have an diameter of 25 mm. However, the waves formed on the film at the measurement location in the pipe have their stream-wise length higher than 25 mm, thus requiring the laser sheet falling on the pipe to be higher than 25 mm in diameter for better visualization. Since this is not possible to obtain with the available dichroic mirror, the laser is kept at an angle of 75^{o} to the horizontal as shown in Fig. 2.8b. Due to this arrangement, the incident beam intensity would be highest near the left and it keeps decreasing towards right, as shown in Fig. 2.7b.

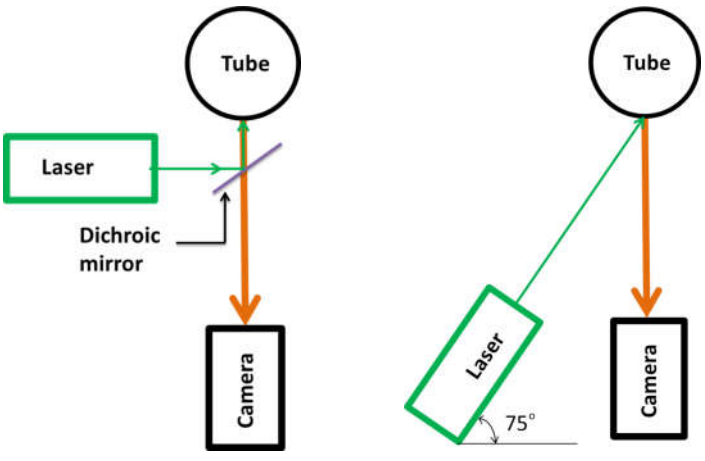

(a) (b)

Figure 2.8: (a) One possible arrangement for laser and camera. (b) Arrangement for laser and camera.

In addition to the above, the laser intensity was observed to have some temporal variation, even after switching on the laser for 1 hour. However, the temporal intensity variation was found to be within ≈ 4 intensity counts at most of the places. This can be inferred from the plot in Appendix D which shows the intensity variations as observed at 16 different spots in the measurement region. Each spot is taken to be an average of 3 by 3 pixels. Thus for the aforementioned factors, for the same film thickness throughout the measurement region, the intensity level measured by each pixel of the camera is different.

In order to perform the calibration, a set of different film thickness is to be obtained, such that each film thickness is constant throughout the measurement area. To simulate this, three stepped cylinders, with four steps in each are used. One of the cylinders is shown in Fig. 2.9. The steps have a height of 80 mm, which is chosen so that camera's field of view (70 mm x 70 mm) can be exposed to constant film thickness. The first cylinder has step diameters such that they create a radial film from 0.5 mm to 2 mm with 0.5 mm increment. The second cylinder creates radial film of thickness 3 mm to 6 mm with 1 mm as increment, while the third cylinder creates film of 8 mm to 14 mm with 2 mm as increment. The dimensions of these cylinders are provided in Table 2.1. Through this, the response of each pixel of the camera to different film thickness can be obtained. Using these data points, a second order polynomial is fitted through the standard least square routine. Thus a transfer function for measured fluorescence intensity to film thickness for each pixel is obtained.

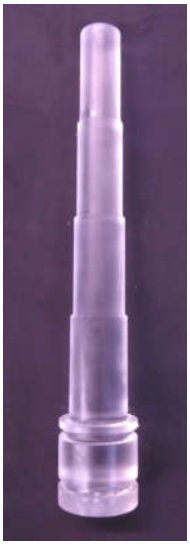

Figure 2.9: Cylinder used for calibration (entry 3 in Table 2.1). Step height is 80 mm, which creates a constant films thickness in the camera's field of view.

Table 2.1: Dimensions of the cylinders used for calibration. The tolerances in the diameter are within ± 0.15 mm.

		Step 1	**Step 2**	**Step 3**	**Step 4**
Cylinder 1	**Step Diameter [mm]**	61	60	59	58
	Radial Film Thickness [mm]	0.5	1	1.5	2
Cylinder 2	**Step Diameter [mm]**	56	54	52	50
	Radial Film Thickness [mm]	3	4	5	6
Cylinder 3	**Step Diameter [mm]**	46	42	38	34
	Radial Film Thickness [mm]	8	10	12	14

2.5. RECORDING AND PROCESSING OF THE EXPERIMENTAL DATA

The experiments are performed at different *Re* and the variation is achieved by changing the liquid mass flow rate through the vertical pipe. It is controlled by using a liquid bypass setup in the pump. At the start of the experiment, the laser and the pump are switched on for a period of 30 minutes to achieve steady state conditions. During this period, to avoid any photo decomposition of the dye due to continuous exposure to the laser light, an opaque sheet is kept in front of the measurement area. During each experimental trial, the fluorescence intensities are recorded at 250 Hz with an exposure time of 1/400 s, for 6000 frames (24 seconds). Each frame is 1024 x 1024 pixels. Using the transfer function obtained for each pixel from the calibration, the values of the fluorescence intensities are mapped to their respective film thickness values. During this conversion, if the intensity value at a particular pixel location lies more than 5 counts outside its calibrated range, then the corresponding thickness value is entered as NaN. To remove minor error signals, each frame of the film thickness values is normalized using the routine mentioned in Eq. 2.1.

$$h(i_{normalized}, j_{normalized}, t) = \frac{h(i,j,t)}{h(i_{time-averaged}, j_{time-averaged})} \cdot H \tag{2.1}$$

where,

- $h(i_{normalized}, j_{normalized}, t)$ represents the normalized film thickness value at each pixel location (i, j) at different time (t),

- $h(i, j, t)$ is the film thickness value at each pixel at different time as obtained using the transfer function,
- $h(i_{time-averaged}, j_{time-averaged})$ refers to the film thickness values at the location (i, j) obtained by averaging the 6000 frames, and
- H is the time and space averaged value of the film thickness across all recorded frames.

In Fig. 2.10 - (a) shows the snapshot of the intensity frame as recorded by the camera for $Re \approx 32$; (b) shows the film thickness frame that is retrieved from (a) using the transfer function obtained through calibration; (c) shows the average film thickness of 6000 frames recorded during an experimental trial of 24 seconds. The pixels in this frame are represented by $h(i_{time-averaged}, j_{time-averaged})$. The spatial average of the film thickness in (c) is represented by H, which has a value of 2.02 mm for the case of Re ≈ 32; (d) shows the normalized frame of (b) as indicated by Eq. 2.1. The process involved in the calibration, experiment, and in data processing are summarized in the form of a flow chart in Fig. 2.11.

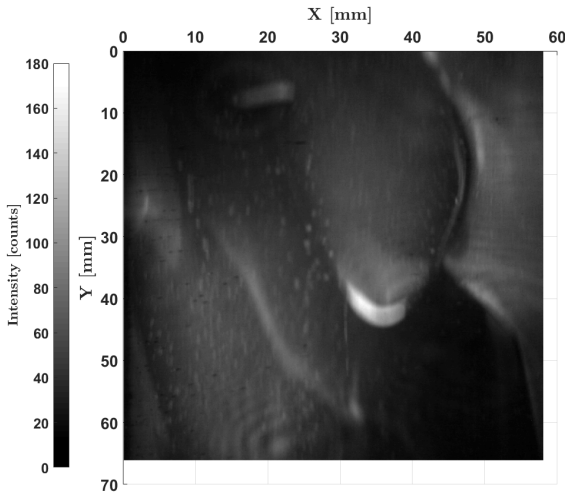

(a) Frame of fluorescence intensity as recorded by the camera during the film flow.

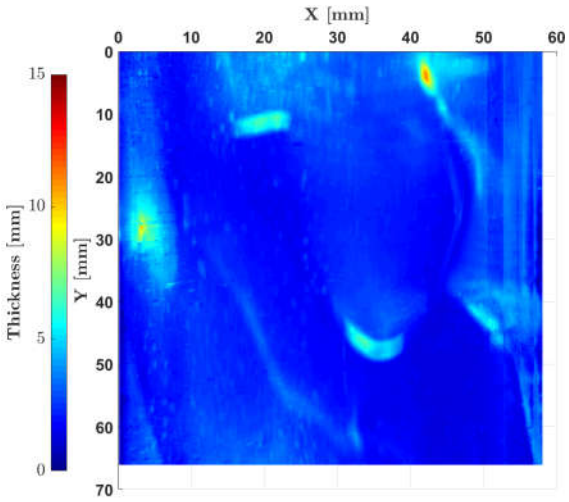

(b) Film thickness retrieved using transfer function obtained from calibration.

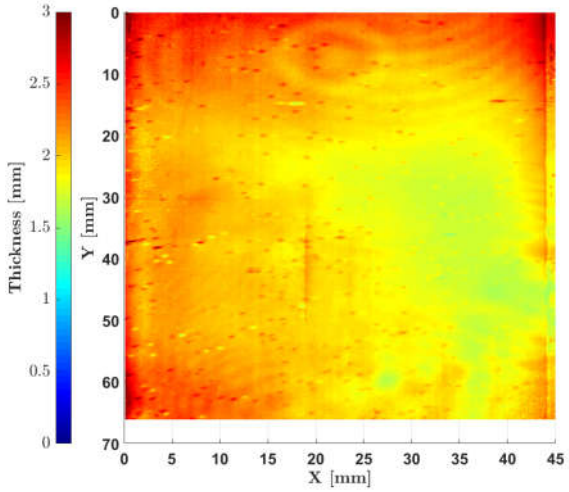

(c) Temporal average of the film thickness obtained from the measurement time of 24 seconds. The spatial average of this frame, (H), is 2.02 mm.

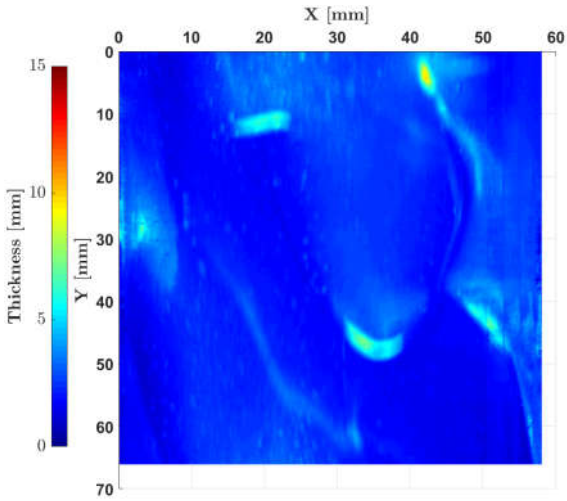

(d) Normalized image of (b). Normalization is performed by pixel-wise division of (b) by (c) and multiplying all the pixels of the resulting image by H (Eq. 2.1).

Figure 2.10: The snapshot of a recording by the camera, image of the retrieved film thickness and normalized image for the case of $Re \approx 32$.

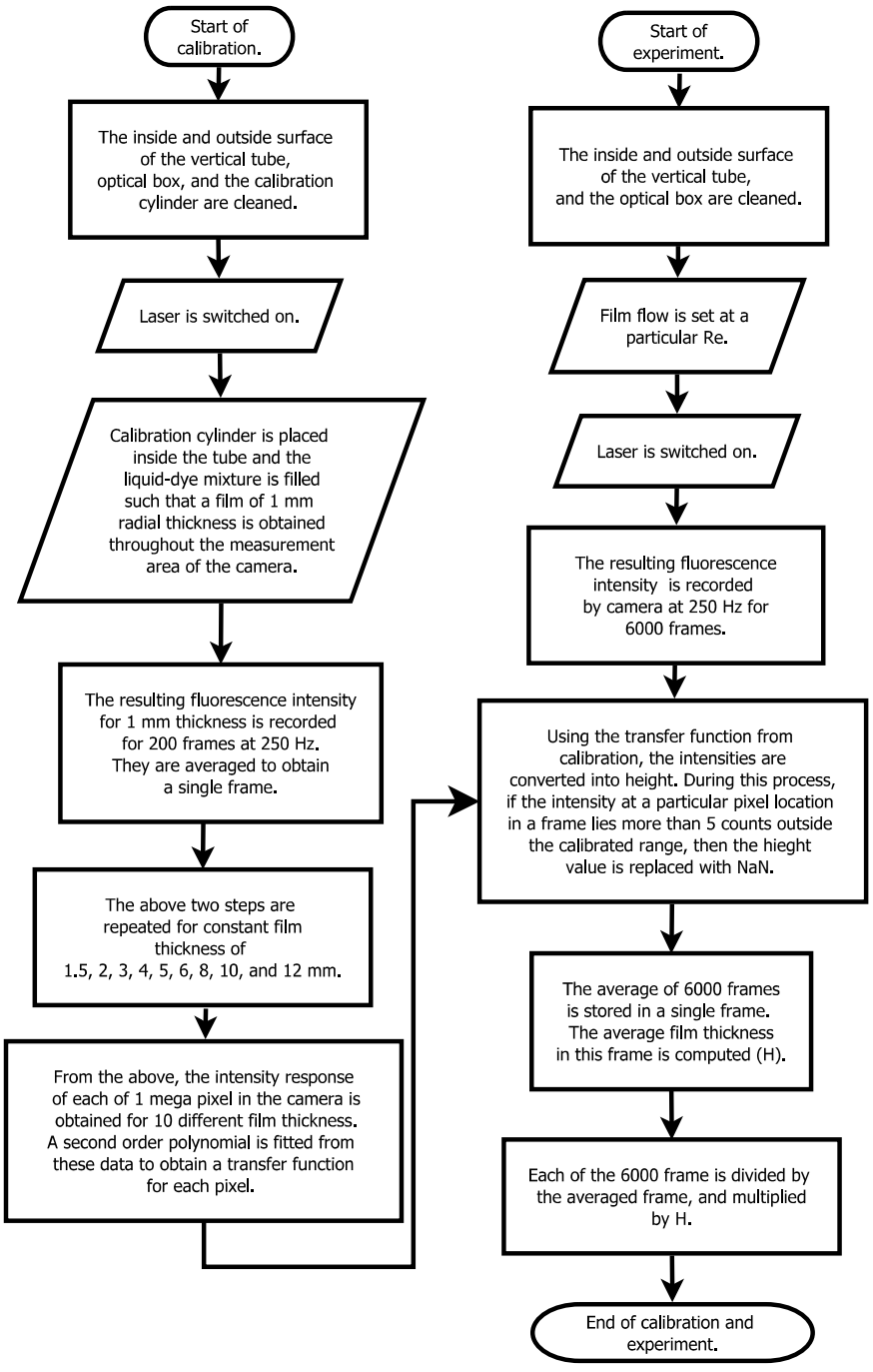

Figure 2.11: Flowchart of the steps involved in the calibration (left), and in experiment (right).

2.6. UNCERTAINTY ANALYSIS

In order to determine the uncertainty in the film thickness measurements, the intensities of the films created using the calibration cylinder were retrieved using the transfer function obtained for each pixel from calibration. The resulting deviations in the film thickness is given in Fig. 2.12. Except for 1 mm and 2 mm, more than 96 % of the measurements lie within ± 10 % of their actual values.

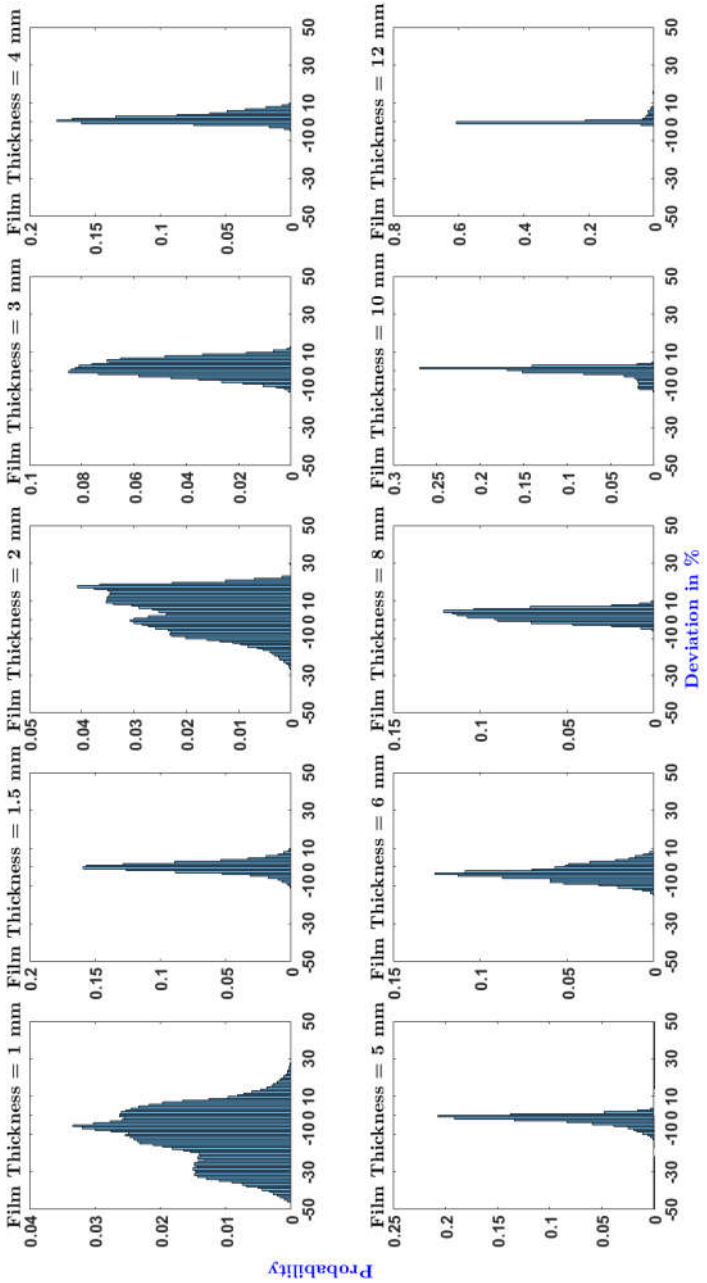

Figure 2.12: Probability density distributions of the deviation in film thickness measurements. The film thickness ranges from 1 mm to 12 mm. Except for 1 mm and 2 mm, more than 96 % of the measurement deviations lie within ± 10 % of their actual value.

Factors that contribute to the uncertainty are: (i) Presence of dark spots in the laser beam; (ii) Presence of air bubbles in the film flow. One possible reason for the formation of air bubble is due to cavitation arising from usage of gear pump; (iii) Usage of polynomial fit; (iv) Tolerances associated with manufacturing the calibration cylinder; and (v) Though small, the temporal fluctuations in the laser is a contributor.

3

Results and Discussions

This chapter presents the analysis of the film thickness measurements. Some two - dimensional wave shapes are initially given, followed by the three dimensional snapshots of waves. The experimentally obtained film thickness and wave velocities are compared with the Nusselt's theory. The formation of rivulets on the time averaged film thickness field are then described. The chapter ends with an analysis for the possible mechanisms leading to the rivulet formation using Probability Density Distributions (PDD) of the film thickness measurements.

3.1. EXPERIMENTAL CASES

The film flow analysis are performed for the Reynolds numbers 11.6 (±6%) and 32.4 (±8%). The variation in the *Re* is obtained by changing the liquid mass flow rate (Table 3.1). For simplicity, the Reynolds number of the two cases are hereafter referred to as 12 and 32. The volume flow rate is calculated by determining the time taken to fill a 1 litre cylinder. The uncertainty in the recording of time is 2 %, while it is 1 % for the volume. The liquid used to create the falling film is glycerine-water solution. To determine the composition, the dynamic viscosity of the solution is measured using Mettler-Toledo LS-40 rheometer, and the viscosity-mass fraction equation for glycerine-water mixture given by Cheng (2008)) is used to determine the mass fraction of the glycerine. The solution used is 84 ±1 wt. % glycerine, with $Ka = 8.05$ (±7%). Its surface tension (Jungermann and Sonntag (1991)) and density (Bosart and Snoddy (1928)) are given in Table 3.2. The recording of the LIF data is performed at 250 Hz.

Table 3.1: The liquid mass flow rate for the two cases of *Re* used in the analysis.

	***Re* = 11.6** (±6%)	***Re* = 32.4** (±8%)	**Unit**
Liquid mass flow rate	0.05 (±2%)	0.14 (±4%)	kg/s

Table 3.2: Physical properties of 84 ±1 wt. % glycerine-water mixture, (Cheng (2008), Jungermann and Sonntag (1991), and Bosart and Snoddy (1928)).

Parameter	**Value**	**Unit**
Density, ρ	1220 (±0.5%)	kg/m^3
Surface Tension, σ	0.065 (±3%)	N/m
Dynamic Viscosity, μ	0.09 (±2%)	kg/(m · s)
Kapitza Number, *Ka*	8.05 (±7%)	dimensionless

3.1.1. LOCATION OF MEASUREMENT POINTS/LINE

In the following sections, film thickness measurements taken at certain locations in the measurement field are utilized. Fig. 3.1 is used to indicate these locations.

3.2. WAVE SHAPE - TWO-DIMENSIONAL

Some typical two-dimensional wave shapes observed for $Re = 32$ is given in Fig. 3.2. The measured film thickness is plotted along the horizontal axis while the measurement location along the stream-wise direction is plotted in the vertical axis. The film thickness measurements are taken along a 1 mm wide line whose location is at X = 30 mm in Fig. 3.1. For $Re = 32$, the mean film thickness obtained by spatial and temporal averaging of the film thickness measurement field for 24 seconds is 2.02 mm. The film thickness for a film flow without waves, i.e. Nusselt film thickness, determined by Eq. 1.5, is 2.38 mm. These are also plotted in Fig. 3.2. The reason for the difference is explained in section 3.4.

For the film profile in left of Fig. 3.2, two waves with maximum crest height of 5 mm and 9.5 mm are observed. For the wave at the top, the increase in the film thickness per unit distance along the stream-wise direction, i.e. the wave slope, is 0.2 mm/mm at the wave-back, while it is 0.9 mm/mm at the wave-front, i.e. the wave slope in the wave-font is ≈ 5 times that of the wave-back. The higher slope at the wave-front is expected to be due to the action of gravity that tends to accumulate the liquid at the wave-front. Similar wave trends were observed for high *Ka* fluids by Kharlamov et al. (2015) for $Re \sim \mathcal{O}(10)$ (Fig. 1.12) and by Karapantsios and

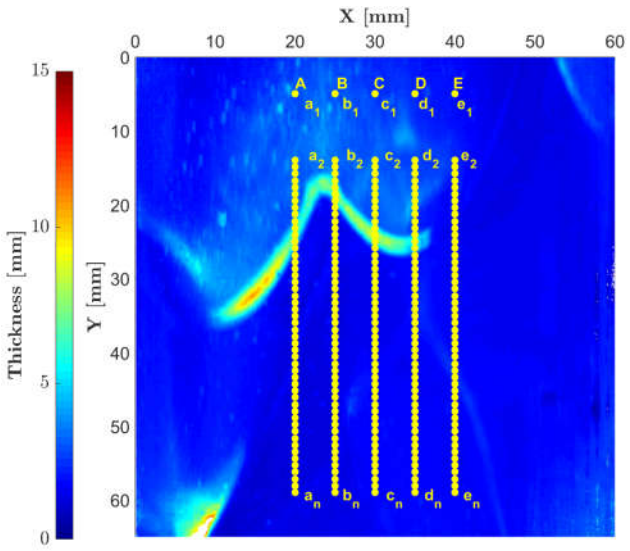

Figure 3.1: Location of the film thickness measurement points (yellow dots) used for analysis in subsequent sections of the report.

Karabelas (1990) for *Re* in the range of 500 to 13000 and *Ka* (section 1.4.5). This similarity in the wave slope trend indicates the importance of the force due to gravity at both high and low *Re* and *Ka* film flows.

For the film profile in the middle of Fig. 3.2, from the point of the maximum crest height, the film thickness reduces gradually in the region of its wave-back. This indicates the wavelength between successive waves is higher when compared with the plot to the left. In certain instances, waves were not observed along the measurement line due to passage of waves at other parts of the pipe. One such profile is shown in the right of Fig. 3.2.

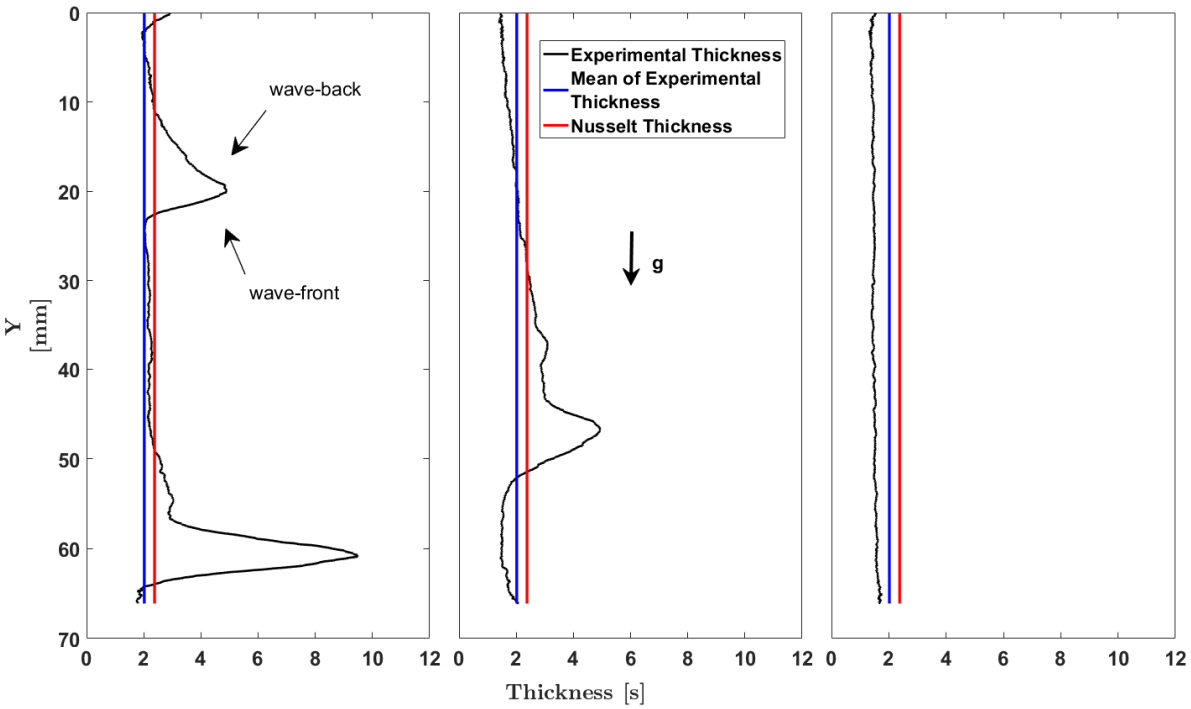

Figure 3.2: Some typical two dimensional wave shapes observed for *Re* = 32. Measurement line is 1 mm in width, and it is located at X = 30 mm in Fig. 3.1.

Three consecutive snapshots are shown in Fig. 3.3. In the left plot, wave 'A' and 'B' have a maximum

amplitude of 8.8 mm and 5.3 mm respectively. A wave with a larger amplitude travels faster than a wave with a smaller amplitude. This is because, the intensity of the viscous shear stress imposed by the stationary wall, which acts in the direction against the film flow, reduces as the distance from the wall increases. This is also reflected in the Nusselt's equation for film velocity - Eq. 1.3, in which the velocity is proportional to the square of the film thickness. Due to this, 'A' travels faster at 1.8 m/s, while 'B' travels at 1.0 m/s. This leads to merging of the waves along the stream-wise direction, as seen in the middle and the right of Fig. 3.3.

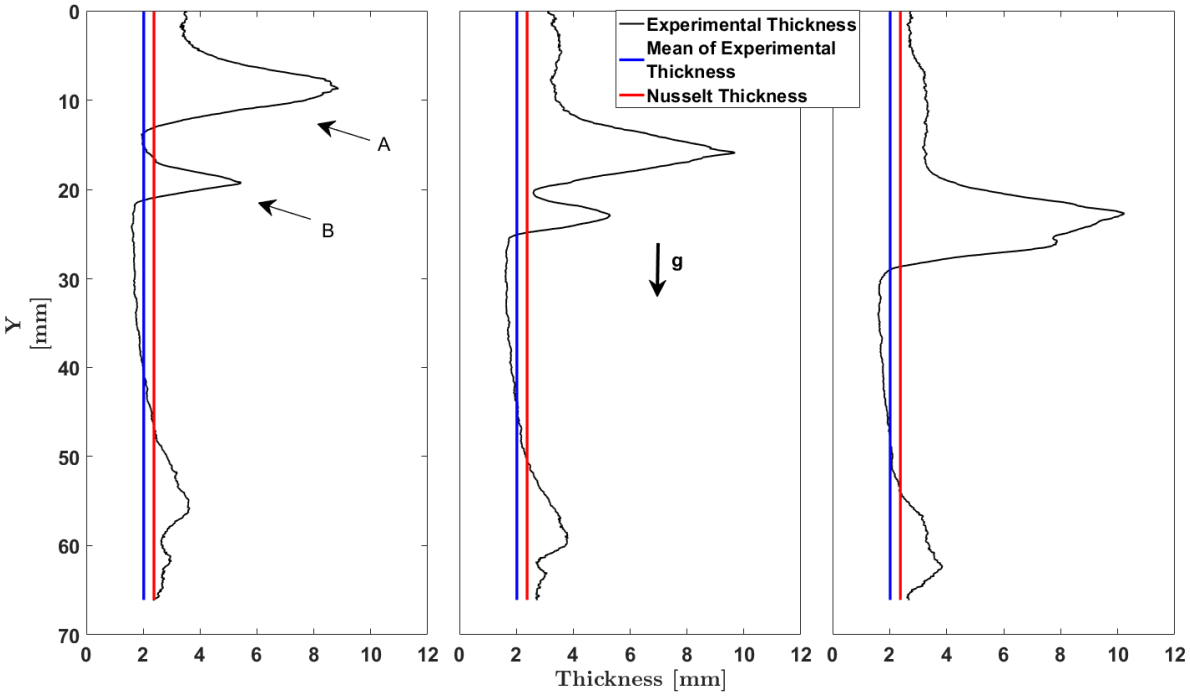

Figure 3.3: Merging of the waves in the stream-wise direction observed for $Re = 32$. Interval between the frames is 4 ms. Measurement line is 1 mm in width and it is located at X = 30 mm in Fig. 3.1.

3.3. THREE-DIMENSIONAL WAVE SHAPE VISUALIZATION

The three-dimensional visualization of the film flow for $Re = 12$ is shown in Fig. 3.4 for a time interval of 60 ms. In Fig. 3.4a, two waves are identified as 'A' and 'B', with 'B' having a higher amplitude than 'A'. The wave velocity of a wave is proportional to its amplitude (section 3.2). Due to this, 'B' travels faster than 'A'. In Fig. 3.4e, 'A' and 'B' are in the same position along the transverse direction. The lateral wave surface that lies between 'A' and 'B' are in contact with each other. This results in merging of the waves in the transverse direction which is seen in Fig. 3.4f. During this process, the amplitude of the wave peaks gets redistributed, which is seen in Fig. 3.4d - Fig. 3.4f. This suggests the occurrence of transverse redistribution of the liquid during the merging process. A similar image, for $Re = 32$ is shown in Fig. 3.5 for a time interval of 40 ms. In Fig. 3.5a, 'A' is behind 'B'. Owing to the larger amplitude of 'A', it travels faster than 'B' as seen in the subsequent frames - Fig. 3.5b to Fig. 3.5f. As a result, they are nearly at the same stream-wise position in Fig. 3.5f. However in this case, merging of the waves does not happen since their lateral surfaces are not in contact.

Regarding the shape of the three-dimensional waves, Fig. 3.6 shows the complimentary view of Fig. 3.5e. The color scale range is reduced to 0 to 10 mm to better distinguish the shape. It is inferred that the film thickness in the upstream region on the wave crest is higher than the undisturbed film thickness. This characteristic is similar to the streak-like shape (section 1.5.2) obtained by Kharlamov et al. (2015) which was shown in Fig. 1.12.

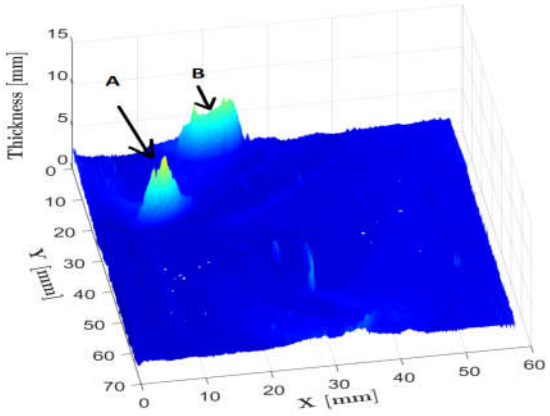

(a) Time = 0 ms

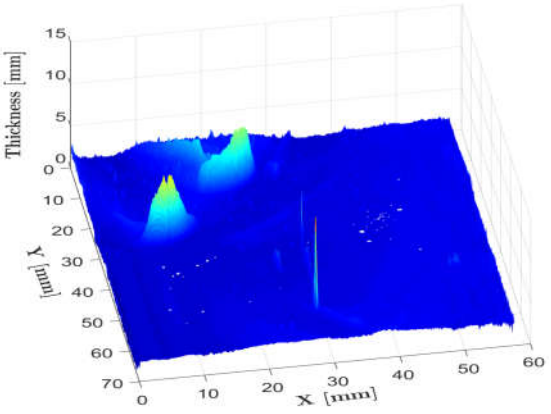

(b) Time = 12 ms

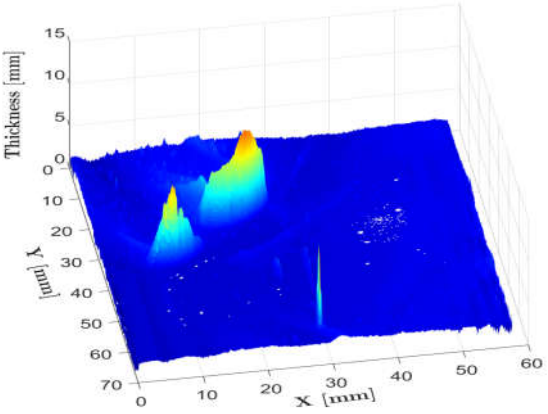

(c) Time = 24 ms

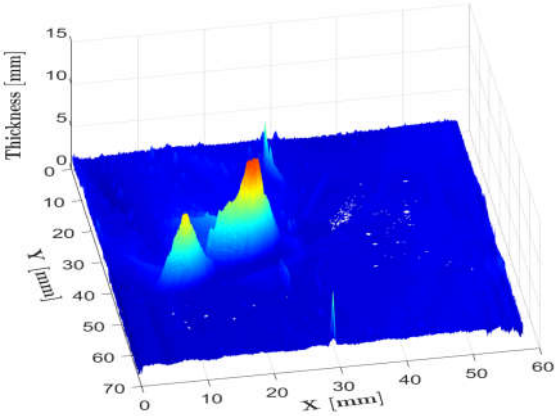

(d) Time = 36 ms

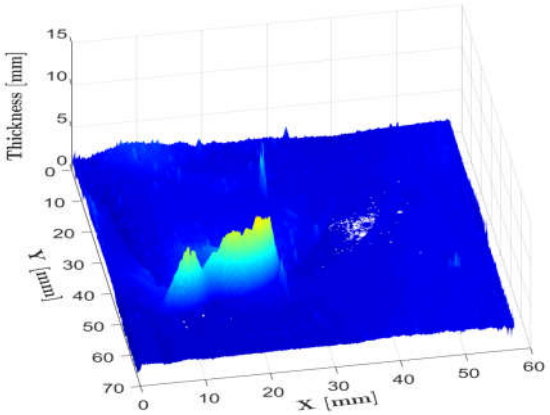

(e) Time = 48 ms

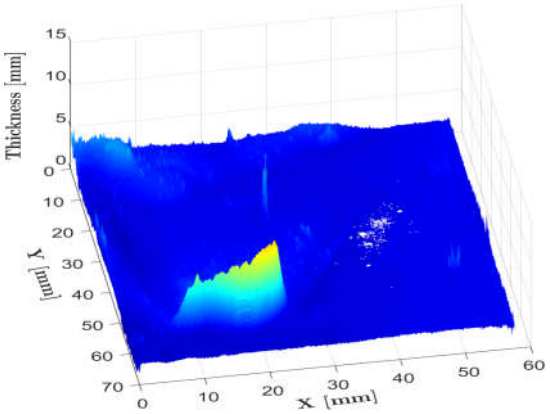

(f) Time = 60 ms

Figure 3.4: Three-dimensional visualization of the film flow for $Re = 12$ during a time interval of 60 ms, represented in 6 frames. The frames show, among others, the travel of two waves that are identified as 'A' and 'B' in (a). In (a), 'B' is behind 'A'. In the subsequent frames, it is seen that 'B' owing to its higher amplitude, travels faster, merges with 'A' along the transverse direction.

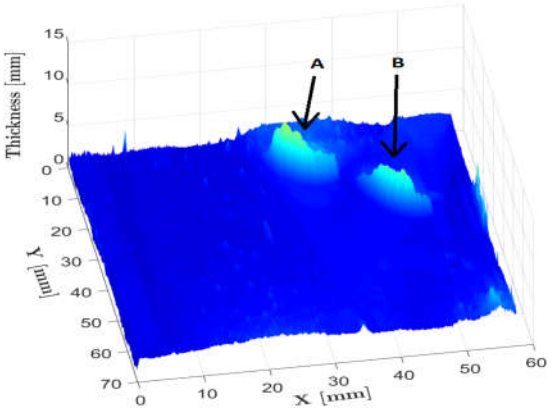

(a) Time = 0 ms

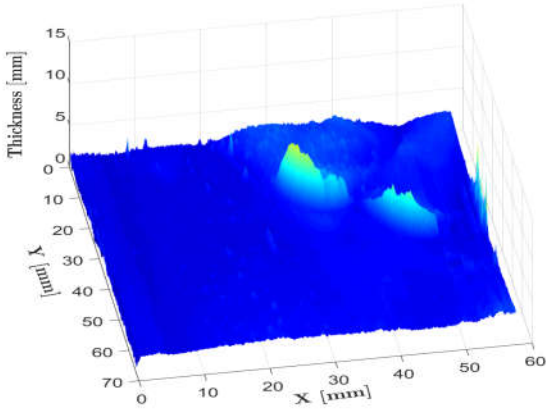

(b) Time = 8 ms

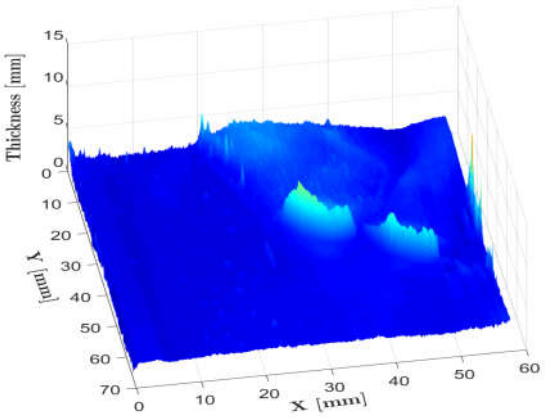

(c) Time = 16 ms

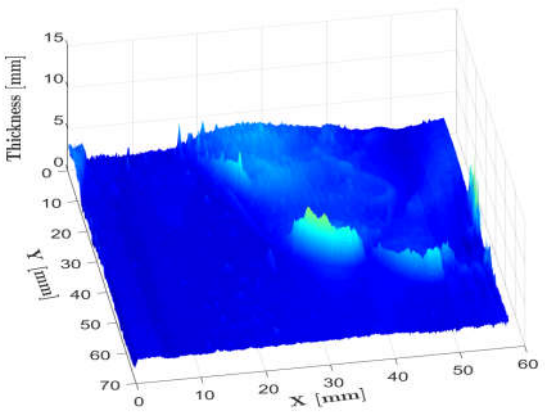

(d) Time = 24 ms

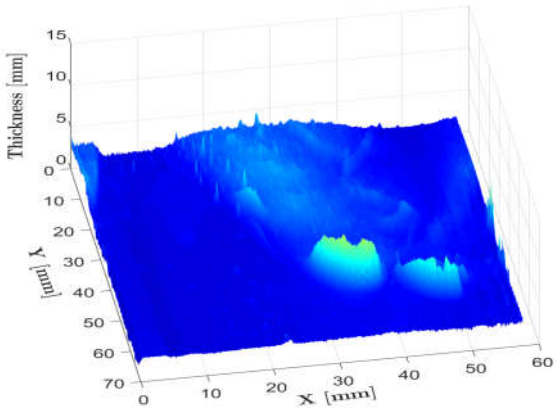

(e) Time = 32 ms

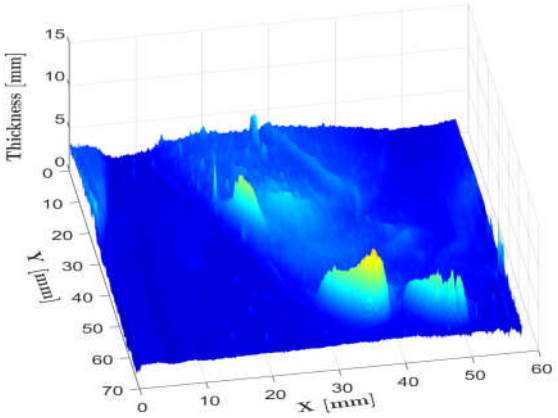

(f) Time = 40 ms

Figure 3.5: Three-dimensional visualization of the film flow for $Re = 32$ during a time interval of 40 ms, represented in 6 frames. The frames show, among others, the travel of two waves that are identified as 'A' and 'B' in (a). In (a), 'A' is behind 'B'. From the subsequent frames it is seen that 'A' has higher velocity than 'B' due to higher amplitude of the former.

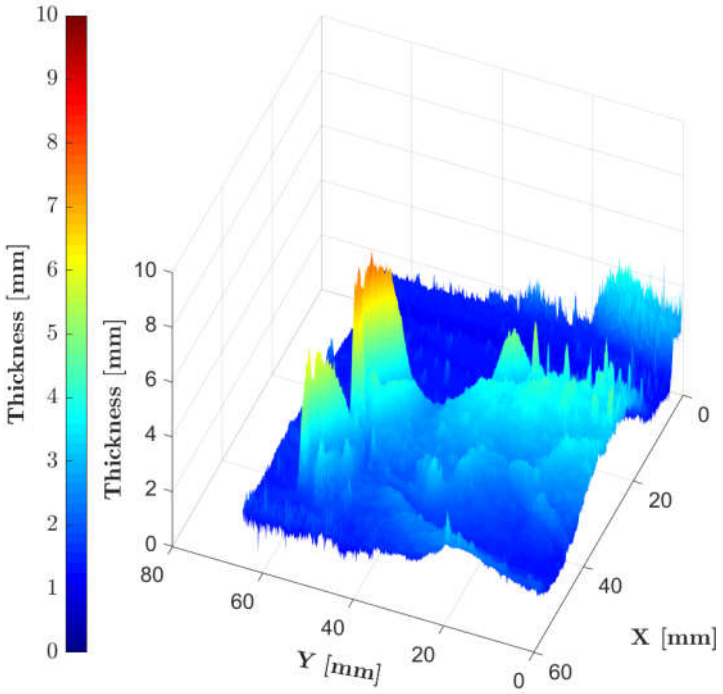

Figure 3.6: Complimentary view of the film flow instance shown in Fig. 3.5e. The thickness of the film at the upstream position of the wave crests is higher than the undisturbed region. This characteristic is similar to the streak-like profile shown in Fig. 1.12.

3.4. FILM THICKNESS

The instantaneous film thickness for the case of $Re = 32$ at the location d_2 in Fig. 3.1 is given in Fig. 3.7. The Nusselt's film thickness and the experimental mean film thickness for $Re = 12$ and 32 are presented in Table 3.3. The experimental value of the mean film thickness is ≈ 15 % lower than the analytical solution for both the cases.

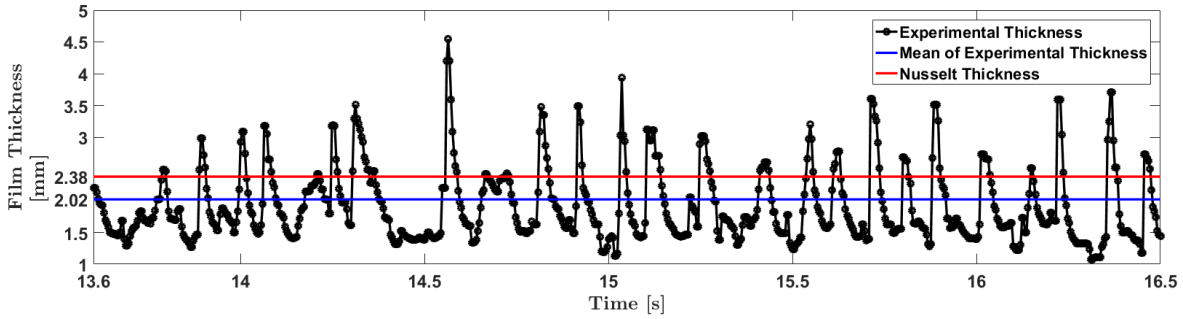

Figure 3.7: Time series of the film thickness for $Re = 32$ at the location d_2 in Fig. 3.1. A third order one-dimensional median filter is applied to remove non-physical spikes in the measurements. The size of the measurement spot is 1 mm x 1 mm. The mean of the experimental film thickness, obtained by spatial and temporal averaging of 6000 frames is 2.02 mm. It is lower than the Nusselt's film thickness, which is 2.38 mm.

The experimental mean value can be understood to be lower than the analytical value due to the following: The film thickness has a cubic root dependency on the liquid mass flow rate (Eq. 1.5). In experiments, for a particular *Re*, even though the overall mass flow rate of the system is kept constant, due to wave formation the local mass flow rates varies depending on the wave amplitude. Due to the cubic root dependency, the increase (or decrease) in the film thickness when the local mass flow rate increases (or decreases), is less than the value that would have been, if the relationship has been linear. So the spatial and temporal average of the experimental film thickness would be lower with respect to the analytical solution. It could be better understood by

Table 3.3: Analytical and experimental values of the film thickness for $Ka = 8$

Case	Analytical film thickness [mm]	Experimental mean film thickness [mm]	Deviation
$Re = 12$	1.69	1.44	- 15.0 %
$Re = 32$	2.38	2.02	- 15.1 %

considering the two cases - (i) Nusselt film flow (without waves), and (ii) actual film flow with waves. Nusselt's velocity profile (given by Eq. A.5) is assumed to be valid in both the cases. The overall liquid mass flow rate ($\dot{m}$), total time (t) and frequency (f) of the film thickness measurements are same for both the cases. The time instance of the film thickness measurements are identified by t_i, for i=1 to $n = (t \cdot f)$. A common point in the flow field is chosen for analysis. The objective is to determine the average film thickness for these two cases for the time period t_i, i=1 to n.

For the case (i), the local mass flow rate for each of the time instance is given by $[c_{\text{th-i}} \cdot \dot{m}]$, $i = 1$ to n, where $c_{\text{th-i}}$ denotes the factor by which the liquid mass flow rate at an instance "i" varies when compared with the overall liquid mass flow rate ($\dot{m}$). Due to absence of the waves, the local liquid mass flow rates are the same as the overall liquid mass flow rate ($\dot{m}$) at all time instances t_i, $i = 1$ to n. Therefore, $c_{\text{th-i}}$ has a value of 1 for all i=1 to n.

For the case (ii), due to the waves, the local liquid mass flow rates would vary with time and it is denoted by $[c_{\text{ex-i}} \cdot \dot{m}]$. When the wave amplitude is less than the laminar film thickness, $c_{\text{ex-i}}$ is less than 1, and vice versa. By the principle of mass conservation, the arithmetic mean of $c_{\text{ex-i}}$, for $i = 1$ to n, is 1. As the overall liquid mass flow rate ($\dot{m}$) is same for the cases (i) and (ii), the summation of their instantaneous liquid mass flow rates for the time period n should also be the same. This is indicated by Eq. 3.1.

$$\frac{1}{n} \cdot \sum_{i=1}^{n} c_{\text{th-i}} \cdot \dot{m} = \frac{1}{n} \cdot \sum_{i=1}^{n} c_{\text{ex-i}} \cdot \dot{m} \quad [kg/s] \tag{3.1}$$

Since Nusselt's velocity profile is assumed to be valid for both the cases, the film thickness is given by Eq. 1.5, which is re-written in Eq. 3.2.

$$\delta = \alpha \cdot \dot{m}^{1/3} \quad [m], \text{ where } \alpha = \left(\frac{3 \cdot \nu}{\rho \cdot g}\right)^{1/3} \tag{3.2}$$

The average film thickness for the analytical flow (case i) is given by Eq. 3.3.

$$\delta_{th-avg} = \frac{1}{n} \cdot \sum_{i=1}^{n} \alpha \cdot (c_{\text{th-i}} \cdot \dot{m})^{1/3} = \alpha \cdot \dot{m}^{1/3} \cdot p_{th} \quad [m], \text{ where } p_{th} = \frac{1}{n} \cdot \sum_{i=1}^{n} {c_{\text{th-i}}}^{1/3} \tag{3.3}$$

The average film thickness for the experimental flow (case ii) is given by Eq. 3.4.

$$\delta_{ex-avg} = \frac{1}{n} \cdot \sum_{i=1}^{n} \alpha \cdot (c_{\text{ex-i}} \cdot \dot{m})^{1/3} = \alpha \cdot \dot{m}^{1/3} \cdot p_{ex} \quad [m], \text{ where } p_{ex} = \frac{1}{n} \cdot \sum_{i=1}^{n} {c_{\text{ex-i}}}^{1/3} \tag{3.4}$$

Since $c_{\text{th-i}}$ has a value of 1 for i = 1 to n, p_{th} is 1. However $c_{\text{ex-i}}$ can take values below and above 1, with an arithmetic mean of 1. So p_{ex} would always be less than 1. Thus, δ_{ex-avg} is always less than δ_{th-avg}.

3.5. TIME-AVERAGED FILM THICKNESS

The film thickness obtained in the measurement field, is time averaged for a period of 2 seconds and is shown in Fig. 3.8 for $Re = 12$, and in Fig. 3.10 for $Re = 32$ at different instances. It could be inferred that the variation in the film thickness in the stream-wise direction is relatively constant, while the transverse variation is considerable. The ridges are indicated by the blue arrow lines, while the orange arrow lines indicate the valleys in Fig. 3.8 and Fig. 3.10. The following parameters are found to vary in the time averaged film thickness field depending on the instances of averaged time - (i) the pattern of the film thickness variation in the transverse direction, (ii) number and (iii) transverse length of ridges and valleys.

3.5.1. FILM THICKNESS IN THE TRANSVERSE DIRECTION

The film thickness variation in the transverse direction for Re = 12 at five horizontal lines in Fig. 3.8 a -d, are shown in Fig. 3.9 a - d respectively. The pattern of transverse thickness variation changes with time, and the same is shown for Row 3 in Fig.3.9 e and f. Similar plots for Re = 32 are shown in Fig. 3.11 a - f. Table 3.4 presents a quantitative overview of the film thickness variation presented in Fig. 3.9 and Fig. 3.11. The spatial average of the film thickness in Fig. 3.8 and Fig. 3.10 is presented under the column $h_{s.t.avg}$. The minimum and the maximum film thickness based on 10 % and 90 % of the probability density distribution are presented under h_{min} and h_{max}.

Table 3.4: Variation of the film thickness measurements in ridges and valleys shown in Fig. 3.9 and Fig. 3.11. h_{min} and h_{max} represents the minimum and the maximum film thickness determined from 10 % and 90 % of the probability density distribution. Number of ridges (N_R) and valleys (N_V) and their widths observed in Fig. 3.8 and Fig. 3.10. The entries in bold represents the ridge/valley that is fully-visible.

Re	**Instance of averaged time**	**Spatial and temporal averaged film thickness $h_{s.t.avg}$**	h_{min}	h_{max}	**Variation of h_{min} and h_{max} from $h_{s.t.avg}$**		N_R	**Ridge width**	N_V	**Valley width**
	s	**mm**	**mm**	**mm**	**%**			**mm**		**mm**
12	10 to 12	1.45	1.43	1.48	-1.4	2.1	1	**22**	2	**4**; 12
	12 to 14	1.43	1.40	1.48	-2.1	3.1	1	12	2	**17**; 10
	16 to 18	1.45	1.40	1.49	-3.4	2.8	2	6; 24	1	**8**
	18 to 20	1.44	1.40	1.48	-2.8	2.8	2	**20**; 10	1	10
32	10 to 12	1.98	1.90	2.08	-4.3	4.8	1	**18**	2	7; 14
	12 to 14	1.98	1.89	2.06	-4.8	3.8	2	5; 15	1	**20**
	16 to 18	2.04	1.96	2.13	-3.9	4.4	2	11; 13	1	**18**
	18 to 20	2.01	1.97	2.07	-2.2	2.7	2	15; **11**	2	8; **5**

The variation in h_{min} and h_{max} from $h_{s.t.avg}$ is found to be dependant on the instances of averaged time for both the cases of *Re*. For the case of Re = 12, the variation in Fig. 3.9 a,b, is lower when compared with Fig. 3.9 c,d, which are quantified in Table 3.4. On average, the film thickness variation is within ± 3 % of $h_{s.t.avg}$. For the case of Re = 32, the variation in Fig. 3.11 a,b is higher when compared with Fig. 3.11 c,d. The average film thickness variation is higher in this case, which is within ± 5 % of $h_{s.t.avg}$. For both the cases of *Re*, the transverse variation in thickness varies in a cyclic manner, indicating the presence of rivulets. Kharlamov et al. (2015) explicitly observed such rivulets (Fig. 1.14) for the first time on the time-averaged film thickness fields for Re = 56 and Ka = 3660, which was discussed in section 1.5.2.

The trend of the transverse thickness variation, as can be seen from Fig. 3.8 - Fig. 3.11 is similar along the stream wise direction. The position of the ridges and valleys varies with time. This indicates that they are unsteady and one-dimensional in their behaviour.

A stepped pattern is visible in time averaged film thickness for both the cases of *Re*. It could be formed due to the passage of the high amplitude waves. One example is circled in Fig. 3.8 a. The distance between the pattern is 3.1 mm, while the time difference between the frames is 4 ms. This results in a velocity of 0.78 m/s. This is in close agreement with the velocity values obtained in the section 3.7 for Re = 12, which is 0.75 m/s.

NUMBER AND WAVELENGTH OF RIDGES AND VALLEYS

The ridges and valleys are indicated in Fig. 3.8 and Fig. 3.10. Their number and transverse width are also quantified in Table 3.4. In order to determine the region of the ridges and valleys, $h_{s.t.avg}$ in Table 3.4 is used as the cut-off value, i.e. regions with thickness below $h_{s.t.avg}$ are identified as valley, and above as ridge. It is to be noted that the measurement field is only a part of the tube geometry. So for the ridges and valleys that lie at the right and the left extremes in Fig. 3.8 and Fig. 3.10, only part of their actual width is visible. To indicate this, one-sided arrow line is used, while the double-sided arrow line is used when a ridge/valley is fully visible. The width of the ridge/valley that is fully visible is represented in bold in Table 3.4. For both the cases of *Re*

considered, the combined number of ridges and valleys varies between 3 and 4, and relatively short (5 to 10 mm) as well as long (10 to 20 mm) width of the ridges and valleys are observed.

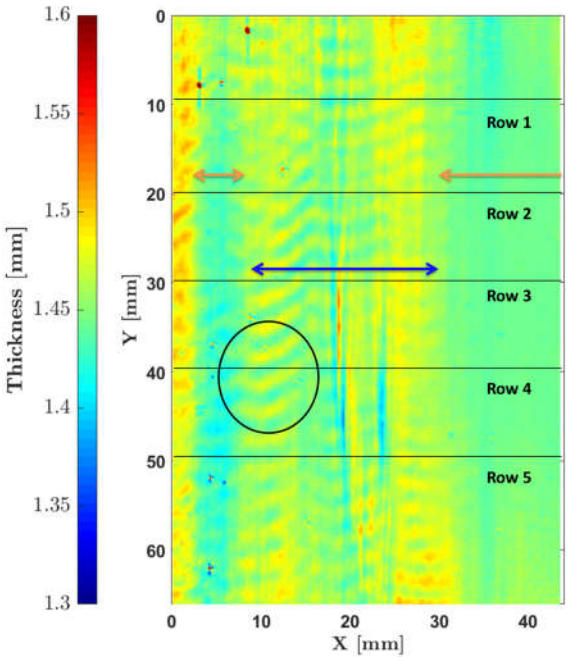

(a) Averaged Time = 10 to 12 s

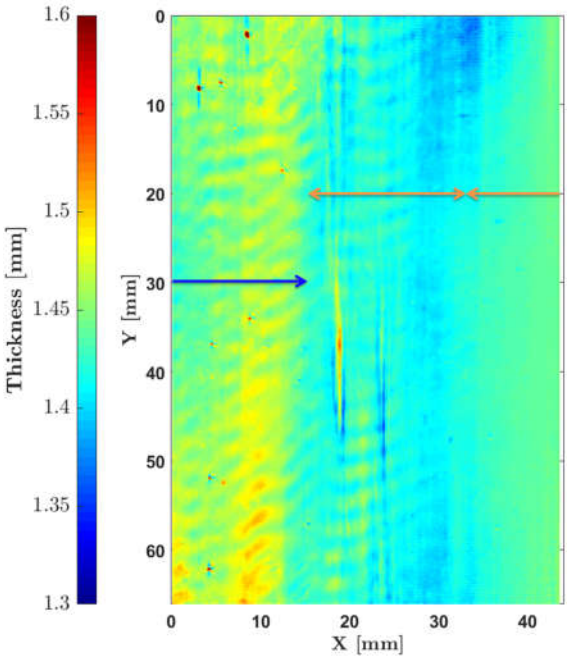

(b) Averaged Time = 12 to 14 s

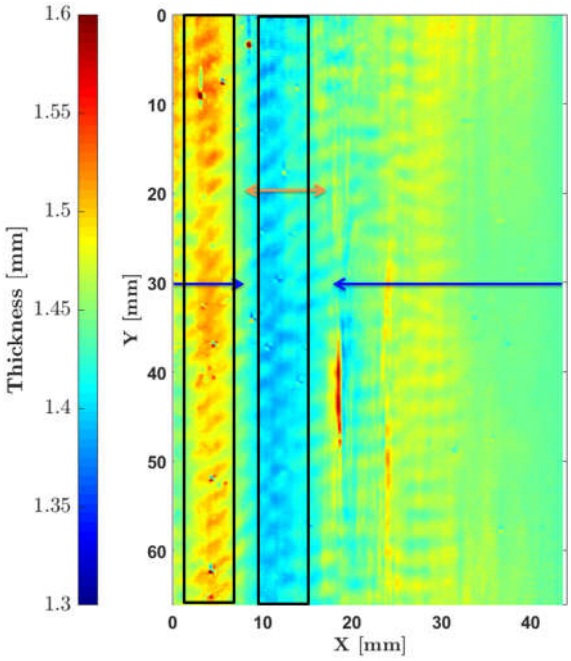

(c) Averaged Time = 16 to 18 s

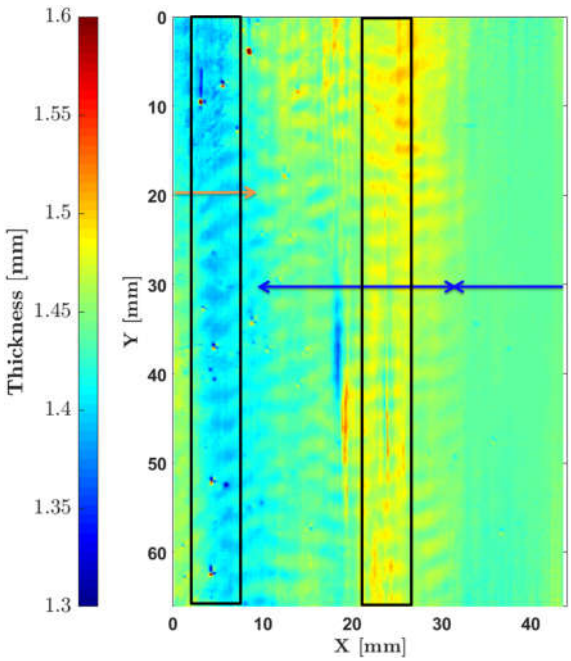

(d) Averaged Time = 18 to 20 s

Figure 3.8: Contour plot of the film thickness averaged for 2 seconds at different time instances for $Re = 12$. The blue arrows indicate the region of ridges, while the orange indicates the valley. Single-headed arrow lines are used when a ridge/valley is not fully visible, while a double-headed arrow line is used otherwise.

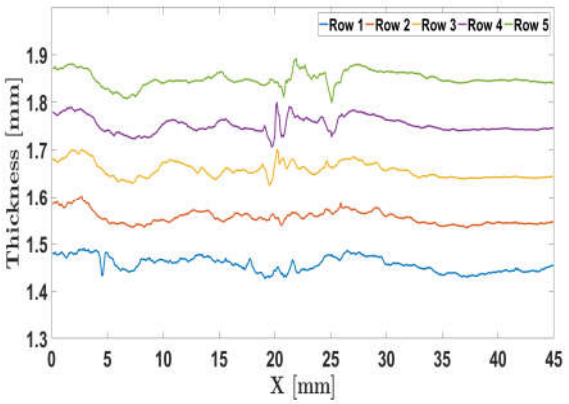

(a) Averaged Time = 10 to 12 seconds

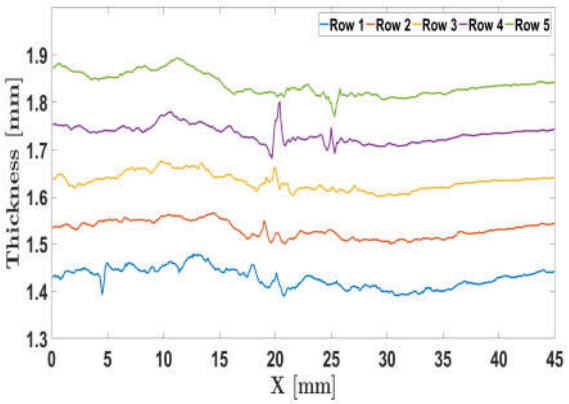

(b) Averaged Time = 12 to 14 seconds

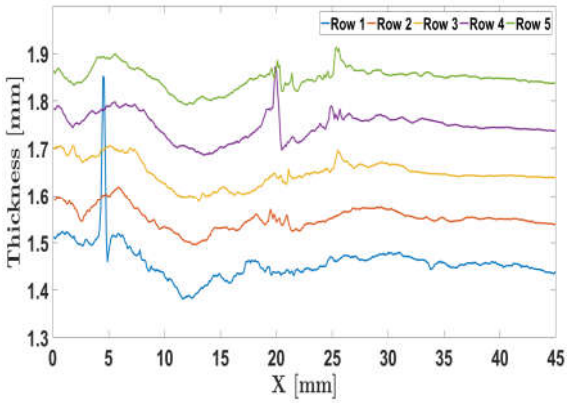

(c) Averaged Time = 16 to 18 seconds

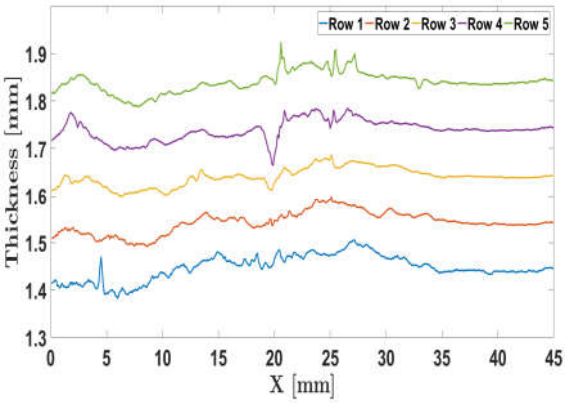

(d) Averaged Time = 18 to 20 seconds

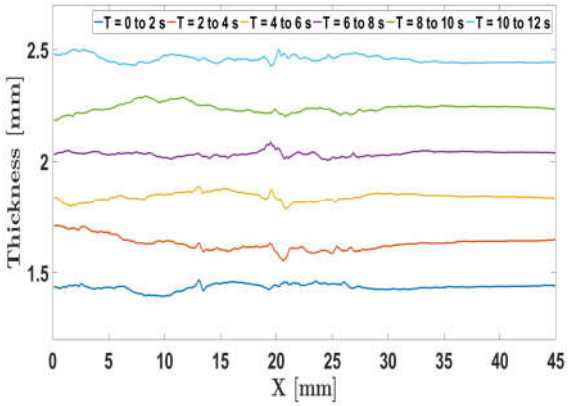

(e) Film thickness variation along Row 3 for 0 to 12 s.

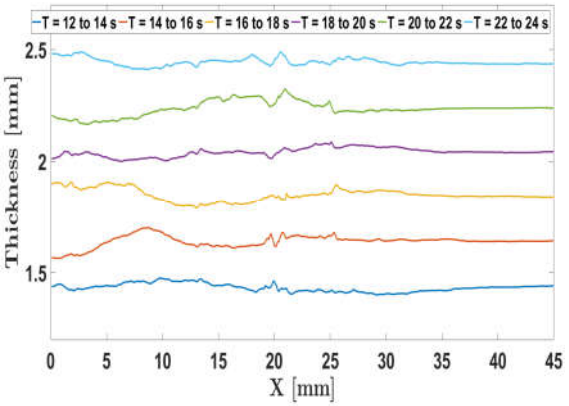

(f) Film thickness variation along Row 3 for 12 to 24 s.

Figure 3.9: (a): Plot of the film thickness in the transverse direction for Re = 12 averaged for 2 seconds. The thickness variation is shown at 5 horizontal lines shown in Fig. 3.8a. The plot for each line (except Row 1) is successively shifted by 0.1 mm to avoid data cluttering. The same is shown in (b) - (d) at different time instances. (e): Temporal variation of the film thickness along Row 3 for 0 to 12 seconds and (f) for 12 to 24 seconds. Each time instance (except T = 0 to 2 s in (e) and T = 12 to 14 s in (f)) is successively shifted by 0.2 mm.

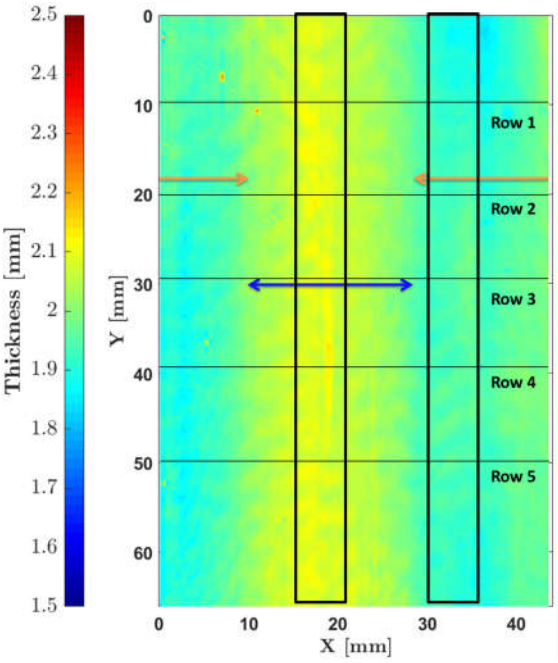

(a) Averaged Time = 10 to 12 s

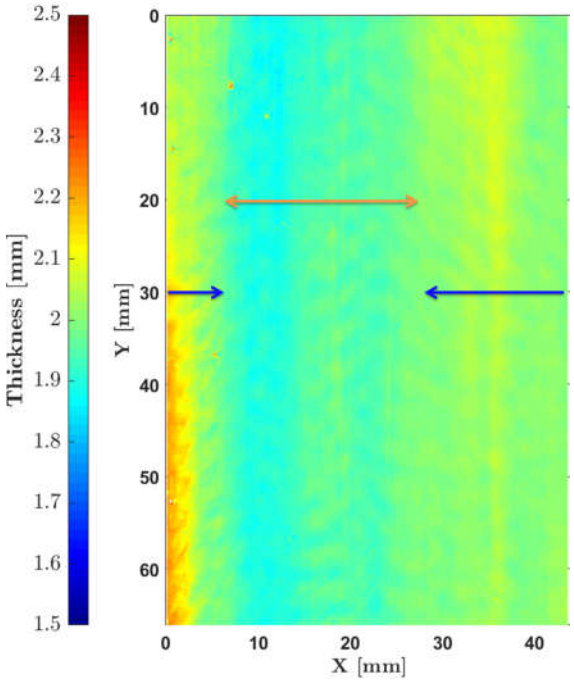

(b) Averaged Time = 12 to 14 s

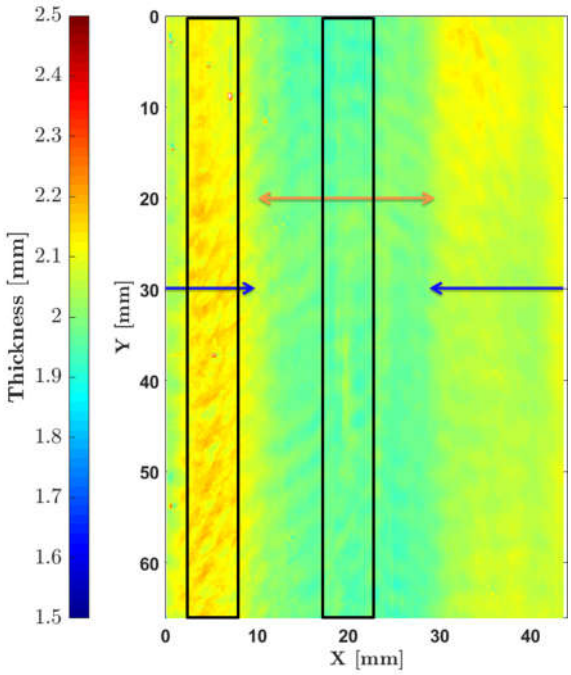

(c) Averaged Time = 16 to 18 s

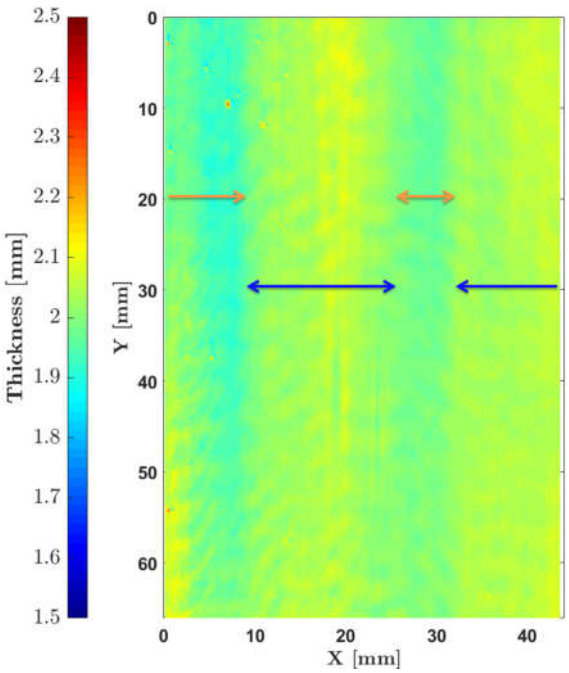

(d) Averaged Time = 18 to 20 s

Figure 3.10: Contour plot of the film thickness averaged for 2 seconds at different time instances for $Re = 32$. The blue arrows indicate the region of ridges, while the orange indicates the valley. Single-headed arrow lines are used when a ridge/valley is not fully visible, while a double-headed arrow line is used otherwise.

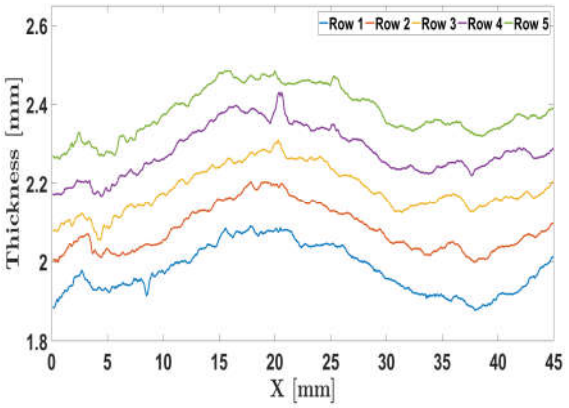

(a) Averaged Time = 10 to 12 seconds

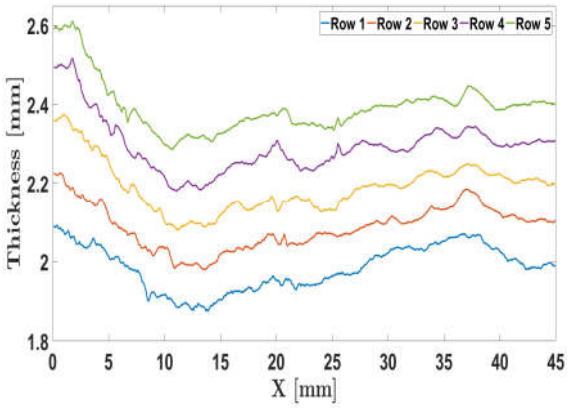

(b) Averaged Time = 12 to 14 seconds

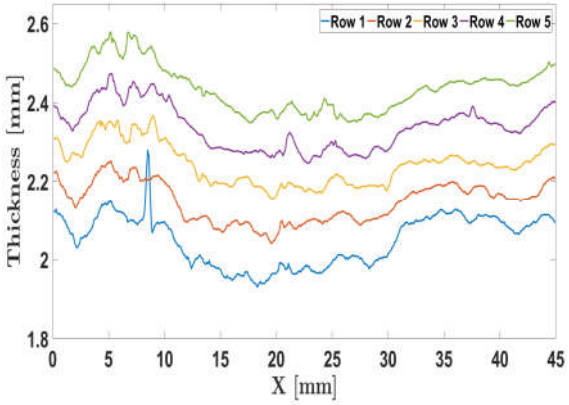

(c) Averaged Time = 16 to 18 seconds

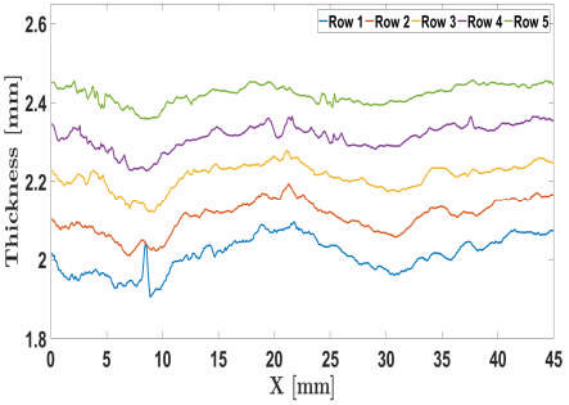

(d) Averaged Time = 18 to 20 seconds

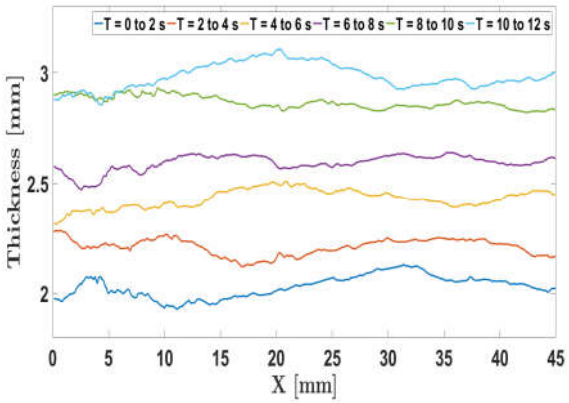

(e) Film thickness variation along Row 3 for 0 to 12 s.

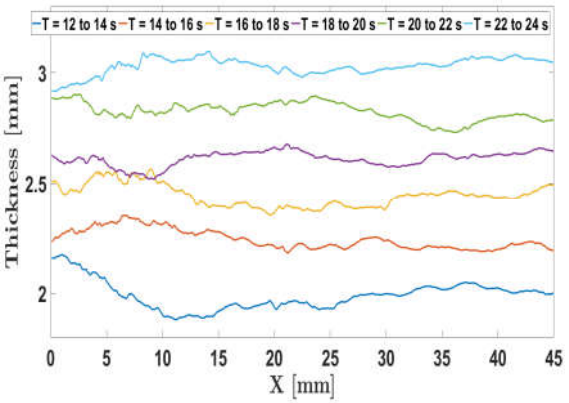

(f) Film thickness variation along Row 3 for 12 to 24 s.

Figure 3.11: Film thickness variation for *Re*=32. The thickness variation is shown at 5 horizontal lines shown in Fig. 3.10a. For description of the plots refer Fig. 3.9

3.6. PROBABILITY DENSITY DISTRIBUTION

The pattern formation such as ridges and valleys, in the transverse direction in the time averaged film thickness field - Fig. 3.8 and Fig. 3.10, is found to occur due to one of the two below-mentioned possibilities. Here the terms "fewer/higher" used is relative to the total number of the film thickness measurements considered.

1. Case A: Formation of ridges due to the fewer number of film thickness measurements above 3 mm.
2. Case B: Formation of ridges due to the higher number of film thickness measurements below 3 mm.

A plot of the probability density distribution (PDD) for the film thickness values at the region of the ridge and valley helps to understand the behaviour. One example is shown in Fig. 3.12 for the case of Re = 12. The range of the film thickness values for which the probability is calculated is plotted along the horizontal axis. The normalized probability is plotted along the vertical axis in the logarithmic scale. The film thickness measurements that are utilized for plotting the PDD corresponds to the measurement time of 16 to 18 seconds and the region of the ridge and valley are marked by the black rectangles in Fig. 3.8c. The total number of thickness data measurements in the region of ridge/valley is represented by 'N'. Before proceeding with the analysis of the PDD, one more plot is introduced - Fig. 3.13. In order to obtain this plot, a region where the PDD of the ridge/valley is measured in Fig. 3.12 is selected. The 'N' film thickness measurements in this region are arranged in ascending order, and the entries are identified as $(h_{sorted})_i$ for i = 1 to N. This is plotted along the horizontal axis. The vertical axis plots the cumulative contribution of the sorted film thickness in the range of 0 mm - 'a' mm to the average film thickness, which is indicated by $h_{cumulative}|_0^a$. It is determined by Eq. 3.5.

$$h_{cumulative}|_0^a = \frac{1}{N} \cdot \sum_{i=1}^{n} (h_{sorted})_i \quad \text{[mm]} \tag{3.5}$$

such that $(h_{sorted})_n \leq a$, and $(h_{sorted})_{n+1}$, if exists, is $> a$, were a and h are in [mm].

3.6.1. CASE A: FORMATION OF RIDGES DUE TO FEWER NUMBER OF FILM THICKNESS MEASUREMENTS ABOVE 3 MM

For Re = 12, the PDD distribution plotted at the region of the ridge and the valley, which are indicated by the black rectangles in Fig. 3.8c is shown in Fig. 3.12. The values in % hereafter in this section refers to the percentage of 'N'. Following are the observations and inferences:

(a) The number of film thickness measurements that lie in the range of 0 to 3 mm is ≈ 96 % for the ridge, while it is ≈ 98.5 % for the valley.

(b) Due to the above, it is seen in Fig. 3.13 that the cumulative contribution of the film thickness measurements in the range of 0 to 3 mm to the average film thickness is higher for the valley than for the ridge. It is 1.34 mm for the valley, while it is 1.29 mm for the ridge.

(c) The remaining film thickness measurements - ≈ 4 % for the ridge and ≈ 1.5 % for the valley, lies in the range of 3 to 15 mm.

(d) The distribution of the film thickness values in this range is such that the ridge has higher occurrence of the film thickness values than for the valley at all sub-intervals (Fig. 3.12).

(e) Due to the above, the average film thickness of the ridge is seen to increase in Fig. 3.13 in the range of 3 to 15 mm. This results in the ridge having a thickness of 1.49 mm, while for the valley it is 1.40 mm.

In this case, the ridge is formed due to fewer number (≈ 4 %) of the film thickness measurements that lies above 3 mm. A similar behaviour is found for Re =32, which are shown in Fig. 3.16 and Fig. 3.17.

3.6.2. CASE B: FORMATION OF RIDGES DUE TO HIGHER NUMBER OF FILM THICKNESS MEASUREMENTS BELOW 3 MM

For the measurement time of 18 to 20 seconds corresponding to Re = 12, the PDD and cumulative contribution to the average film thickness are shown in Fig. 3.14 and Fig. 3.15 respectively. The region of the ridge and valley are marked by the black rectangles in Fig. 3.8d. The following are the observations and inferences:

(a) The number of film thickness measurements that lie in the range of 0 to 3 mm is ≈ 98.6 % for the ridge, while it is ≈ 98 % for the valley.

(b) Due to the higher number of the thickness values for the ridge in the range of 0 to 3 mm, their contribution to the average film thickness, as seen in Fig. 3.15, is also higher - 1.41 mm for the ridge, while it is 1.31 mm for the valley.

(c) The remaining thickness measurements - ≈ 1.4 % for the ridge and ≈2 % for the valley, lie in the range of 3 to 15 mm.

(d) For the range of 3 to 15 mm, it is inferred from Fig. 3.14 that the valley has the higher probability than the ridge for all sub-intervals.

(e) Due to the above, the ridge's thickness stays relatively constant for the thickness measurements above 3 mm in Fig. 3.15.

In this case, the ridge is formed due to relatively higher number (≈ 98.6 %) of film thickness measurements below 3 mm. A similar behaviour for Re =32 is shown in Fig. 3.18 and Fig. 3.19. Note that trends observed in points (a) - (e) are in contrast for case A and case B.

Another difference between the cases is the maximum film thickness recorded for the ridge and the valley. In case A, the maximum film thickness is observed for the ridge (Fig. 3.13 and Fig. 3.17), while in case B, it is observed for the valley (Fig. 3.15 and Fig. 3.19).

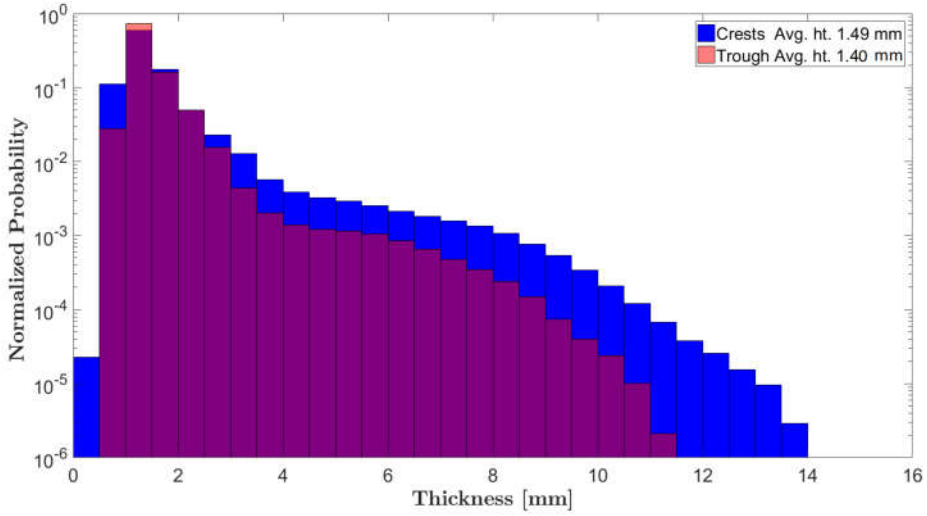

Figure 3.12: Normalized probability density distribution for $Re = 12$ plotted at the region of the ridge and the valley, which are indicated by the black rectangles in Fig. 3.8c. The measurement time is 16 to 18 s. The normalization is performed from the total number of thickness measurements, 'N', of 13.14 million for each case of ridge and valley. The thickness interval for probability measurements is 0.5 mm along the horizontal axis. The thickness measurements in the range of 0 to 3 mm is ≈ 96 % of total measurements for the ridge, while it is ≈ 98.5 % for the valley. The remaining measurements lie in the range of 3 to 15 mm. In this range, for each 0.5 mm interval, ridge has a higher probability than valley.

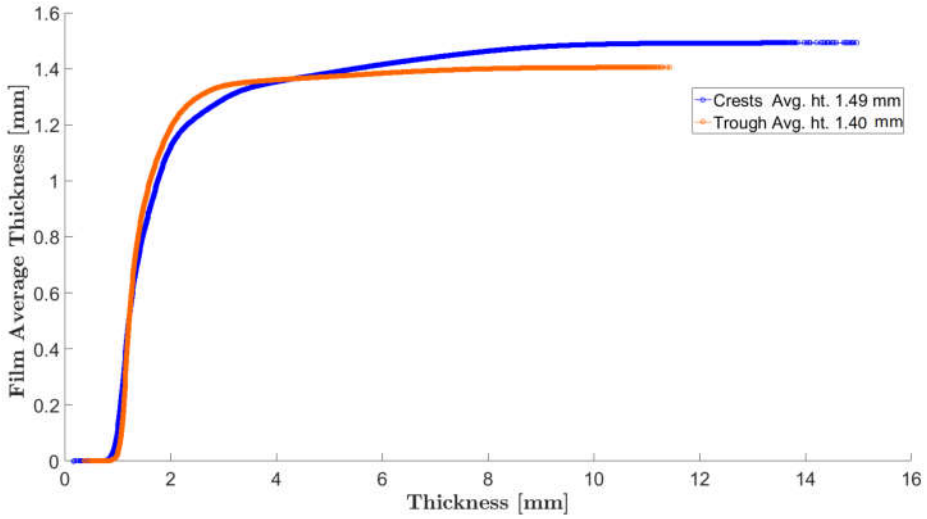

Figure 3.13: Cumulative contribution to the average film thickness (determined by Eq. 3.5) for the same data as in Fig. 3.12. The measurement time is 16 to 18 s. The cumulative contribution to the average film thickness for the ridge is less than the valley for 0 to 3 mm. This is due to higher probability of the film thickness in the range of 0 to 3 mm for the valley than for the ridge (refer Fig. 3.12). However, for the range of 3 to 15 mm, ridge has higher probability than valley. Due to this, the cumulative contribution to the average film thickness for the ridge increases in this range. The formation of ridge is due to fewer number (≈ 4 %) of the film thickness measurements that lie above 3 mm. The maximum film thickness recorded for the ridge is ≈ 15 mm, while it is less for the valley which is ≈ 11.5 mm.

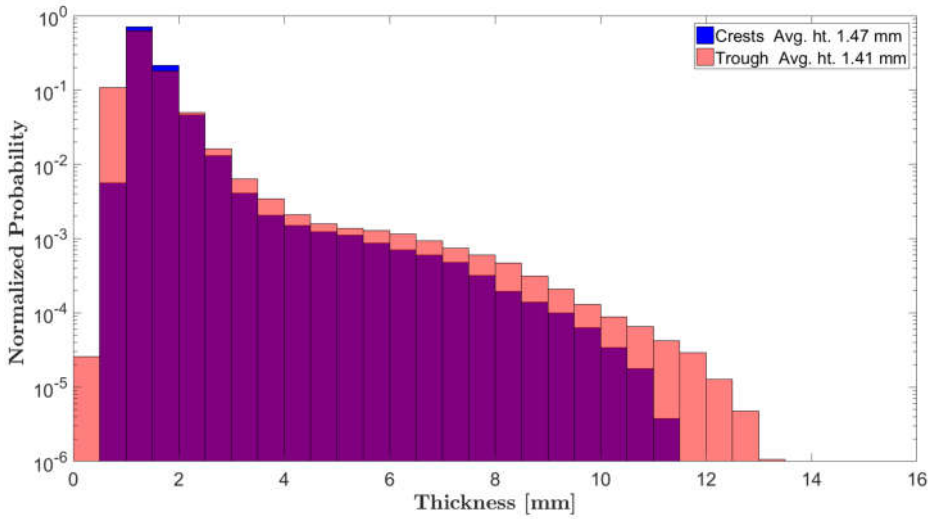

Figure 3.14: Normalized probability density distribution for Re = 12 plotted at the region of the ridge and the valley, which are indicated by the black rectangles in Fig. 3.8d. The measurement time is 18 to 20 s. The normalization is performed from the total number of thickness measurements, 'N', of 13.14 million for each case of ridge and valley. The thickness interval for probability measurements is 0.5 mm along the x axis. The thickness measurements in the range of 0 to 3 mm is ≈ 98.6 % of total measurements for the ridge, while it is ≈ 98 % for the valley. The remaining film thickness measurements lie in the range of 3 to 15 mm. In this range, for each 0.5 mm interval, the valley has a higher probability of thickness occurrence than the ridge.

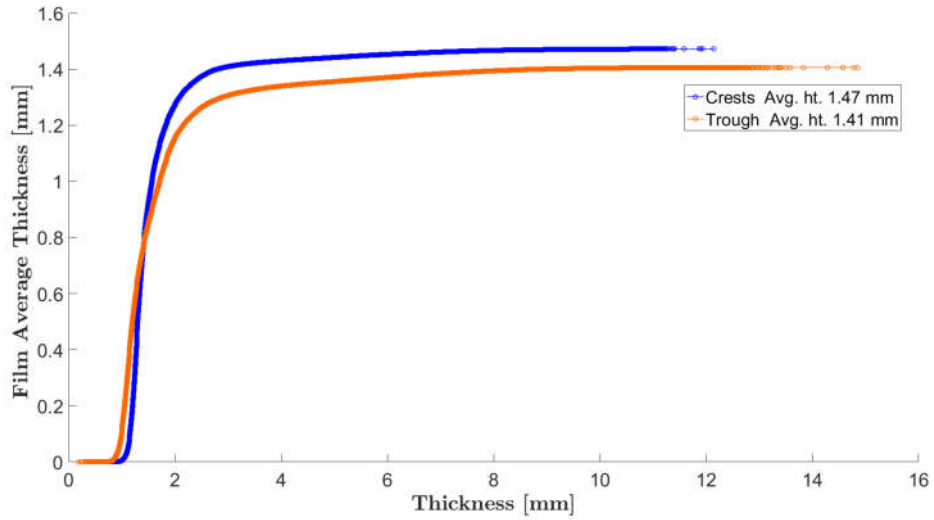

Figure 3.15: Cumulative contribution to the average film thickness (determined by Eq. 3.5) for the same data as in Fig. 3.14. The measurement time is 18 to 20 s. The cumulative contribution to the average film thickness for the ridge, unlike in Fig. 3.13, reaches a higher value than valley at 3 mm. This is due to higher probability of the film thickness measurements in the range of 0 to 3 mm for the ridge than for the valley (refer Fig. 3.14). The formation of the ridge is due to relatively higher number (≈ 98.6 %) of the film thickness measurements in the range of 0 to 3 mm. The maximum film thickness recorded for the valley is 15 mm. It is more than for the ridge, which is 12 mm.

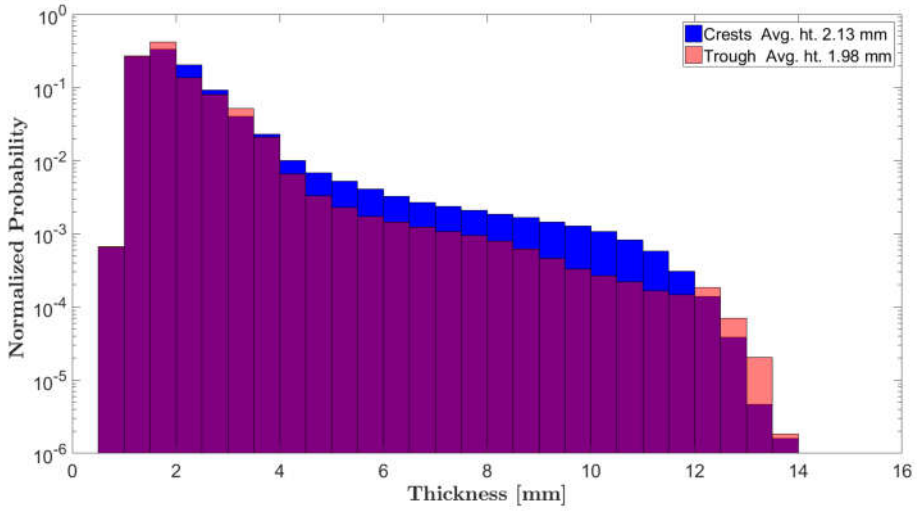

Figure 3.16: Normalized probability density distribution for Re = 32 plotted at the region of the ridge and the valley, which are indicated by the black rectangles in Fig. 3.10c. The measurement time is 16 to 18 s. The normalization is performed from the total number of thickness measurements, 'N', of 13.10 million for each case of ridge and valley. The thickness interval for probability measurements is 0.5 mm along the horizontal axis. The thickness measurements in the range of 0 to 3 mm is ≈ 89 % of total measurements for the ridge, while it is ≈ 91 % for the valley. The remaining measurements lie in the range of 3 to 15 mm. In this range, for each 0.5 mm interval, the ridge has a higher probability of the film thickness occurrence than the valley, except for few intervals at the end.

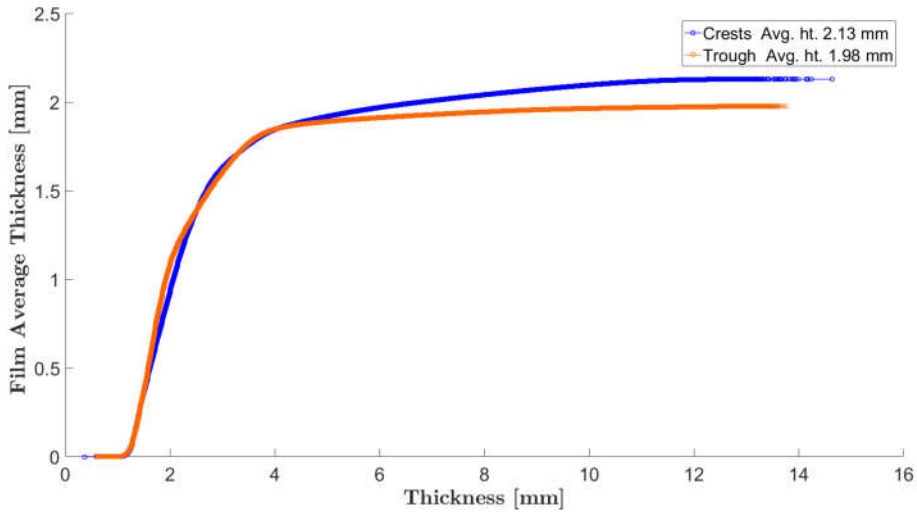

Figure 3.17: Cumulative contribution to the average film thickness (determined by Eq. 3.5) for the same data as in Fig. 3.16. The measurement time is 16 to 18 s. The cumulative contribution to the average film thickness for the ridge is less than the valley for 0 to 3 mm. This is due to higher probability of the film thickness occurrence in the range of 0 to 3 mm for the valley than for the ridge (refer Fig. 3.16). However, for the range of 3 to 15 mm, ridge has higher probability of the film thickness occurrence than the valley. Due to this, the cumulative contribution to the average film thickness for the ridge increases in this range. The formation of the ridge is due to fewer number (≈ 11 %) of the film thickness measurements in the range of 3 to 15 mm. The maximum film thickness recorded for the valley, which is ≈ 13.5 mm is less than for the ridge, ≈ 14.6 mm.

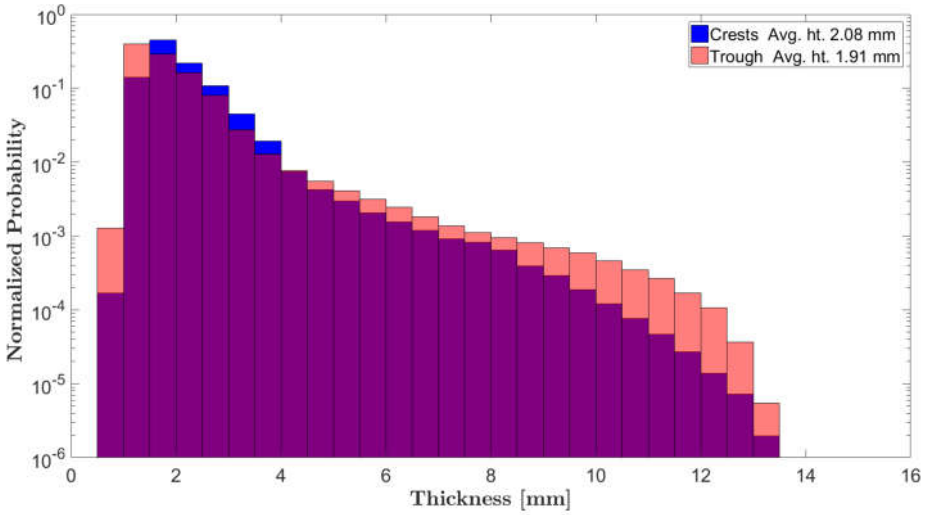

Figure 3.18: Normalized probability density distribution for $Re = 32$ plotted at the region of the ridge and the valley, which are indicated by the black rectangles in Fig. 3.10a. The measurement time is 10 to 12 s. The normalization is performed from the total number of thickness measurements, 'N', of 13.14 million for each case of ridge and valley. The thickness interval for probability measurements is 0.5 mm along the horizontal axis. The thickness measurements in the range of 0 to 4 mm is ≈ 98 % of total measurements for the ridge, while it is ≈ 97 % for the valley. The remaining measurements lie in the range of 4 to 15 mm. In this range, for each 0.5 mm interval, the valley has a higher probability than the ridge.

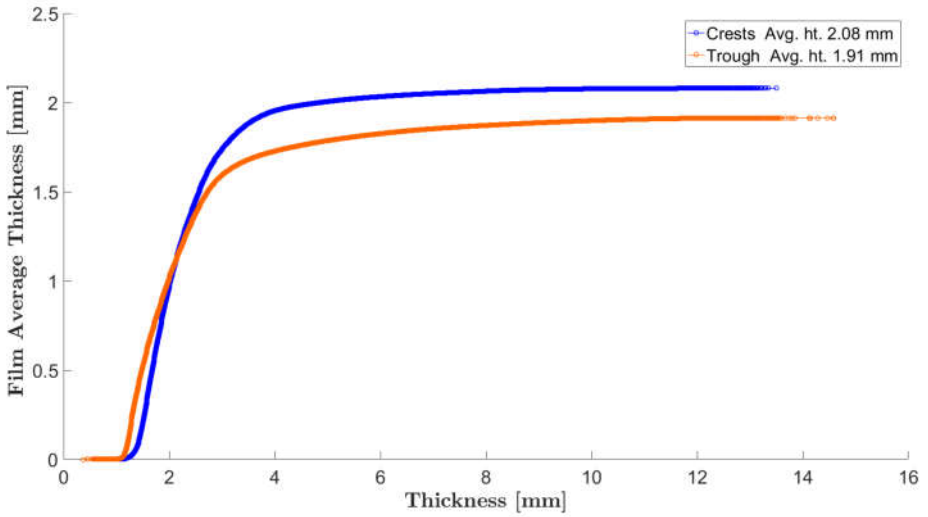

Figure 3.19: Cumulative contribution to the average film thickness (determined by Eq. 3.5) for the same data as in Fig. 3.18. The measurement time is 10 to 12 s. The cumulative contribution to the average film thickness for the ridge, unlike in Fig. 3.17, reaches a higher value than the valley at 3 mm. This is due to higher probability of the film thickness in the range of 0 to 3 mm for the ridge than for the valley (refer Fig. 3.18). The formation of the ridge is due to relatively higher number (≈ 98 %) of the film thickness measurements in the range of 0 to 4 mm. The maximum film thickness recorded for the valley, 14.5 mm, is more than for the ridge, which is 13.5 mm.

3.7. WAVE VELOCITY

The average velocity of the waves can be obtained from the instantaneous film thickness measurements using cross-correlation analysis. This is explained by considering the film thickness measurements at two points in section 3.7.1. The velocity values thus obtained should be corrected for sub-pixel interpolation, the need for which is discussed in section 3.7.2. It is followed by a discussion on the wave velocities obtained for Re = 12 and 32.

3.7.1. DETERMINATION OF VELOCITY FROM CROSS-CORRELATION ANALYSIS

For the case of Re = 32, the film thickness time series at the point a_1 in Fig. 3.1 is shown in Fig. 3.20a for a period of 6 seconds. Fig. 3.20b shows the same for a point 45 mm vertically below a_1. A third-order one-dimensional median filter is applied to remove the non-physical spikes in the thickness data. In Fig. 3.20c, their normalized

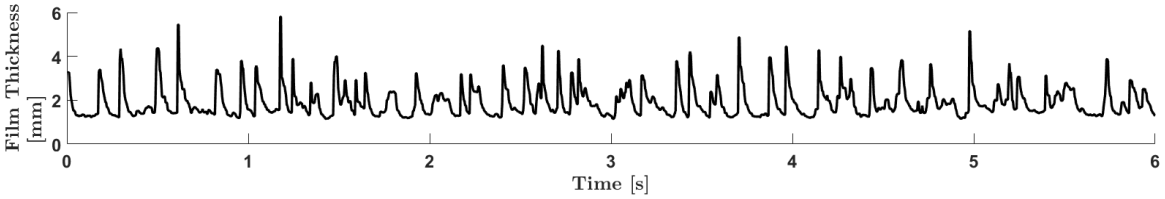

(a) Film thickness time series at the point a_1 in Fig. 3.1 for Re = 32.

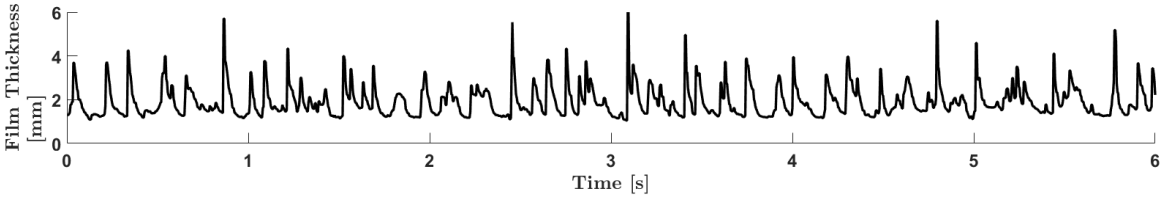

(b) Film thickness time series at the point 45 mm vertically below a_1.

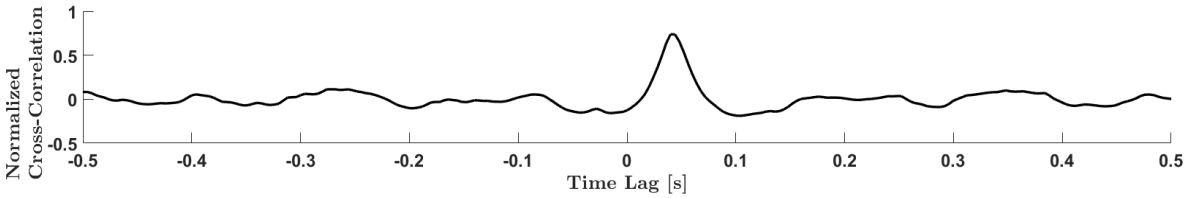

(c) Normalized cross-correlation for the thickness time series in (a) and (b). The time lag that corresponds to the maximum value of the cross-correlation coefficient is 0.044 s. The resulting average wave velocity is 1.02 m/s.

Figure 3.20: Time series of the film thickness and normalized cross-correlation between two points, for a time interval of 6 seconds.

cross-correlation is plotted along the vertical-axis, while the time lag is plotted along the horizontal-axis. The time lag that corresponds to the maximum value of the normalized cross-correlation coefficient represents the temporal offset of the film thickness measurements between the two points considered. It has a value of 0.044 s for the case shown in Fig. 3.20c. From this, the velocity is calculated to be 1.02 m/s, which represents the average wave velocity during the considered time period.

3.7.2. NEED FOR CORRECTION USING SUB-PIXEL INTERPOLATION

The method used to find the wave velocity from the film thickness time series at two points is extended to obtain the wave velocity along a series of points in a vertical line at different locations. These are shown in Fig. 3.1 by means of five columns of yellow dots identified by A to E. In each of the columns A - E, the dots are identified by their respective lower case alphabet whose subscript indicates the position of the dots. The wave velocity along a column is obtained by considering sets of two dots in each column such that the first dot is present in all the sets. For example, in column A, the film thickness time series are considered at the location

(a_1, a_2), (a_1, a_3), ..., and (a_1, a_n).

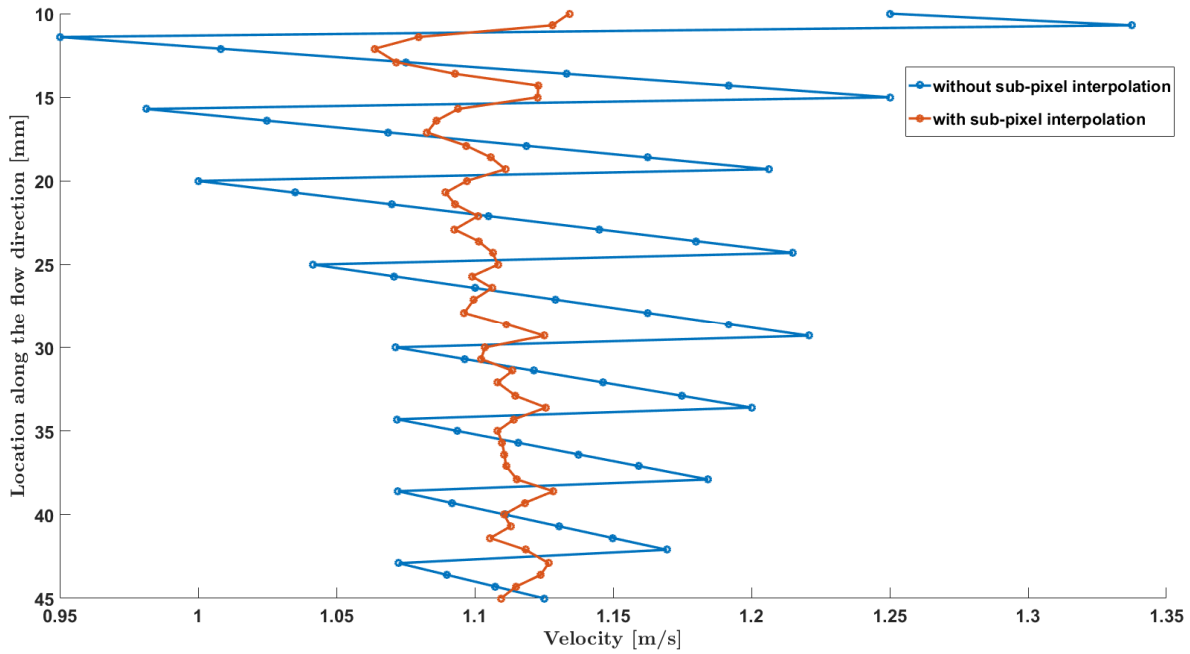

Figure 3.21: Experimentally determined wave velocity, indicated by the blue line, from the cross-correlation analysis of the film thickness time series for $Re = 32$ along column A in Fig. 3.1. Sets of two points are used to obtain the wave velocity values such that, point a_1 is present in all the sets, i.e. the sets used are (a_1, a_2), (a_1, a_3), ..., and (a_1, a_n). The velocity values indicated by the blue line represents a saw-tooth profile. It arises due to not correcting for sub-pixel interpolation, which is explained in section 3.7.2. The orange line indicates the wave velocity values obtained after correcting for sub-pixel interpolation, in which the variation is considerably reduced.

The wave velocities obtained along the column A for the case of $Re = 32$ is represented by the blue line in Fig. 3.21. It resembles a saw tooth pattern. In order to understand the reason for the formation of such a pattern, consider the following: Let the cross-correlation analysis be performed for three sets of the film thickness time series at the locations (with reference to Fig. 3.1) - (a_1, a_{49}), (a_1, a_{50}), and (a_1, a_{51}). For these sets, the values of the cross-correlation can be obtained only at the discrete time instances determined by the film thickness measurement frequency, which are multiples of 4 ms. The resulting cross-correlation values are indicated by the black dots in Fig. 3.22.

The temporal offset between the film thickness time series (t_{cc}), which corresponds to the maximum value of the cross-correlation value, is B (0.048 s) in all the three sub-figures. The wave velocity is determined by dividing the distance between the set of points considered and their temporal offset. Since the determined temporal offset remains the same while the distance between the points considered increases, the resulting wave velocity increases, instead of being nearly the same value. This error arises because the absolute maximum of the cross-correlation coefficient occurs at time instances that are less than 4 ms apart. To overcome this, a second-order polynomial is fitted to the discrete values of the cross-correlation coefficient and is represented by the dashed line in Fig. 3.22. The resulting temporal offset (t_{lag}) indicated by the red dash in Fig. 3.22, increases for the three sets considered. This indicates that the temporal offset obtained from the discrete cross-correlation values (t_{cc}) has to be corrected ($t_{correction}$) such that the t_{lag} is represented by Eq. 3.6. The value of $t_{correction}$ is obtained by taking the derivative of the fitted second-order polynomial to be zero and is represented in Eq. 3.7, where C_{left} and C_{right} represents the value that is to the immediate left and right of the maximum value of the cross-correlation coefficient C_{max}. The values of t_{cc} for the case of the blue line in Fig. 3.21 is shown in Fig. 3.23 in the same color. The values of t_{cc} are constant for sets of approximately seven locations along the flow direction. This results in the saw-tooth pattern observed in Fig. 3.21. The wave velocity calculated from the corrected temporal offset t_{lag}, and t_{lag} are shown by the orange line in Fig. 3.21 and Fig. 3.23 respectively. In this case, the saw tooth profile is considerably reduced, though not eliminated. In order to minimize them further, the temporal frequency of the measurements should be increased from the

present value of 250 Hz.

The presence of constant t_{cc} values in Fig. 3.23 in sets of approximately seven locations indicate that the temporal frequency of the film thickness measurements should be increased by a factor of seven from the present value, i.e. to 1750 Hz, if the correction for sub-pixel interpolation is to be avoided. This would result in the reduction of the camera's exposure time by one-seventh of its present value. So to record the same range of fluorescence intensities as currently recorded, the concentration of the dye should be increased such that the resulting fluorescence intensities are seven times higher. Such increase is not possible with the present experimental conditions, due to the non-linear behaviour of the resulting fluorescence intensity with increase in the dye concentration, as discussed in section 2.3.

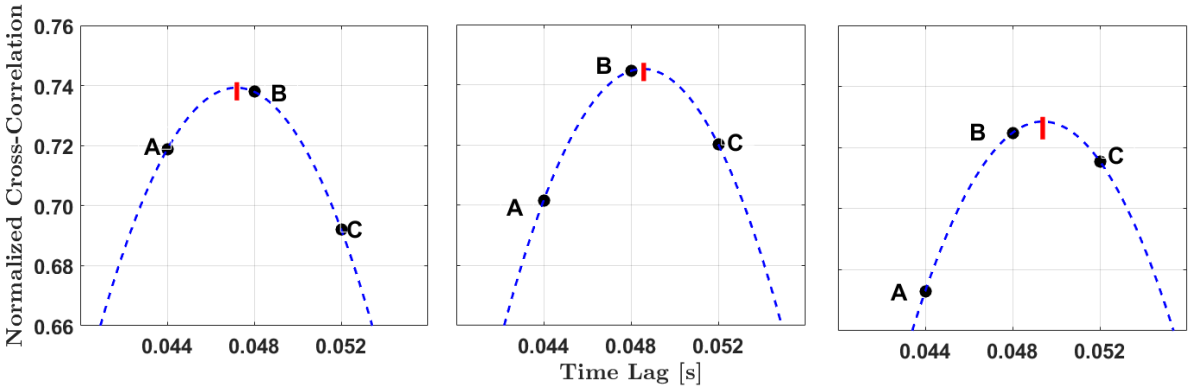

(a) Location: (a_1, a_{49}). Δd = 52.2 mm. v = 1.09 m/s. t_{lag} = 0.0472 s. $v_{corrected}$ = 1.11 m/s

(b) Location: (a_1, a_{50}). Δd = 53.1 mm. v = 1.11 m/s t_{lag} = 0.0486 s. $v_{corrected}$ = 1.10 m/s

(c) Location: (a_1, a_{51}). Δd = 54 mm. v = 1.13 m/s t_{lag} = 0.0494 s. $v_{corrected}$ = 1.10 m/s

Figure 3.22: Illustration of the need for sub-pixel interpolation. The black dots in the sub-figures (a), (b), and (c) shows the maximum (B) and its neighbouring (A, C) normalized cross-correlation values obtained by considering the film thickness time series for Re = 32, at the points indicated. For location of the points refer Fig. 3.1. The distance between the points are indicated by Δd. The time lag that corresponds to the maximum value of the normalized cross-correlation (t_{cc}) is B (0.048 s) in all three sub-figures. The resulting wave velocity represented by v, instead of being nearly the same, increases in (a), (b), and (c), since t_{cc} remains the same. To overcome this, a second-order polynomial is fitted through A, B, and C, and the corrected temporal offset (t_{lag}) is determined by Eq. 3.6. The wave velocity thus obtained are represented by $v_{corrected}$, which is observed to be nearly constant.

$$t_{lag} = t_{cc} + t_{correction} \quad [s] \tag{3.6}$$

$$t_{correction} = \frac{(C_{right} - C_{left})}{2 \cdot f \cdot ((2 \cdot C_{max}) - C_{left} - C_{right})} \quad [s] \tag{3.7}$$

Here, f is the frequency of the film thickness measurements [Hz].

The corrected wave velocities along the columns A - E in Fig. 3.1 is shown in Fig. 3.24 for the case of Re = 12, and in Fig. 3.26 for the case of Re = 32. The thin lines in these figures corresponds to the mean of the corresponding thick lines. The wave velocities are obtained by considering film thickness time series measurements for 24 seconds. The average of the wave velocities in the columns A-E for both Re are presented under $v_{exp.avg.}$ in Table 3.5. The film thickness time series that is used to obtain the experimental wave velocities are utilized to obtain Nusselt's velocity (given by Eq. 1.3), and their average of all columns is presented under $v_{th.avg.}$ in Table 3.5. The $v_{exp.avg.}$ values are ≈ 4.5 times higher than the theoretical velocity values.

The experimental wave velocities along each of the columns A - E are found to vary and their behaviour can be categorized as - fluctuating, increasing, or decreasing when compared with their respective mean, as seen in Fig. 3.24 and Fig. 3.26. The classification of the columns based on their behaviour is presented in Table 3.6.

For Re = 12 (Fig. 3.24), the mean wave velocities along each column, $v_{wave-mean}$, is found to gradually decrease from 0.84 m/s for A to 0.66 m/s for E. Such a decrease could indicate a monotonic decrease in the width of the circumferential slit, r in Fig. 2.2, due to the misalignment of the slit adjuster in the liquid distributor. To analyze this, consider Fig. 3.25 which plots the $v_{wave-mean}$ along the vertical axis and time

Table 3.5: Theoretical (given by Eq. 1.3) and experimental values of average wave velocity

Re	**Theoretical average wave velocity $v_{th.avg.}$ [m/s]**	**Experimental average wave velocity $v_{exp.avg.}$ [m/s]**	**Deviation Factor $\frac{v_{exp.avg.}}{v_{th.avg.}}$**
12	0.14	0.75	5.4
32	0.29	1.12	3.9

Table 3.6: Classification of wave velocity variation trend along the flow direction in Fig. 3.24 and Fig. 3.26

Re	**Variation of the wave velocities along the flow direction with its mean value**		
	Fluctuates	**Increases**	**Decreases**
12	A, B, C	D	E
32	E	B, C, D	A

intervals over which $v_{wave-mean}$ is averaged along the horizontal axis, with the thin vertical lines representing the mean values of their corresponding thick lines. This figure indicates that, the maximum values of $v_{wave-mean}$ for columns D and E ($\approx$ 0.8 m/s) is near the lower bound of $v_{wave-mean}$ for column A. Taking velocity to be proportional to the liquid mass flow rate, it indicates that the liquid flow rate was decreasing along the tube circumference that lies in the measurement area, during the time period of the measurement. So the misalignment in the liquid distributor is the most probable cause for the trend observed.

For $Re = 32$, $v_{wave-mean}$ is shown in Fig. 3.26 and it is approximately constant for columns A - D at 1.10 m/s, while it increases to 1.19 m/s for column E. The variation in $v_{wave-mean}$ for each of the columns A-E as a function of the time interval of averaging is plotted in Fig. 3.27. It is inferred that the variation in each column is considerable. Fig. 3.28 plots the values of $v_{wave-mean}$ obtained over a period of 24 seconds in the vertical axis and average film thickness at the location of velocity measurements obtained over the same period along the horizontal axis. The correlation coefficient for the scatter plot is 0.2, suggesting the existence of a weak relation between average wave velocity and average film thickness. This indicates that the variation in $v_{wave-mean}$, which is observed in Fig. 3.27, is probably due to the unsteady nature of the rivulets.

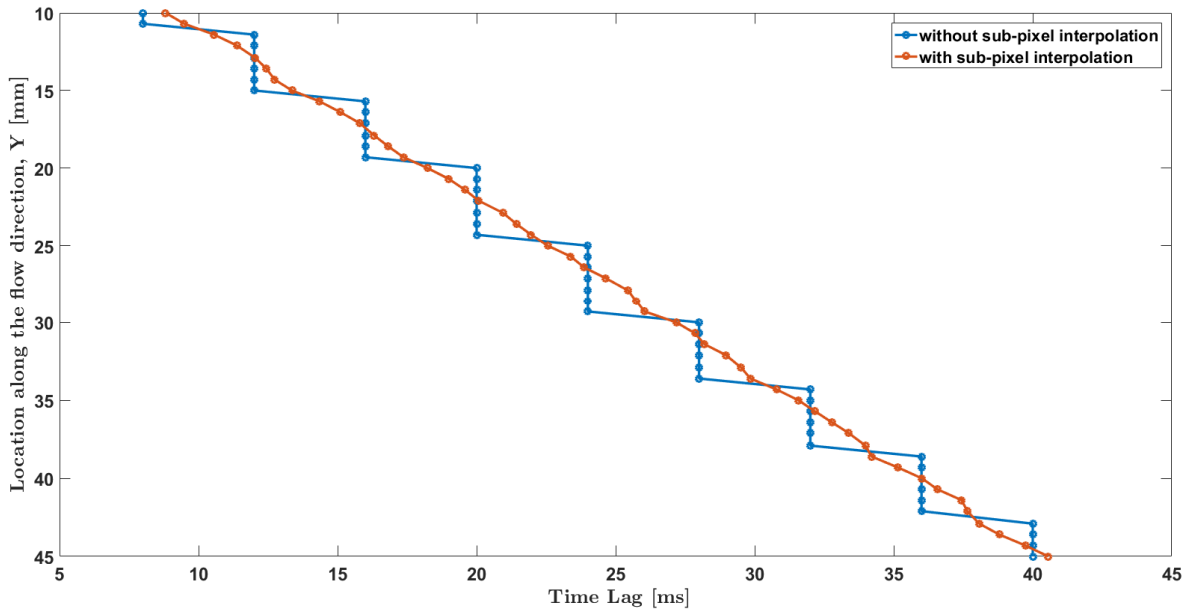

Figure 3.23: Profile of delay time determined from cross-correlation analysis with and without correcting for sub-pixel interpolation, for the case shown in Fig. 3.21.

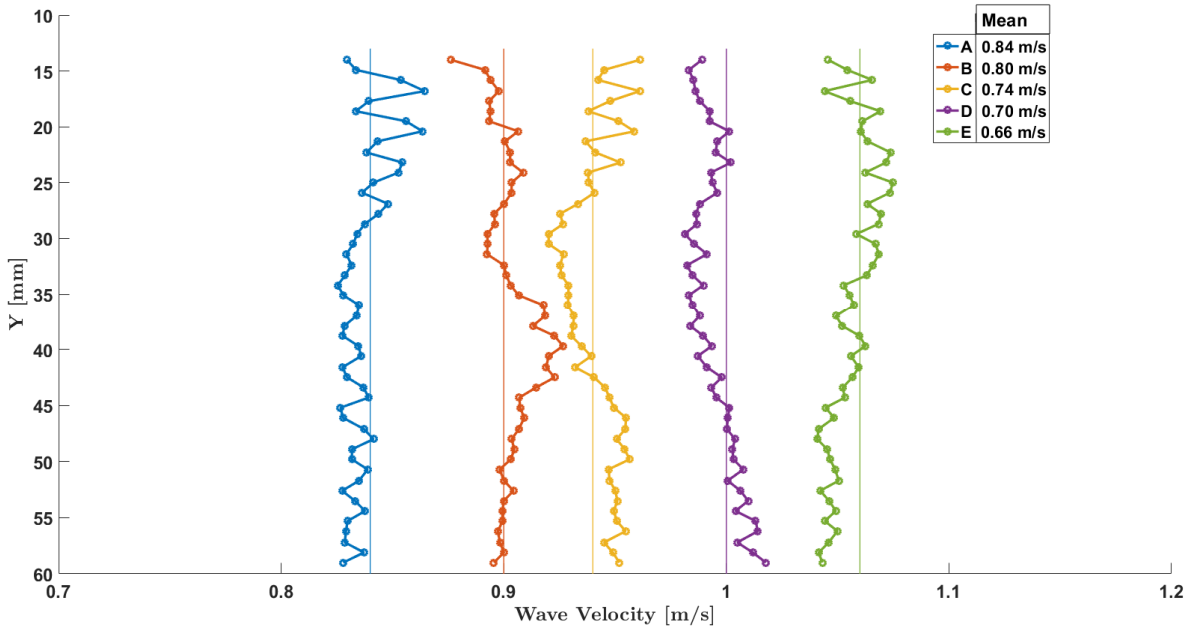

Figure 3.24: Experimentally determined wave velocities for Re = 12, along the columns A to E in Fig. 3.1. The thin vertical line represents the mean of the corresponding thick lines, which is also mentioned in the legend. The velocities for the columns B to E are successively shifted by 0.1 m/s from their actual value.

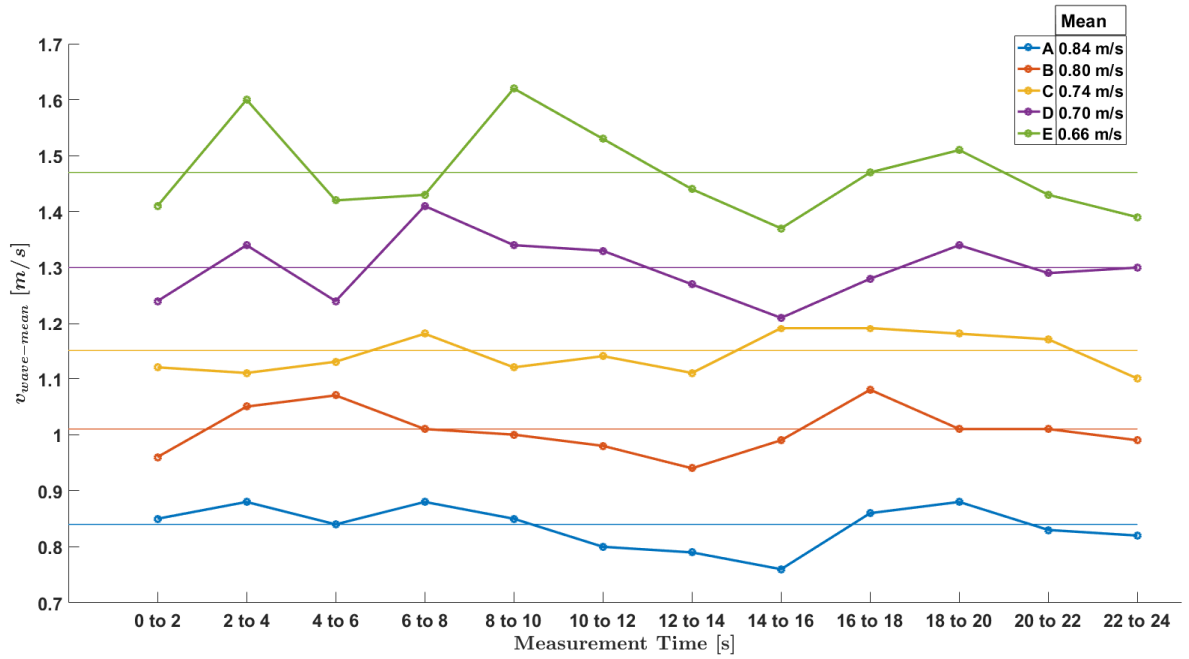

Figure 3.25: Variation in the mean of the wave velocity along the columns A-E in Fig. 3.24, with measurement time. The thin vertical line represents the mean of the corresponding thick lines, which is also mentioned in the legend. The velocities for the columns B to E are successively shifted by 0.2 m/s from their actual value.

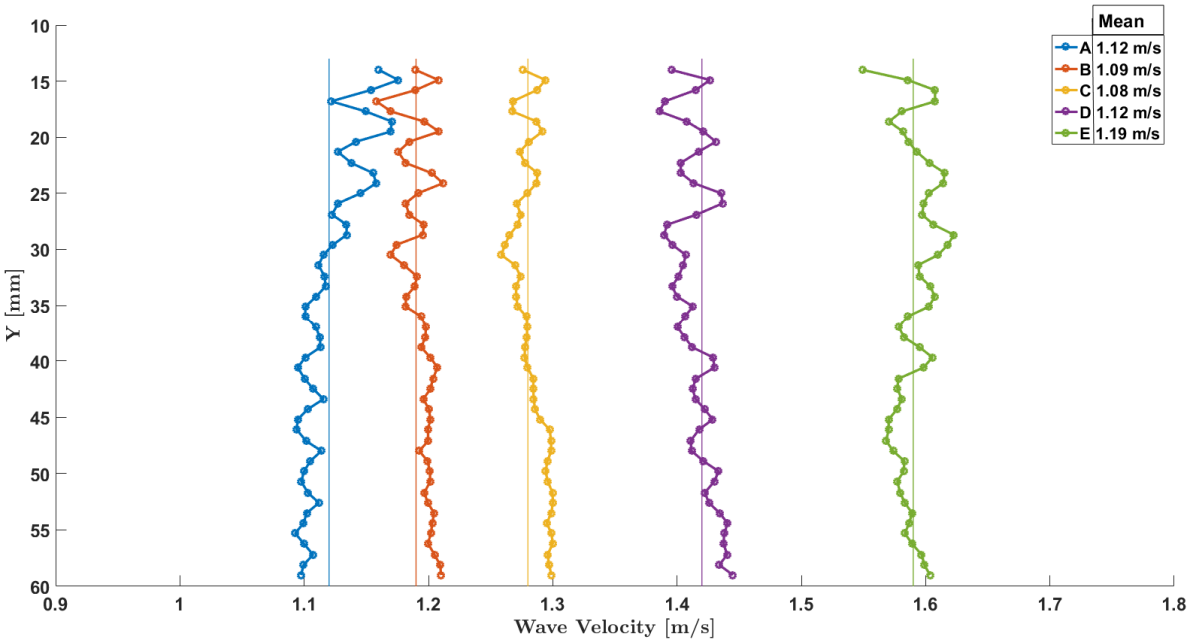

Figure 3.26: Experimentally determined wave velocities for Re = 32, along the columns A to E in Fig. 3.1. The thin vertical line represents the mean of the corresponding thick lines, which is also mentioned in the legend. The velocities for the columns B to E are successively shifted by 0.1 m/s from their actual values.

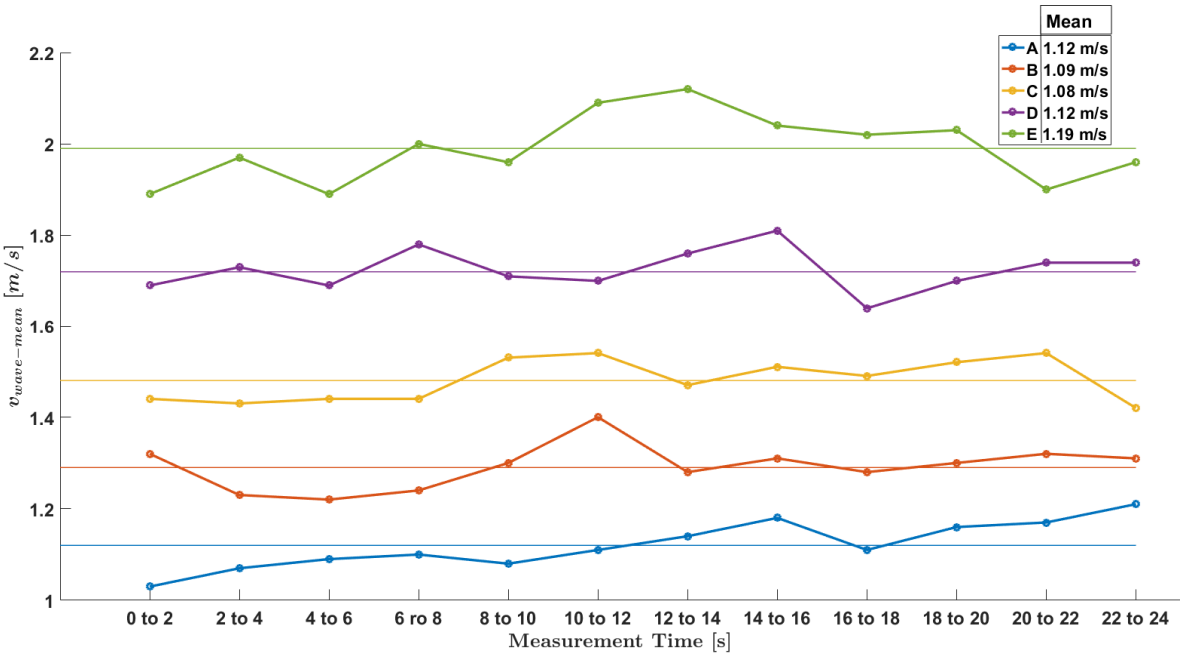

Figure 3.27: Variation in the mean of the wave velocity along the columns A-E in Fig. 3.26, with measurement time. The thin vertical line represents the mean of the corresponding thick lines, which is also mentioned in the legend. The velocities for the columns B to E are successively shifted by 0.2 m/s from their actual value.

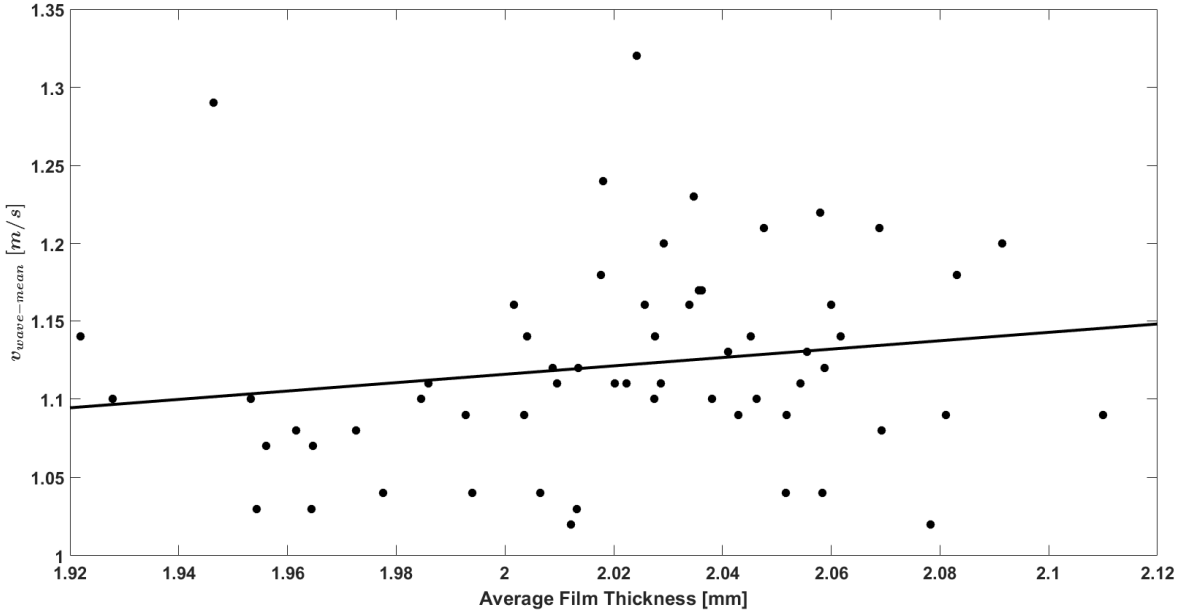

Figure 3.28: Dependency of average film thickness on average wave velocity. The correlation coefficient value is 0.2, suggesting the relationship is weak.

4

Conclusions

A vertically falling liquid film flow develops waves on its liquid-vapour interface due to various instabilities present in it. The film height dynamics of such flows were experimentally studied by re-constructing their three-dimensional interfacial profiles. Though extensive experimental studies of low viscosity liquids ($Ka \sim \mathcal{O}\left(10^2 - 10^3\right)$) were available, they are scarce for high viscosity liquids ($Ka \sim \mathcal{O}(1)$) (Mendez et al. (2017)) at low $Re \sim \mathcal{O}(10)$. Therefore the objective of the present work was to characterize film flows at low Ka and Re conditions, for which the following were performed:

- A laboratory scale setup of a vertical falling film flow on the inner circumference of a Plexiglas pipe (L = 2 m, $\varnothing_{inner}$ = 62 mm) was designed and developed.
- Quantitative visualization of the three-dimensional interfacial profile of the film flow was obtained using the Laser Induced Fluorescence technique.
- Film flow analysis were performed for Re = 11.6 (±6%) and 32.4 (±8%) using 84 ±1 wt. % glycerine–water solution with Ka = 8.05 (±7%).

Performing analysis based on the film thickness data obtained from the measurements, the following conclusions were arrived at for both the cases of Re considered:

- The steepness of the surface slope was higher at the wave-front when compared with the regions of the wave-back. This trend was observed for the waves formed by high Ka fluids at $Re \sim \mathcal{O}(10)$ by Kharlamov et al. (2015) and for $Re \sim \mathcal{O}\left(10^2 - 10^4\right)$ by Karapantsios and Karabelas (1990). The similarity in the observation indicates the importance of the gravity force at both low and high Re and Ka film flows.
- The three-dimensional shape of the waves formed had their film thickness at the back of the wave crest to be higher than at the front. This characteristic resembles the streak-like waves observed for high Ka ($\sim \mathcal{O}\left(10^3\right)$) liquids at Re ($\sim \mathcal{O}\left(10^1 - 10^2\right)$) by Kharlamov et al. (2015).
- The three-dimensional interface re-construction allowed to observe transverse merging of the waves when their lateral surface were in contact.
- The mean experimental film thickness for Re = 12 was determined to be 1.44 mm, while for Re = 32 it was 2.02 mm. These values were ≈ 15 % lower than the Nusselt's laminar film thickness. This deviation was probably due to the presence of the waves at the liquid-gas interface of the film.
- On the time averaged film thickness field, a transverse variation in the film thickness was observed. These variations were above (called as ridges) and below (called as valleys) the spatial and temporal averaged mean film thickness ($h_{s.t.avg}$). On average, the transverse variation in the time-averaged film thickness field was ± 3 % of $h_{s.t.avg}$ for Re = 12, and ± 5 % of $h_{s.t.avg}$ for Re = 32. The width of the ridges and the valleys varied from 5 mm to 20 mm for both the Re considered. These transverse variations, owing to their cyclic nature, were referred to as rivulets, which were observed to be unsteady in their behaviour. The rivulets are not calculated in the available mathematical models and were first observed by Kharlamov et al. (2015) for high Ka ($\sim \mathcal{O}\left(10^3\right)$) liquids.
- Probability density distribution of the film thickness at the rivulets revealed two time-dependant distinctive patterns for the formation of the ridges – (i) fewer number (< ≈ 5 % of the total measurements) of higher film thickness values (more than 3 mm); and (ii) higher number (≈ 96 % of the total measurements) of lower film thickness values (upto 3 mm).
- The time and space averaged wave velocity ($v_{exp.avg}$) were determined from cross-correlation analysis of the film thickness time series. For Re = 12, it was 0.75 m/s, while for Re = 32, it was 1.12 m/s. The $v_{exp.avg.}$ was ≈ 4 times higher than the Nusselt's velocity for the corresponding film thickness.

4.1. RECOMMENDATION FOR FUTURE RESEARCH

1. In order to further investigate the uniformity of flow, water sampler could be used to measure the distribution of the liquid in the transverse direction.

2. To enable studying of waves at various position of the pipe, a split-piece model of the optical box is desired. The optical box used in the present work has to be sided along the tube to change its vertical location. When doing so, due to O-ring at the bottom, a thin irregular layer of grease is deposited on the outer surface of the tube, making it optically unsuitable for future measurements.

3. The temporal frequency of measurements could be increased to avoid the saw tooth profile during velocity measurements.

4. To study the effect of evaporation, hot air can be passed through the slit adjuster in the liquid distributor.

A

MODELING LAMINAR FILM THICKNESS - WITHOUT HEAT TRANSFER

Consider a vertical wall on which a liquid film flow happens, as shown in Fig. A.1.

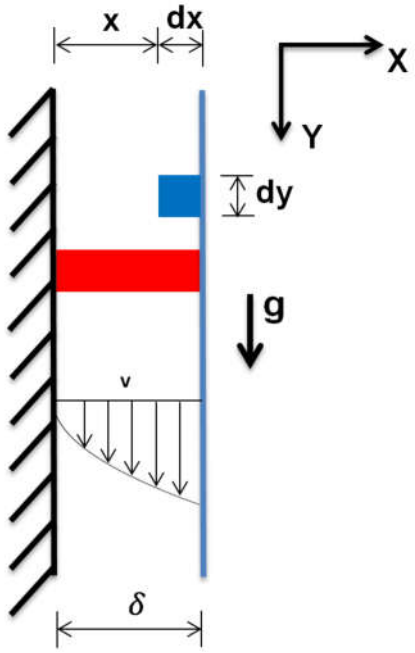

Figure A.1: Vertical falling film.The blue colored shaded region is the control volume. Film thickness is denoted by δ, while v represents the velocity in the stream-wise direction. Y axis is taken positive downwards. Z axis is normal to the figure.

Consider a small control volume which is shaded in blue color. The left side control surface is located at a distance x from the wall, while the right side control surface is located at δ, which is the film thickness, from the wall. It has a differential length of dy along the stream-wise direction, and it extends in the Z direction (normal to the figure) with length equal to the depth of the plate which is z. For a hydro-dynamically fully developed flow, since there is no acceleration, the net force acting on the control volume should be zero. A force balance on this control volume can be constructed by considering the force due to gravity ($F_{gravity}$) and the opposing force due to viscosity, i.e. shear stress ($F_{shear\text{-}stress}$), as:

$$F_{gravity} = F_{shear-stress} \tag{A.1}$$

While force due to gravity is the main contributor for the flow happening as a vertical film, it also provides an opposing force through buoyancy. The net force due to gravity is give by,

$$F_{gravity} = F_{gravity-downwards} - F_{buoyancy-upwards} = m_{liquid} \cdot g - m_{vapour} \cdot g$$

$$F_{gravity} = (\rho_{liquid} - \rho_{vapour}) \cdot V \cdot g = (\rho_{liquid} - \rho_{vapour}) \cdot (\delta - x) \cdot dy \cdot z \cdot g \tag{A.2}$$

Here m and ρ refers to the mass [kg] and density [kg/m^3] of liquid/vapour, V is the control volume [m^3], and g is the gravitational acceleration [m/s^2]. For the scenarios considered in this report, $\rho_{liquid} \sim \mathcal{O}\left(10^3 \cdot \rho_{vapour}\right)$. So ρ_{vapour} is neglected further, and ρ_{liquid} is represented by ρ.

The counter acting force due to viscous shear stress is given by,

$$F_{shearstress} = \mu \cdot \frac{\mathrm{d}v}{\mathrm{d}x} \cdot dy \cdot z \tag{A.3}$$

Here μ is the dynamic viscosity of the liquid [kg/(m $\cdot$ s], and v is the velocity of the fluid in stream-wise direction (along y in Fig. A.1).

Equating the forces,

$$\mu \cdot \frac{\mathrm{d}v}{\mathrm{d}x} \cdot dy \cdot z = \rho \cdot (\delta - x) \cdot dy \cdot z \cdot g$$

$$\frac{\mathrm{d}v}{\mathrm{d}x} = \frac{(\delta - x) \cdot g}{\nu} \tag{A.4}$$

Integrating with respect to dx yields,

$$v = \frac{(\delta x - \frac{x^2}{2}) \cdot g}{\nu} + C_1 \tag{A.5}$$

In order to determine the constant C, the no-slip boundary condition at the solid-liquid interface is applied. The vertical wall is assumed to be stationary.

$$v = 0 \quad at \quad x = 0 \tag{A.6}$$

Substituting the above condition in Eq. A.5 to eliminate the constant, the velocity profile is given by,

$$v = \frac{(\delta x - \frac{x^2}{2}) \cdot g}{\nu} \qquad [m/s] \tag{A.7}$$

This is known as Nusselt flat film velocity solution.

The mass flow rate of the liquid could be obtained by integrating the velocity over the thickness as,

$$\dot{m} = \int_0^\delta \rho \cdot v \cdot dA = \int_0^\delta \frac{\rho \cdot (\delta x - \frac{x^2}{2}) \cdot g}{\nu} \cdot dx \cdot z$$

The thermo-physical properties of the liquid are assumed to be constant across the film thickness, i.e. the properties doesn't change with temperature variation across the film. So taking the constants outside the integration, and considering unit width,

$$\dot{m} = \frac{\rho \cdot g}{\nu} \int_0^\delta (\delta x - \frac{x^2}{2}) \cdot dx$$

$$\dot{m} = \rho \cdot \frac{g}{\nu} \cdot \frac{\delta^3}{3} \qquad [kg/(m \cdot s)] \tag{A.8}$$

The laminar film thickness as a function of mass flow rate is obtained by re-arranging the terms in Eq. A.8, as shown in Eq. A.9.

$$\delta_{\text{without heat transfer}} = \left(\frac{3 \cdot \nu \cdot \dot{m}}{\rho \cdot g}\right)^{1/3} \qquad [m] \tag{A.9}$$

B

MODELING FILM THICKNESS - WITH HEAT AND MASS TRANSFER

The principle of energy conservation is used to model the film thickness with condensation or evaporation. In this case, the heat transfer happens at both the interfaces - (i) convection at liquid-vapour interface, and (ii) conduction at liquid-solid interface.

Consider a control volume which is indicated by the red colored box in Fig. A.1. Applying the principle of energy conservation to this control volume,

$$\begin{aligned} \text{Energy transferred by} \\ \text{condensation/evaporation} \\ \text{at liquid-vapour interface} \end{aligned} \quad = \quad \begin{aligned} \text{Energy transferred by} \\ \text{conduction} \\ \text{at liquid-solid interface} \end{aligned} \tag{B.1}$$

$$-d\dot{m} \cdot h_{fg} \quad = \quad -k \cdot dy \cdot z \cdot \frac{(T_{film} - T_{wall})}{\delta}$$

Here, h_{fg} is the enthalpy of vaporization of the liquid [kJ/kg], k is the thermal conductivity of the liquid [W/(m · K)], T is the temperature of film/wall [K].

The minus sign on the right of Eq. B.1 is in accordance with the Fourier's law of heat conduction. The term $d\dot{m}$ on the left indicates the change in mass of the liquid inside the control volume over a infinitesimal time period. When evaporation occurs, the mass of the liquid inside the control volume would decrease with time. This is because the mass inflow through the top control surface, apart from leaving the control volume through the bottom control surface, also leaves through the right control surface due to evaporation. So $d\dot{m}$ would be negative. So the negative sign on the left side would make the left hand side to be a positive value, which would match with the right hand side, where $T_{wall} > T_{film}$. The converse applies for condensation.

The above equation gives a relation between the variation in liquid mass flow rate and heat transfer property. If an equation relating the variation in liquid mass flow rate and film thickness could be obtained, these two equations can be combined to obtain a relation between film thickness and heat transfer property. The desired equation is obtained by differentiating Eq. A.8 as,

$$d\dot{m} = \frac{\rho \cdot g \cdot z \cdot \delta^2 \cdot d\delta}{\nu} \qquad [kg/s] \tag{B.2}$$

Combining equation Eq. B.1 and Eq. B.2,

$$\frac{-k \cdot dy \cdot \frac{(T_{film} - T_{wall})}{\delta}}{-h_{fg}} = \frac{\rho \cdot g \cdot \delta^2 \cdot d\delta}{\nu} \tag{B.3}$$

Re-arranging the terms in the above equation,

$$\frac{dy}{d\delta} = \left(\frac{h_{fg}}{k \cdot (T_{film} - T_{wall})}\right) \cdot \left(\frac{\rho \cdot g \cdot \delta^3}{\nu}\right)$$

Integrating the above equation with respect to $d\delta$,

$$y = \left(\frac{h_{fg}}{k \cdot (T_{film} - T_{wall})}\right) \cdot \left(\rho \cdot \frac{\cdot g}{\nu} \cdot \frac{\delta^4}{4}\right) + C2 \tag{B.4}$$

To evaluate the constant C2, the value of film thickness at the start of the wall (i.e. at y=0) is utilized as a boundary condition.

$$\delta = \delta_{y=0} \quad at \quad y = 0 \tag{B.5}$$

Applying the above to Eq. B.4, and re-arranging the terms to give the laminar film thickness for a flow with heat transfer,

$$\delta_{\text{with heat transfer}} = \left(\delta_{y=0}^4 + \frac{4 \cdot \nu \cdot k \cdot (T_{film} - T_{wall})}{h_{fg} \cdot \rho \cdot g} \cdot y\right)^{1/4} \qquad [m] \tag{B.6}$$

Qualitatively, Eq. B.6 informs that, for the case of evaporation, $T_{wall} > T_{film}$, the film thickness would decrease from the thickness at the start of the plate $\delta_{y=0}$. For condensation, $T_{wall} < T_{film}$, the film thickness increases down the plate.

C

QUANTIFICATION OF THE PROCESSES INVOLVED IN LASER INDUCED FLUORESCENCE

A brief quantitative description of the processes involved in LIF is presented in this section. For this purpose, the below three questions are posed, which are answered in the subsequent sections :

1. For a given energy of laser light incident on the fluorescent solution, how many molecules can be taken to the excited state ?
2. Of the excited molecules, a few would return to the ground state by means other than fluorescence. So what fraction of the excited molecules will undergo fluorescence ?
3. Of the radiated fluorescence, after accounting for various losses in the measurement system, how much will finally be detected by the camera ?

NUMBER OF MOLECULES IN EXCITED STATE

Let E_L be the total incident Laser energy on the fluorescent solution, which travels a length of Δl through the film. The number of Excited Molecules (EM) is given by Eq. C.1 (Laufer (1996)).

$$EM = \frac{E_L}{h_{Planck} \cdot \nu_{ge}} \cdot N_0 \cdot \beta_g \cdot \sigma_{ge} \cdot \Delta l \tag{C.1}$$

where, h_{Planck} is the Planck's constant (6.626 x 10^{-34} J·s), ν_{ge} is the different in frequency of light between the excited and ground state, N_0 is the total density of the species, β_g is the Boltzmann fraction, and σ_{ge} is the absorption cross-section.

MOLECULES UNDERGOING FLUORESCENCE

The molecules in the excited state, may come to the ground state in the following ways: (a) spontaneous emission, and (b) emission by passing through an intermediate level.

For detection, either of the above process can be utilized. However, due to interference of elastic scattering process with spontaneous emission, option (b) is preferred. Since both the emissions would occur simultaneously, a band pass filter is used to allow only the emission from the desired state to be passed to the photodiode.

From the total number of excited molecules EM given by Eq. C.1, only a part would emit through (b). Apart from this, there are additional losses in the excited molecules undergoing transition through the desired path.

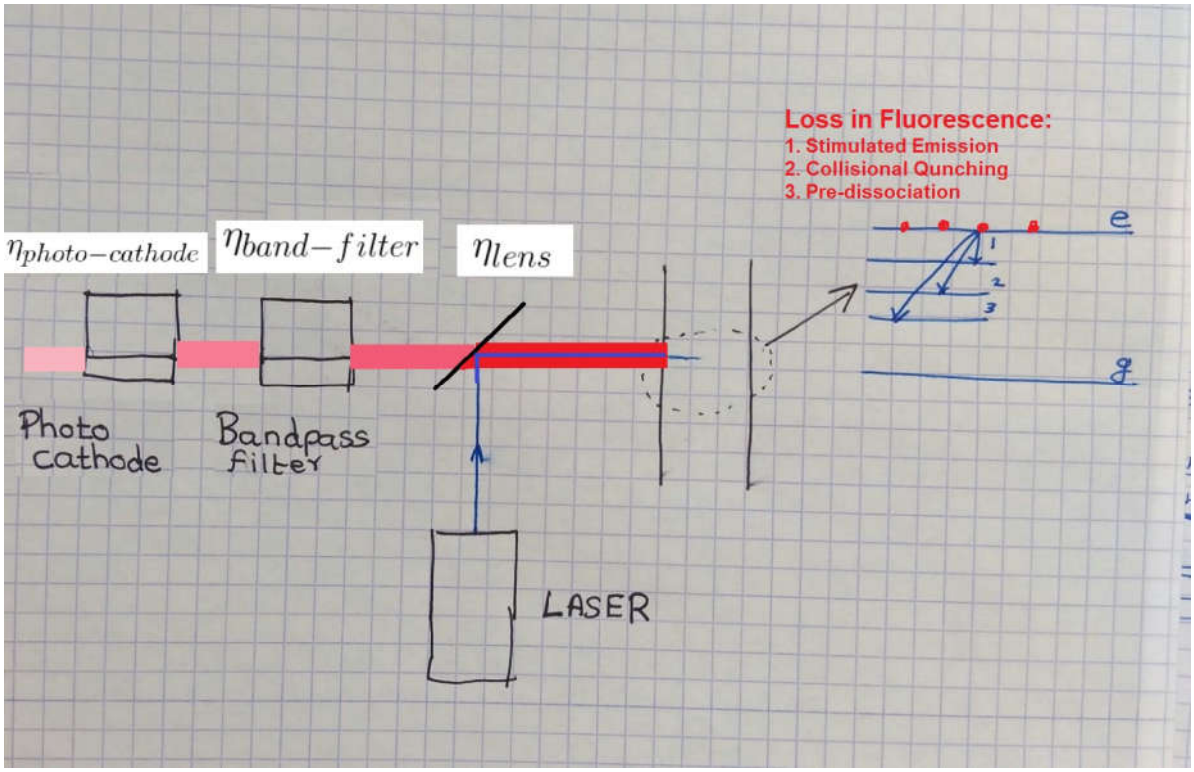

Figure C.1: Laser Induced Fluorescence (LIF) - Experimental Setup. THe fluorescence emitted (red color) has to pass through three optical arrangements before it is converted into electrical signal. There is optical loss associated with each which is represented by the reduction in the intensity of the fluorescence (red color).

1. The incident Laser ray could cause Stimulated Emission (SE), thereby causing a reduction in the number of molecules passing through the fluorescence path.
2. Collisional Quenching (CQ): The molecules in the excited state exchanges energy with other molecules through collision. Due to this, the location of the molecule in the excited state is shifted, and thus a loss of fluorescence.
3. Due to the process of Pre-Dissociation (PD), the number of molecules in the excited state could be reduced.

The above energy loss factors are accounted by the Stern-Volmer (SV) coefficient, and the number of photo electrons emitted through (b) - $n_{emitted-b}$ is given by Eq. C.2 (Laufer (1996)).

$$n_{emitted-b} = EM \cdot SV \tag{C.2}$$

FLUORESCENCE DETECTED

In order to detect the fluorescence, the measurement system consists of three main parts which are arranged in series: (i) a band pass filter to allow only the fluorescent rays to pass through, (ii) a lens arrangement to direct the fluorescence to the downstream elements, and (iii) an array of photodiode converts the incident fluorescence to photo electrons. Parts (ii) and (iii) is the . camera. Though $n_{emitted-b}$ molecules undergo fluorescence, only a part of them would be finally detected. This is due to loss associated with each of the three parts as described below.

1. Band pass filter, apart from blocking the undesired emissions, it also blocks a part of the desired emission. Its transmission efficiency is indicated by $\eta_{band-filter}$.
2. The lens arrangement has a efficiency of η_{lens}, as it cannot capture all the fluorescence emitted due to its limited solid angle.

3. The photodiode process of converting the incident fluorescence to photo electrons is limited by its quantum efficiency, $\eta_{photo-diode}$. If the array of photodiode consists of 'r' rows and 'c' columns, then each photodiode would receive $1/(r \cdot c)$ of the total incident fluorescence on the photodiode array.

Accounting for the above, the final intensity signal detected by each of the photodiode in the array is given by,

$$S = \frac{\eta_{lens} \cdot \eta_{band-filter} \cdot \eta_{photo-diode}}{r \cdot c} \cdot n_{emitted-b}$$

$$S = \frac{\eta_{lens} \cdot \eta_{band-filter} \cdot \eta_{photo-diode}}{r \cdot c} \cdot \frac{E_L}{h_{Planck} \cdot \nu_{ge}} \cdot N_0 \cdot \beta_g \cdot \sigma_{ge} \cdot \Delta l \cdot SV \tag{C.3}$$

D

Temporal Variation in the Fluorescence Intensity as recorded by the Camera

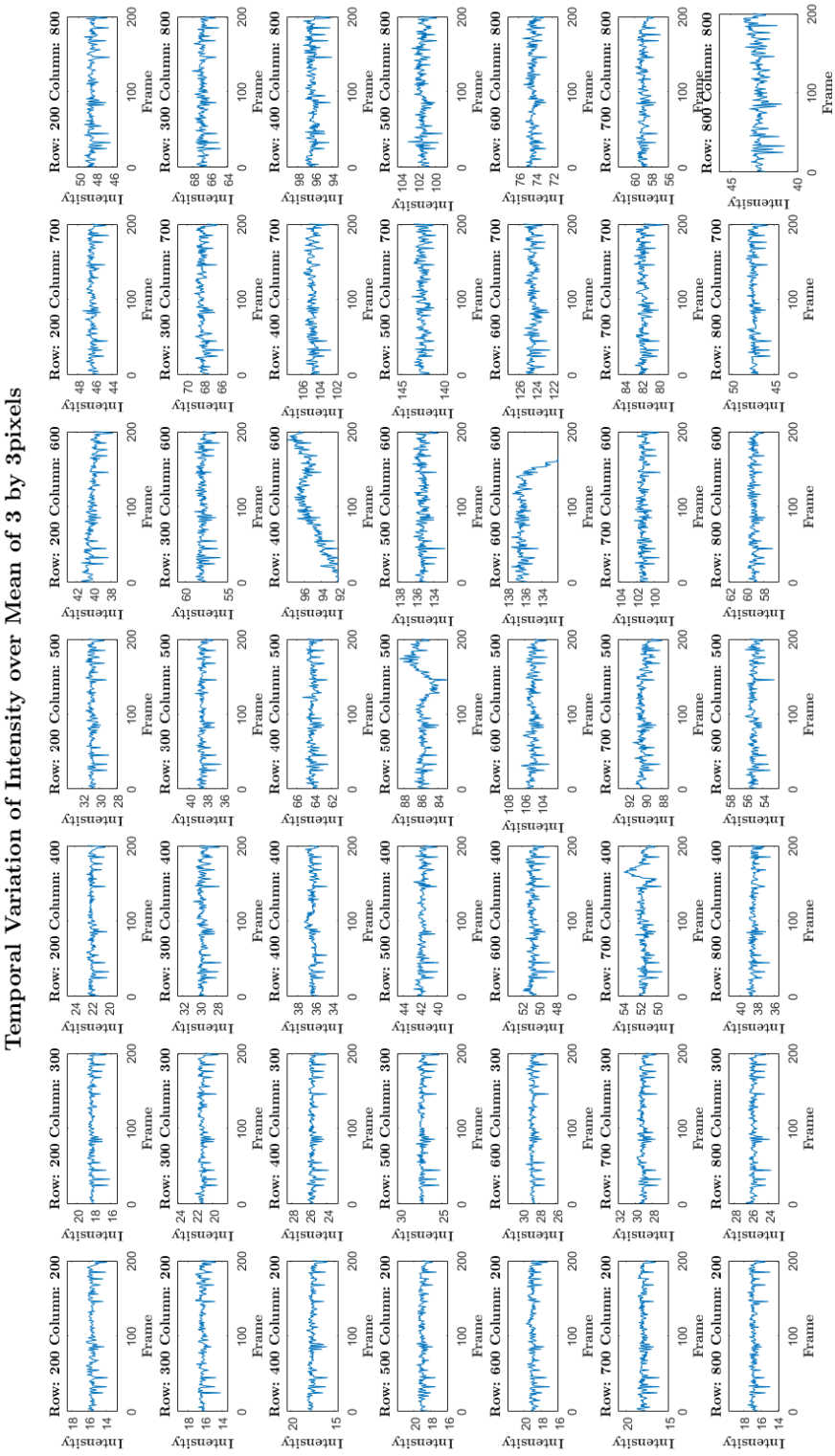

Figure D.1: Temporal variation in the intensity as recorded by the camera

REFERENCES

Sergey Alekseenko, Andrey Cherdantsev, Mikhail Cherdantsev, Sergey Isaenkov, Sergey Kharlamov, and Dmitry Markovich. Application of a high-speed laser-induced fluorescence technique for studying the three-dimensional structure of annular gas–liquid flow. *Experiments in Fluids*, 53(1):77–89, Jul 2012. ISSN 1432-1114. doi: 10.1007/s00348-011-1200-5. URL https://doi.org/10.1007/s00348-011-1200-5.

Mosen Asadi. *Beet-sugar handbook*. John Wiley & Sons, 2006.

T. Brooke Benjamin. Wave formation in laminar flow down an inclined plane. *Journal of Fluid Mechanics*, 2(6): 554–573, 1957. doi: 10.1017/S0022112057000373.

DJ Benney. Long waves on liquid films. *Studies in Applied Mathematics*, 45(1-4):150–155, 1966.

JW Boag, Pavel Evgen'evič Rubinin, and David Shoenberg. *Kapitza in Cambridge and Moscow: life and letters of a Russian physicist*. Elsevier, 2012.

L. W. Bosart and A. O. Snoddy. Specific gravity of glycerol1. *Industrial & Engineering Chemistry*, 20(12):1377–1379, 1928. doi: 10.1021/ie50228a032. URL http://dx.doi.org/10.1021/ie50228a032.

H Chang. Wave evolution on a falling film. *Annual review of fluid mechanics*, 26(1):103–136, 1994.

Nian-Sheng Cheng. Formula for the viscosity of a glycerolwater mixture. *Industrial & Engineering Chemistry Research*, 47(9):3285–3288, 2008. doi: 10.1021/ie071349z. URL http://dx.doi.org/10.1021/ie071349z.

Nicholas P Cheremisinoff. *Handbook of chemical processing equipment*. Butterworth-Heinemann, 2000.

E. A. Demekhin, E. N. Kalaidin, S. Kalliadasis, and S. Yu. Vlaskin. Three-dimensional localized coherent structures of surface turbulence. ii. solitons. *Physics of Fluids*, 19(11):114104, 2007. doi: 10.1063/1.2793149. URL https://doi.org/10.1063/1.2793149.

E. A. Demekhin, E. N. Kalaidin, and A. S. Selin. Three-dimensional localized coherent structures of surface turbulence. iii. experiment and model validation. *Physics of Fluids*, 22(9):092103, 2010. doi: 10.1063/1.3478839. URL https://doi.org/10.1063/1.3478839.

Georg Dietze and Reinhold Kneer. Flow separation in falling liquid films. *Frontiers in Heat and Mass Transfer (FHMT)*, 2(3), 2011.

GEORG F. Dietze, F. AL-SIBAI, and R. KNEER. Experimental study of flow separation in laminar falling liquid films. *Journal of Fluid Mechanics*, 637:73–104, 2009. doi: 10.1017/S0022112009008155.

GERARD Grant, BORIS Morgenroth, and K Neipoth. The balcke-duerr falling film plate evaporator-an innovative concept for evaporation in the cane industry. In *PROCEEDINGS-AUSTRALIAN SOCIETY OF SUGAR CANE TECHNOLOGISTS*, pages 355–360. PK Editorial Services; 1999, 2000.

U. Gross, Th. Storch, Ch. Philipp, and A. Doeg. Wave frequency of falling liquid films and the effect on reflux condensation in vertical tubes. *International Journal of Multiphase Flow*, 35(4):398 – 409, 2009. ISSN 0301-9322. doi: https://doi.org/10.1016/j.ijmultiphaseflow.2009.01.001. URL http://www.sciencedirect.com/science/article/pii/S0301932209000020.

Eric Jungermann and Norman OV Sonntag. *Glycerine: a key cosmetic ingredient*, volume 11. CRC Press, 1991.

Serafim Kalliadasis, Christian Ruyer-Quil, Benoit Scheid, and Manuel García Velarde. *Falling liquid films*, volume 176. Springer Science & Business Media, 2011.

PL Kapitza and SP Kapitza. Wave flow of thin fluid layers of liquid. *Zh. Eksp. Teor. Fiz*, 19:105, 1949.

T.D. Karapantsios and A.J. Karabelas. Surface characteristics of roll waves on free falling films. *International Journal of Multiphase Flow*, 16(5):835 – 852, 1990. ISSN 0301-9322. doi: https://doi.org/10.1016/0301-9322(90)90007-6. URL http://www.sciencedirect.com/science/article/pii/0301932290900076.

John Menzies Kay and Ronald Midgley Nedderman. *An Introduction to Fluid Mechanics and Heat Transfer: with applications in chemical and mechanical process engineering*. CUP Archive, 1974.

S. M. Kharlamov, V. V. Guzanov, A. V. Bobylev, S. V. Alekseenko, and D. M. Markovich. The transition from two-dimensional to three-dimensional waves in falling liquid films: Wave patterns and transverse redistribution of local flow rates. *Physics of Fluids*, 27(11):114106, 2015. doi: 10.1063/1.4935958. URL http://aip.scitation.org/doi/abs/10.1063/1.4935958.

J.P. Kockx, F.T.M. Nieuwstadt, R.V.A. Oliemans, and R. Delfos. Gas entrainment by a liquid film falling around a stationary taylor bubble in a vertical tube. *International Journal of Multiphase Flow*, 31(1):1 – 24, 2005. ISSN 0301-9322. doi: https://doi.org/10.1016/j.ijmultiphaseflow.2004.08.005. URL http://www.sciencedirect.com/science/article/pii/S0301932204001351.

Yasuo Koizumi, Ryou Enari, and Hiroyasu Ohtake. Correlations of wave characteristics for a liquid film falling down along a vertical wall. *Journal of Heat Transfer*, 131(8):082901, 2009.

G. Laufer. *Introduction to Optics and Lasers in Engineering*. July 1996.

M.A. Mendez, Benoit Scheid, and J-M Buchlin. Low kapitza falling liquid films. *Chemical Engineering Science*, 170(Supplement C):122 – 138, 2017. ISSN 0009-2509. doi: https://doi.org/10.1016/j.ces.2016.12.050. URL http://www.sciencedirect.com/science/article/pii/S0009250916307151. 13th International Conference on Gas-Liquid and Gas-Liquid-Solid Reactor Engineering.

Luan T. Nguyen and Vemuri Balakotaiah. Modeling and experimental studies of wave evolution on free falling viscous films. *Physics of Fluids*, 12(9):2236–2256, 2000. doi: 10.1063/1.1287612. URL http://dx.doi.org/10.1063/1.1287612.

Wilhelm Nusselt. Die oberflachenkondesation des wasserdamffes the surface condensation of water. *Zetrschr. Ver. Deutch. Ing.*, 60:541–546, 1916.

C. D. Park and T. Nosoko. Three-dimensional wave dynamics on a falling film and associated mass transfer. *AIChE Journal*, 49(11):2715–2727, 2003. ISSN 1547-5905. doi: 10.1002/aic.690491105. URL http://dx.doi.org/10.1002/aic.690491105.

D. Schubring, A.C. Ashwood, T.A. Shedd, and E.T. Hurlburt. Planar laser-induced fluorescence (plif) measurements of liquid film thickness in annular flow. part i: Methods and data. *International Journal of Multiphase Flow*, 36(10):815 – 824, 2010. ISSN 0301-9322. doi: https://doi.org/10.1016/j.ijmultiphaseflow.2010.05.007. URL http://www.sciencedirect.com/science/article/pii/S0301932210000984.

PL Smart and IMS Laidlaw. An evaluation of some fluorescent dyes for water tracing. *Water resources research*, 13(1):15–33, 1977.

Alan H. Varnam and Jane P. Sutherland. *Milk and Milk Products*. Springer US, 1994. doi: 10.1007/978-1-4615-1813-6. URL https://doi.org/10.1007/978-1-4615-1813-6.

James F Wilson, Ernest D Cobb, and FA Kilpatrick. Fluorometric procedures for dye tracing. Technical report, Dept. of the Interior, US Geological Survey; For sale by the Books and Open-File Reports Section, US Geological Survey,, 1986.

Donald R Woods. *Rules of thumb in engineering practice.* John Wiley & Sons, 2007.

PN Yoshimura, T Nosoko, and T Nagata. Enhancement of mass transfer into a falling laminar liquid film by two-dimensional surface waves—some experimental observations and modeling. *Chemical Engineering Science*, 51(8):1231–1240, 1996.

Nobuhiro Yotsukura, Hugo B Fischer, and William W Sayre. Measurement of mixing characteristics of the missouri river between sioux city, iowa, and plattsmouth, nebraska. Technical report, USGPO,, 1970.